



**FACULTY
OF MATHEMATICS
AND PHYSICS**
Charles University

DOCTORAL THESIS

Kristína Bartha

Phase transformations in ultra-fine grained titanium alloys

Department of Physics of Materials

Supervisor of the doctoral thesis: PhDr. RNDr. Josef Stráský, Ph.D.
Study programme: Physics
Specialization: Physics of Condensed Matter and
Materials Research

Prague 2019

I declare that I carried out this doctoral thesis independently, and only with the cited sources, literature and other professional sources.

I understand that my work relates to the rights and obligations under the Act No. 121/2000 Coll., the Copyright Act, as amended, in particular the fact that the Charles University has the right to conclude a license agreement on the use of this work as a school work pursuant to Section 60 paragraph 1 of the Copyright Act.

In..... date.....

signature

ACKNOWLEDGEMENTS

I would like to express my appreciation to my supervisor Dr. Josef Stráský for his constant support and active guidance during my studies. My sincere thanks go to Prof. Miloš Janeček for advising and his willingness of help.

Further, I would like to thank my colleagues from the Department of Physics of Materials, namely Jana Šmilauerová, Petr Hrcuba, Pavel Zháňal, Dalibor Preisler, and Jiří Kozlík who were always available for discussion and consultation; Anna Terynková and Jana Kálalová for their help during sample preparations and measurements; Cinthia Antunes Correa for her help during XRD data evaluation; Peter Minárik and Jozef Veselý for helping me with scanning and transmission electron microscope, respectively, and many others who in any way contributed to the success and good atmosphere during work time.

I would like to express my gratitude also to Prof. Jakub Čížek, Prof. Irina Semenova, Petr Doležal, Pere Barriobero-Vila, and František Lukáč.

The last but not the least, I am heartily thankful to my family and my husband, Attila for his never-ending support and encouragement.

Title: Phase transformations in ultra-fine grained titanium alloys

Author: Kristína Bartha

Department: Department of Physics of Materials

Supervisor of the doctoral thesis: PhDr. RNDr. Josef Stráský, Ph.D., Department of Physics of Materials

Abstract:

Ti15Mo alloy in a metastable β solution treated condition was processed by high pressure torsion (HPT) and equal channel angular pressing (ECAP). The microstructure after HPT is severely deformed and ultra-fine grained, while ECAP deformation results in rather coarse-grained structure with shear bands containing high density of lattice defects. Two types of thermal treatments – isothermal annealing and linear heating - were carried out for the solution treated condition and both deformed materials. Wide spectrum of experimental techniques was employed to elucidate the differences in phase transformations, especially in α phase precipitation, occurring in deformed and non-deformed material upon thermal treatment.

It was shown that the α phase precipitation is accelerated in the deformed materials due to a high density of lattice defects, which provide a dense net of preferred sites for nucleation and also fast diffusion paths necessary for accelerated growth. The enhanced precipitation of the α phase in deformed materials also affects the stability of the ω phase, promoting its dissolution. Moreover, in contrast to the non-deformed materials, where α particles form as elongated precipitates along grain boundaries and as lamellae, in deformed counterparts the α precipitates remain equiaxed.

Keywords:

metastable β titanium alloy; severe plastic deformation (SPD) methods; phase transformations; α phase precipitation

Název práce: Fázové transformace v ultra-jemnozrnných slitinách titanu

Autor: Kristína Bartha

Katedra / Ústav: Katedra fyziky materiálů

Vedoucí disertační práce: PhDr. RNDr. Josef Stráský, Ph.D., Katedra fyziky materiálů

Abstrakt:

Slitina Ti15Mo ve výchozím stavu po rozpouštěcím žíhání byla deformována metodami torze za vysokého tlaku (HPT) a protlačováním lomeným kanálem stejného průřezu (ECAP). Zatímco mikrostruktura po HPT je silně deformovaná a jemnozrnná, po ECAP zůstává převážně hrubozrnná a obsahuje smykové pásy s vysokou hustotou mřížkových poruch. Materiál ve výchozím stavu i oba deformované materiály byly podrobeny dvěma druhům tepelného zpracování – izotermálnímu žíhání a ohřevu s lineárním vzrůstem teploty. Průběh fázových transformací, zejména precipitace fáze α , probíhající ve všech materiálech během tepelného zpracování, byl studován celou řadou experimentálních metod.

Bylo prokázáno, že precipitace fáze α probíhá v deformovaných materiálech rychleji v důsledku přítomnosti vysoké hustoty mřížkových poruch, které představují hustou síť preferenčních míst pro nukleaci fáze α a dráhy rychlé difúze nutné pro urychlení růstu fáze α . Rychlejší precipitace fáze α v deformovaných materiálech rovněž ovlivňuje precipitaci fáze ω tím, že urychluje její rozpouštění. Na rozdíl od deformovaných materiálů, ve kterých fáze α precipituje ve tvaru protažených destiček podél hranic zrn nebo lamel, v deformovaných materiálech je fáze α převážně rovnoosá.

Klíčová slova:

metastabilní slitiny titanu; metody intenzivní plastické deformace; fázové transformace; precipitáty fáze α

CONTENTS

INTRODUCTION.....	1
1 THEORETICAL BACKGROUND & LITERATURE REVIEW	2
1.1 Basic characterization of titanium and its application.....	2
1.2 Structural modifications of titanium.....	3
1.2.1 Equilibrium phases.....	3
1.2.2 Non-equilibrium phases	4
1.2.3 Classification of titanium alloys	7
1.3 Phase transformations in titanium alloys.....	8
1.3.1 $\beta \rightarrow \omega$	8
1.3.2 $\omega \rightarrow \alpha$	10
1.3.3 $\beta \rightarrow \alpha$	10
1.4 Mechanism of precipitation.....	11
1.5 Methods of severe plastic deformation.....	13
1.5.1 High pressure torsion	13
1.5.2 Equal channel angular pressing.....	15
1.6 Literature review	16
2 AIMS OF THE THESIS	19
3 EXPERIMENTAL MATERIAL AND METHODS	20
3.1 Experimental material	20
3.1.1 High pressure torsion	20
3.1.2 Equal channel angular pressing.....	21
3.1.3 Ageing and heat treatments.....	21
3.2 Experimental methods.....	21
3.2.1 Scanning electron microscopy	21
3.2.2 Transmission electron microscopy.....	25
3.2.3 X-ray diffraction.....	27
3.3 Positron annihilation spectroscopy	28
3.4 Electrical resistance measurement	29
3.5 Microhardness measurement.....	30
4 RESULTS.....	32
4.1 Initial material	32
4.1.1 Ti15Mo in solution treated condition.....	32
4.1.2 Ti15Mo processed by HPT	34

4.1.3	Ti15Mo processed by ECAP.....	35
4.1.4	Phase composition of the initial materials	38
4.1.5	Microhardness of the initial materials.....	41
4.2	Effect of deformed microstructure on α phase precipitation.....	42
4.2.1	Microstructure evolution with ageing	42
4.2.2	Evolution of the phase composition with ageing	53
4.2.3	Defect structure and its evolution with ageing.....	58
4.2.4	Evolution of the microhardness with ageing.....	60
4.3	In-situ observations of phase transformations.....	61
4.3.1	In-situ high energy X-ray diffraction measurement.....	61
4.3.2	In-situ electrical resistance measurement.....	64
4.3.3	In-situ transmission electron microscopy.....	66
4.4	Ex-situ observations based on the resistivity measurement	68
4.4.1	Microstructure observed by TEM	68
4.4.2	Phase composition.....	72
5	DISCUSSION.....	74
5.1	Effect of deformation introduced by severe plastic deformation	74
5.1.1	Effect of high pressure torsion	74
5.1.2	Effect of equal channel angular pressing	75
5.2	Phase transformations during linear heating	76
5.3	Effect of isothermal ageing on phase composition and microstructure	77
5.3.1	Non-deformed material	77
5.3.2	Deformed materials	78
5.4	Enhanced α phase precipitation in deformed materials.....	78
5.5	Effect of ageing on the microhardness	80
6	CONCLUSIONS.....	83
	BIBLIOGRAPHY	86
	LIST OF ABBREVIATIONS	100

INTRODUCTION

In my master thesis defended in 2015, I focused on the microstructure and mechanical properties of metastable β titanium alloys, namely Ti15Mo and Ti-6.8Mo-4.5Fe-1.5Al (LCB). The last chapter of the master thesis was dedicated to the measurement of heat flow during heating of the non-deformed and deformed Ti15Mo alloy. The measurement revealed that ultra-fine grained structure and strain introduced into the material (by severe plastic deformation) significantly affect phase transformations in the material upon heating. Phase transformations in metastable β titanium alloys have been intensively investigated in single crystals and coarse-grained polycrystals at the Department of Physics of Materials in the last years. Therefore, the motivation of this work was to investigate the effect of ultra-fine grained and/or deformed microstructure on phase transformations in metastable β titanium alloys.

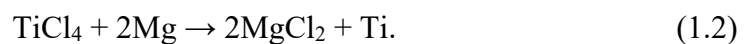
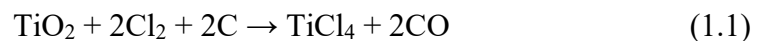
Titanium-based alloys are very attractive materials as they offer a broad range of applications due to their excellent combination of mechanical, physical and corrosion properties. β Ti alloys are also considered as perspective candidates for medical applications due to their excellent biocompatibility. Upon thermomechanical treatment, various phase transformations can occur in β Ti alloys which significantly affect the resulting mechanical properties of the material. Therefore, a thorough understanding of phase transitions is necessary to optimize the properties of the material for possible applications.

This dissertation thesis is divided into 6 chapters. The first one introduces the titanium as an element and discusses current knowledge on titanium alloys, phase transformations in Ti alloys and methods of severe plastic deformation. Comprehensive literature review is also included in the first chapter. Aims of the thesis are formulated in the second chapter, while the next one describes the methods of material manufacturing and characterization. The fourth and most extensive chapter presents achieved the experimental results, which are then discussed in the following chapter. The final chapter summarizes the most important findings of the research, concludes the work and addresses possible topics for future research.

1 THEORETICAL BACKGROUND & LITERATURE REVIEW

1.1 Basic characterization of titanium and its application

Titanium as an element was discovered by a British mineralogist and chemist William Gregor in 1791. He isolated titanium oxide from a magnetic sand, called ilmenite (FeTiO_3). Four years later, a German chemist Martin Heinrich Klaproth independently isolated titanium oxide from the ore, rutile (TiO_2). Klaproth named the new element after the Titans from the Greek mythology. It took more than 100 years to isolate the pure metal – the first successful production was achieved by Matthew Albert Hunter in 1910 by heat treating the TiCl_4 with Na. However, the commercially and technologically feasible process, known as Kroll process, was invented only in 1940 by Wilhelm Justin Kroll [1, 2]. This process is still used for the production of titanium and the underlying chemical reactions of the process can be written as follows [3]:



The product of this process is a highly porous sponge which is subsequently purified by vacuum distillation and melted to produce a compact ingot [4]. In order to improve the homogeneity of ingots multiple melting is carried out [3]. Thus, the production cost of the titanium is rather high in comparison with other light structural metals.

Titanium belongs to Group 4 of the periodic table of elements and has the atomic number of 22. It has a lustrous silver color and with a density of 4.51 g/cm^3 it is the heaviest light metal [2]. In nature, it occurs in five isotopes, ^{46}Ti through ^{50}Ti , where ^{48}Ti is the most abundant one [1].

Titanium and its alloys have remarkable properties, such as high strength-to-weight ratio, good corrosion resistance. The strength of titanium is comparable to commonly used steels; however, its density is significantly lower, allowing the fabrication of much lighter construction parts with given mechanical properties [5]. Another important property of Ti is its excellent corrosion resistance in most environments (such as sea water or human body) thanks to the formation of thin titanium oxide layer with high chemical, mechanical and thermal stability which passivates the metal in harsh environments and even at higher temperatures [1]. Due to the above mentioned properties, Ti alloys are widely used in many technological and industrial applications. The aerospace industry represents the largest market [6].

Other important fields of applications include automotive industry, chemical equipment, architecture, jewelry, sport goods, and medicine [7, 8].

1.2 Structural modifications of titanium

Titanium alloys can occur in various crystalline structures – phases – and their mixtures. The content of phases depends on different factors such as temperature, the presence of alloying elements, and also thermomechanical treatment. In this section, the equilibrium and non-equilibrium phases are described in detail as well as the classification of titanium alloys.

1.2.1 Equilibrium phases

Pure titanium is an allotropic material which means that it occurs in two structural modifications: in hexagonal close-packed (hcp) α phase at low temperatures and in body-centered cubic (bcc) β phase at high temperatures. The α phase belongs to the $P6_3/mmc$ space group; its unit cell, lattice parameters and the most densely packed planes are displayed in Figure 1.1(a). The c/a ratio is 1.586, which is smaller than the ideal closed-pack ratio for hcp cell (1.633). The α phase is stable up to the temperature of 882 °C (so-called β -transus temperature). Above this temperature, the structure transforms to the bcc β phase. This phase is stable up to the melting point of Ti (1668 °C) [5] and belongs to the space group $Im\bar{3}m$. The unit cell of the bcc structure, lattice parameters and one of the most densely packed planes are shown Figure 1.1(b).

At a given pressure, the β -transus temperature and the stability of individual phases strongly depends on the content and type of alloying elements and impurities. Three groups of impurities and alloying elements in titanium alloys can be distinguished, depending on how they affect the β -transus temperature: α stabilizing, β stabilizing and neutral elements. A schematic illustration of the effect of the types of alloying elements is shown in phase diagrams in Figure 1.2 [2]. The α stabilizing elements (e.g. Al, N, O, C) increase the temperature of the β -transus, therefore, they extend the stability range of the α phase to higher temperatures. Conversely, β stabilizers lower the temperature of the β -transus and thereby effectively widen the stability range of the bcc β phase. The β stabilizing elements can be further divided into β isomorphous and β eutectoid elements. The β isomorphous elements (e.g. Mo, V, Ta, Nb) have a high solubility in titanium. On the other hand, even a low content of the β eutectoid elements (e.g. Fe, Mn, Cr, Ni) in titanium alloys can result in the formation of intermetallic compounds [2].

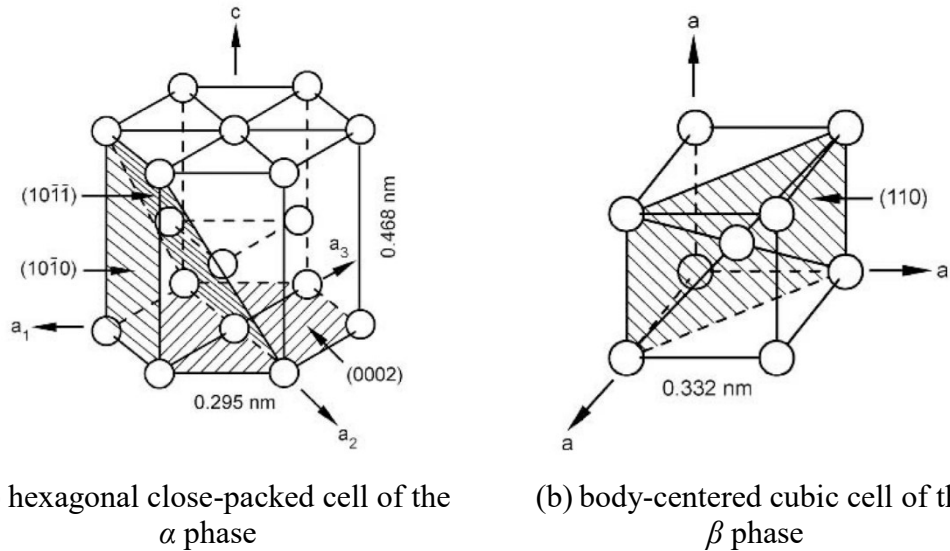


Figure 1.1 Unit cell and lattice parameters of (a) the α phase and (b) the β phase. The most densely packed planes are also indicated [1].

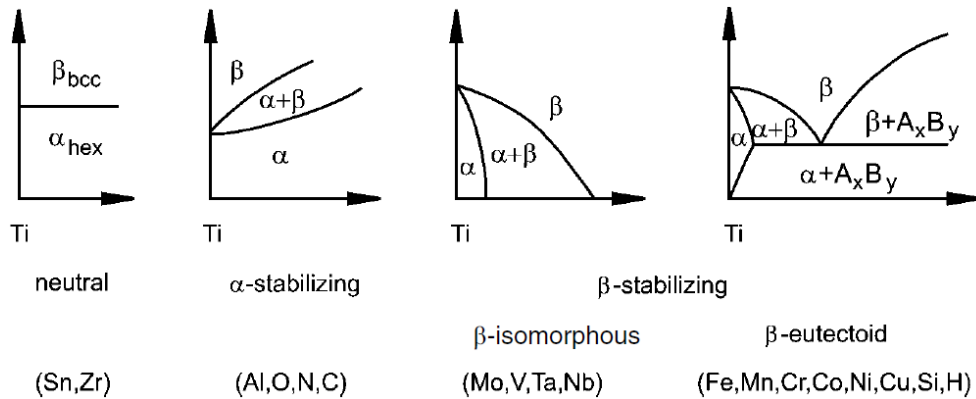


Figure 1.2 The schematic illustration of the effect of different types of alloying elements on phase diagrams of titanium alloys [2].

The neutral elements (e.g. Zr, Hf, Sn) have only a minor influence on the β -transus temperature and their stabilizing effect depends on the type of the other alloying elements. The neutral elements are often used to strengthen the α phase [1].

1.2.2 Non-equilibrium phases

Non-equilibrium or metastable phases form during very fast processes in which the thermodynamic equilibrium cannot be reached. In contrast to stable or equilibrium phases which have the lowest possible Gibbs free energy (G), metastable phases reach the local (not global) minimum of G [9]. Several metastable phases can form in titanium alloys, which are described below in detail [10]. For a better understanding, the pseudo-binary section through a β isomorphous phase diagram is displayed in

Figure 1.3 together with equilibrium and non-equilibrium phases as well as the classification of Ti alloys [1].

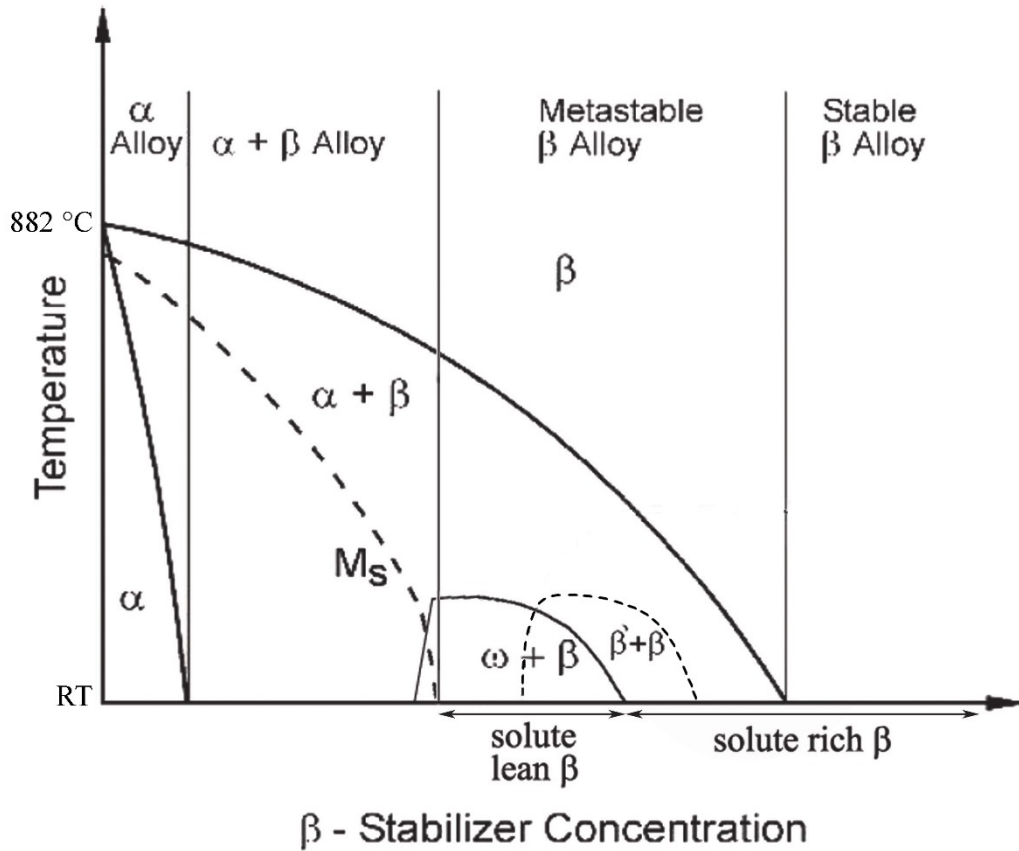


Figure 1.3 Pseudo-binary section through a β isomorphous phase diagram showing equilibrium and non-equilibrium phases as well as classification of Ti alloys [1].

Two types of martensitic phases can occur in titanium alloys: α' and α'' (the temperature of the martensite start (M_s) temperature is indicated by the dashed line in Figure 1.3). They form by a shear-type diffusionless transformation which does not result in any compositional change [10]. α' adopts a hcp structure ($P6_3/mmc$ space group) and can be observed in pure titanium and α alloys. With increasing content of the β stabilizers, the α' loses its hexagonal symmetry and can be rather described as orthorhombic – this phase is referred to as α'' .

With further increase of β stabilizer content a metastable ω phase forms in Ti alloys upon quenching (note that martensitic phases and metastable ω phase may coexist in Ti alloys – see Figure 1.3). The ω phase was discovered by Frost et al. [11] in 1954. This phase has either a hexagonal symmetry with the space group $P6/mmm$ [12] or a trigonal symmetry having the $P\bar{3}m1$ space group [13]. ω phase

particles are finely dispersed in the alloy and their size does not exceed a few hundreds of nanometers. These small particles are coherent with the parent β matrix. The shape of ω particles strongly depends on the particle/matrix misfit. At low β/ω misfit, ω particles are ellipsoidal with a long axis parallel to one of the four $\langle 111 \rangle$ directions of the β matrix. At larger misfits, ω particles become cuboidal with the flat surfaces parallel to $\{100\}$ planes of the β lattice [1]. ω particles significantly change the mechanical properties of the material – they increase the hardness but their presence results in a detriment of the ductility. ω particles can also play a role during phase transformations – they can act as preferential nucleation sites for precipitation of the α phase upon annealing [14, 15].

In general, there are several possible conditions under which the ω may form [16–18]:

1. The *athermal* ω (ω_{ath}) phase develops by shuffle mechanism during rapid quenching from temperatures above the β -transus temperature. The formation of ω_{ath} phase cannot be suppressed even by extremely high quenching rates as it was reported in [13]. The formation of this phase is diffusionless and the reversibility of the $\beta \rightarrow \omega_{ath}$ transformation was proved by several authors, e.g. [19, 20].
2. The so-called *isothermal* ω phase (ω_{iso}) forms during thermal treatment in metastable β alloys in the temperature range between 200 – 500 °C (the exact temperature depends on the alloy composition). The formation of ω_{iso} phase is displacement-controlled and diffusion-assisted, therefore the transformation is non-reversible. The ω_{iso} phase can be distinguished from the athermal one by its slightly larger size and mainly by composition differences across the β/ω interface [14].
3. Pressure may also enhance the formation of the ω phase and consequently extends the composition range in which the ω phase may be observed. The formation of the ω phase by pressure was observed in α alloys. The pressure could exceed 30 kbar for the $\alpha \rightarrow \omega$ transformation to occur [16, 21].
4. The deformation-induced ω phase (at room temperature) was first observed in Ti-8Cr [22] and in Ti-V alloy [23] single crystals.

In highly concentrated β alloys, the ω phase becomes unstable and does not form any longer. Instead, the β phase separates into β_{lean} (coherent disordered particles, often

denoted simply as β') and β_{rich} (β matrix) phase [10]. The magnitude of the lattice distortion due to β' particles is very small and their morphology varies from spheres or cuboids to plates [1, 24].

Apart from the above-mentioned phases there are some ordered ($B2$, α_2 , O'' , $B\delta_2$) or intermetallic (γ) stable phases which have been also observed in titanium alloys. These phases are not regarded as important for the purpose of this thesis. Detailed information about these phases can be found elsewhere [16, 25–28].

A useful tool to classify a multicomponent titanium alloy is to determine their equivalent aluminum and molybdenum content [29]. In titanium alloys containing α stabilizing and neutral elements, the $(\alpha+\beta)/\alpha$ transition may be significantly influenced. For example, aluminum and oxygen elevate the temperature of $(\alpha+\beta)/\alpha$ transformation when alloyed with titanium. Tin and zirconium may also play a role of a weak α stabilizing element. Rosenberg et al. have derived the so-called aluminum equivalency [30] which determines the effect of alloying elements on the $(\alpha+\beta)/\alpha$ transition with respect to Al:

$$[Al]_{eq} = 1.0 [Al] + 0.17 [Zr] + 0.33 [Sn] + 10.0 [O], \quad (1.3)$$

where $[x]$ indicates the concentration of a particular element in wt.%.

In contrast, the molybdenum equivalency defines the stability of the β phase in terms of additions to titanium which are required to suppress the martensitic start temperature below room temperature [31]:

$$[Mo]_{eq} = [Mo] + 0.67 [V] + 0.44 [W] + 0.28 [Nb] + 0.22 [Ta] + 2.9 [Fe] \\ + 1.6 [Cr] + 1.25 [Ni] + 1.7 [Mn] + 1.7 [Co] - 1.0 [Al]. \quad (1.4)$$

The negative coefficient for Al reflects the tendency of aluminum to stabilize the α phase.

1.2.3 Classification of titanium alloys

According to the phase composition at room temperature, titanium alloys are divided into 3 main groups: α alloys, $\alpha+\beta$ alloys and β alloys – this division is also schematically represented in Figure 1.3.

α alloys contain only α phase at room temperature. The major alloying elements are α stabilizers or neutral elements. So-called near α alloys contain a small addition of β stabilizing elements which results in a very small volume fraction of stable β phase in the alloy [1].

The $\alpha+\beta$ alloys, contain both α and β phase at room temperature. The range of the $\alpha+\beta$ alloys is from the $\alpha/\alpha+\beta$ phase boundary to the chemical composition at which martensite start temperature equals room temperature. $\alpha+\beta$ alloys exhibit an advantageous combination of strength, ductility, fatigue and fracture properties [1]. The microstructure and mechanical properties of these alloys can be easily controlled by appropriate heat treatment. Thanks to the above mentioned properties they are the most widely used titanium alloys in several technical and commercial applications.

Further addition of β stabilizers leads to the drop of the M_s temperature below room temperature and the suppression of martensitic phase transformation from β to α phase upon quenching. Alloys of such chemical composition are called β alloys and they are subdivided into metastable and stable β alloys. The stable ones cannot be further hardened by precipitation of the α phase and their practical use is very limited. On the other hand, in metastable β Ti alloys, the β phase is retained in metastable state in the material upon quenching from temperatures above β -transus. Nevertheless, the equilibrium phase composition of metastable β Ti falls into the $\alpha+\beta$ region and the amount of the α phase in a thermodynamic equilibrium may still be quite large [2]. Main advantages of metastable β Ti alloys are high strength and fracture toughness [1, 5]. Moreover, they undergo various phase transformations upon heating. Therefore, their microstructure and mechanical properties can be controlled by a properly designed thermomechanical treatment.

1.3 Phase transformations in titanium alloys

Titanium alloys undergo various phase transformations upon heating or ageing. The most relevant phase transformations for this study are $\beta \rightarrow \alpha$, $\beta \rightarrow \omega$, and $\omega \rightarrow \alpha$ transitions which are described in detail below.

1.3.1 $\beta \rightarrow \omega$

Particles of ω_{ath} phase form in some metastable β titanium alloys upon quenching from temperatures above the β -transus. This type of transformation can be described as diffusionless displacive shuffle. The mechanism of ω_{ath} phase formation corresponds to a shift of two neighboring $(111)_\beta$ planes along the body diagonal of the cubic cell to their intermediate position, while one $(111)_\beta$ plane between two pairs of collapsed planes is left unchanged [32]. This process is schematically shown in Figure 1.4 [33]. According to Figure 1.4, planes marked as 1/3 and 2/3 collapse to their intermediate position, while the planes 0 and 1 are unaffected (upper right corner of the image). A

full collapse of $(111)_\beta$ planes creates a basal plane $(0001)_\omega$ of the hexagonal ω phase. Nevertheless, it has been shown, that the collapse can be only partial, which results in a trigonal symmetry of the ω phase [34]. In addition, it was reported that the $\beta \rightarrow \omega_{ath}$ transformation has a mixed nature which comprises composition changes as well as displacive shuffle transition [35].

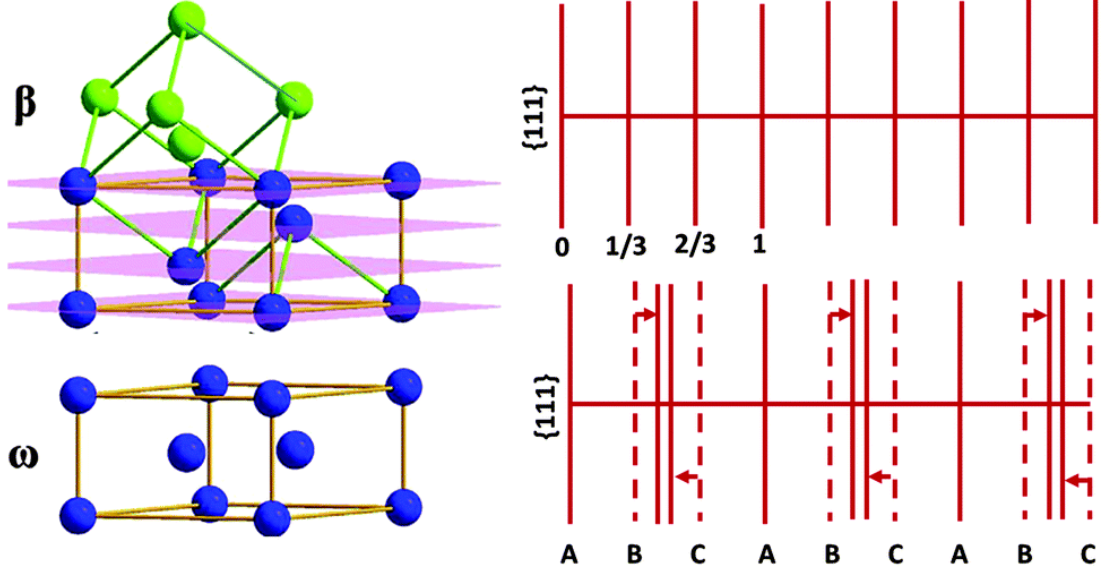


Figure 1.4 Schematic representation of the shuffle transformation from β to ω phase [33].

Due to the mechanism of formation, ω phase exhibits a certain orientation relationship with the parent β lattice [36]:

$$\begin{aligned} (0001)_\omega &|| (111)_\beta, \\ [11\bar{2}0]_\omega &|| [011]_\beta. \end{aligned} \quad (1.5)$$

Since there are four crystallographically equivalent sets of $\{111\}_\beta$ planes, there are also four possible crystallographic orientations (families) of the ω lattice. The lattice parameters of the complete ω phase (fully collapsed hexagonal one) can be easily calculated with respect to the lattice parameter of the β phase according to the equation (1.6):

$$a_\omega = \sqrt{2}a_\beta; c_\omega = \frac{\sqrt{3}}{2}a_\beta. \quad (1.6)$$

Typically at the temperature range of 300 – 400 °C, ω phase particles become stabilized by a diffusion process by rejecting alloying elements [37]. This phase is referred to as ω_{iso} phase. While the size of ω_{ath} does not exceed several nanometers, the size of ω_{iso} phase particles is typically hundreds of nanometers [38].

1.3.2 $\omega \rightarrow \alpha$

ω phase particles may serve as preferential nucleation sites for α phase precipitation during ageing. The ω assisted nucleation of the α phase was reported in systems exhibiting a high misfit between ω and β structures [39]. For a lower ω/β misfit, 3 possible ways of $\omega \rightarrow \alpha$ transformation are proposed in literature:

1. The α phase may precipitate directly inside the core of the ω particle [39, 40]. Initially, the growth of the α phase is governed by a diffusive mechanism, consuming the ω particles. After a complete dissolution of the ω phase, the growth is controlled by a migration of the α/β interface.
2. α particles may grow at a certain distance from the β/ω interface [41]. In [41] authors claimed that a possible enrichment in solute Al in the vicinity of the β/ω interface may occur in Ti-6.8Mo-4.5Fe-1.5Al alloy, which may arise from the interaction between the stress field associated with the coherent β/ω interface and the diffusion of solute elements.
3. Similarly, nucleation of α particles in Al-enriched regions in the vicinity of the β/ω interface was reported by Nag et al. in Ti-5Al-5Mo-5V-3Cr-0.5Fe (wt.%) alloy [42]. In this region the nucleation takes place via displacive-diffusional transformation in which the rate-controlling mechanism is the diffusional partitioning of the alloying elements. Similar research was performed on a Ti-6Cr-5Mo-5V-4Al (wt.%) alloy. However, the Al-rich region was not observed in the material, the nucleation of the α phase took place in oxygen enriched zone in the vicinity of the β/ω interface [43].

1.3.3 $\beta \rightarrow \alpha$

The $\beta \rightarrow \beta+\alpha$ phase transition is the most studied transformation among phase transformations occurring titanium alloys because the size, morphology and volume fraction of α precipitates determines the resulting microstructure and mechanical properties of the material.

The α phase in metastable β Ti alloys forms via a diffusion process of nucleation and growth. α precipitates are incoherent with the β matrix and obey the Burgers relationship [44]:

$$\begin{aligned} (0001)_\alpha &|| (110)_\beta, \\ [11\bar{2}0]_\alpha &|| [1\bar{1}1]_\beta. \end{aligned} \tag{1.7}$$

The nucleation of the α phase occurs heterogeneously at preferential sites such as β/β grain boundaries, previously formed α' or α'' martensites, ω phase particles, and dislocations. Three types of nucleation mechanisms are distinguished based on the ageing temperature and nucleation site [45, 46].

1. At relatively low aging temperatures (< 450 °C), very fine α phase particles precipitate in the β matrix because the precipitation is energetically favorable. Due to the size and distribution of these fine α precipitates, it is assumed that ω phase is the precursor for their nucleation.
2. At temperatures above 550 °C, ω phase particles are already dissolved [37]. The thermal activation is still sufficient for homogeneous nucleation of α phase particles within β grains. α phase then precipitates to the shape of lamellae which are bigger than α particles mentioned above. α phase may also precipitate heterogeneously along grain boundaries.
3. At high aging temperatures (> 650 °C) α phase particles do not precipitate homogeneously within the grains. The diffusivity is sufficient for precipitation; however, the driving force for homogeneous precipitation is not enough at this temperature range (i.e. just below the β -transus temperature). α phase nucleates only heterogeneously along the β/β grain boundaries and lamellae grow subsequently to the interior of grains.

The main approach to promoting uniform precipitation of the α phase is to generate a large number of preferred nucleation sites including lattice dislocations, grain boundaries, sub-grain boundaries and interfaces between β matrix and secondary phases such as ω and β' [42, 47]. The dense distribution of nucleation sites also prevents coarsening of the α phase [48].

1.4 Mechanism of precipitation

Since the main aim of this research is to study the phase transformations in metastable β titanium alloys, specifically the precipitation of the α phase, the mechanism of nucleation and growth is very important. Precipitation is a type of diffusional transformation which is induced by thermal treatment. In this section the fundamentals of precipitation of the α phase in the β matrix will be described briefly.

The precipitation transformation of the α phase in a metastable β Ti alloy can be expressed as follows [9]:

$$\beta' \rightarrow \beta + \alpha, \quad (1.8)$$

where β' denotes a β matrix supersaturated with α stabilizing elements.

Nucleation in solids is almost always heterogeneous which is a typical behavior for metastable β Ti alloys. Non-equilibrium defects such as dislocations, grain boundaries, stacking faults, etc. are examples of suitable nucleation sites. The total free energy change during nucleation can be written as [9]:

$$\Delta G_{het} = -V(\Delta G_V - \Delta G_S) + A\gamma - \Delta G_d, \quad (1.9)$$

where ΔG_S is a misfit strain energy, ΔG_V is a free energy which is released during the creation of the α nucleus, and ΔG_d is an energy which can be released during nucleation, if the nucleation results in an annihilation of a defect. The term $A\gamma$ represents the free energy increase due to interfacial energy of the α/β interface, where A is the area of the interface.

The optimal shape of the nucleus in the heterogeneous nucleation is such that the interfacial free energy is minimized. Thus, the nucleation of the α phase in β matrix at grain boundaries is feasible if the interface energy γ is sufficient (i.e. high angle grain boundaries are suitable nucleation sites). The α nucleus formed at grain boundaries is incoherent, however, the total free energy can be further reduced if the nucleus creates a coherent interface at least with one grain [49]. As a result, the α phase will have an orientation relationship with one of the grains.

Dislocations can also serve as preferential nucleation sites due to reduced misfit strain energy ΔG_S . Pipe diffusion along the dislocation core is able to assist in the growth of a nucleus beyond its critical size [50]. On the other hand, dislocations do not reduce significantly the interfacial energy.

When the material is quenched from a high temperature, excess vacancies are retained during quenching. These vacancies can also facilitate the nucleation by enhancing diffusion or by relieving misfit energies [51].

The second stage of precipitation – the growth – is controlled by the migration of the α/β interface and/or diffusion of solute atoms within β matrix. The growth rate is controlled by the slower of these simultaneously occurring processes [9].

In order to reach the thermodynamic equilibrium, the shape of the α precipitate should satisfy the criterion of a minimum interfacial energy of the nucleus. The nucleus is therefore bounded by a combination of coherent, semicoherent and incoherent interfaces. These interfaces must migrate to allow the growth of the precipitate. The semicoherent interfaces have very low mobility and are forced to migrate by a ledge

mechanism. On the other hand, incoherent interfaces are highly mobile. Therefore, in a lack of ledges, the incoherent interface will migrate faster which results in a precipitate in a form of a thin disc or plate (so-called Widmanstätten morphology [51]).

1.5 Methods of severe plastic deformation

Methods of severe plastic deformation (SPD) are effective in introducing a high density of lattice defects, such as grain boundaries or dislocations, to the material [52]. Generally, SPD are defined as we understand metal forming methods during which extremely high hydrostatic pressures are employed, introducing a very large deformation (hundreds or thousands percent) into the material. In some cases, the shape of the SPD devices is designed to prevent the material from outflow (the material remains in its original shape), thereby producing a high hydrostatic pressure. The presence of this pressure is essential to achieve large deformations and to introduce a high density of lattice defects that are necessary for significant grain refinement [53]. SPD processing usually results in the formation of ultra-fine grained (UFG) structure while maintaining the overall dimensions of the specimens [54, 55].

The SPD deformed materials generally exhibit excellent mechanical properties, such as strength, hardness, or fatigue resistance. Unfortunately, enhanced mechanical properties are very often offset by poor ductility [56]. The reduction of the grain size in polycrystalline materials results in increased strength which generally follows the Hall-Petch relation at ambient temperature [57, 58]:

$$\sigma_y = \sigma_0 + k_y d^{-\frac{1}{2}}, \quad (1.10)$$

where σ_y is the yield stress of the material, σ_0 represents the friction stress, k_y is a material constant and d is the mean size of grains.

There are several techniques of SPD, the most popular being equal channel angular pressing (ECAP) pioneered by Segal [59] and further developed by Valiev [60]. Other frequently used SPD methods include high pressure torsion (HPT) [61], accumulative roll-bonding (ARB) [62] or friction stir processing (FSP) [63]. The two most important methods for this study, HPT and ECAP will be described in detail in the following sections.

1.5.1 High pressure torsion

During HPT, a disc-shaped sample with a diameter ranging from 5 to 50 mm and a thickness of 1–10 mm is placed between two anvils which compress the sample at high

pressure (several GPa). In the next step of the process, one of the anvils is rotated (typically 1 revolution per minute) which consequently leads to the torsion of the sample. The schematic representation of the procedure is shown in Figure 1.5. The total strain ϵ_{vM} imposed by HPT can be expressed by von Mises equation using a simple torsion (neglecting the initial thickness of the sample) [64]:

$$\epsilon_{vM} = \frac{\gamma}{\sqrt{3}} = \frac{r\theta}{\sqrt{3}h} = \frac{2\pi Nr}{\sqrt{3}h}, \quad (1.11)$$

where γ is the shear strain, θ is the rotation angle, N is the number of revolutions, r represents the distance from the center of the sample, and h is the final thickness of the specimen.

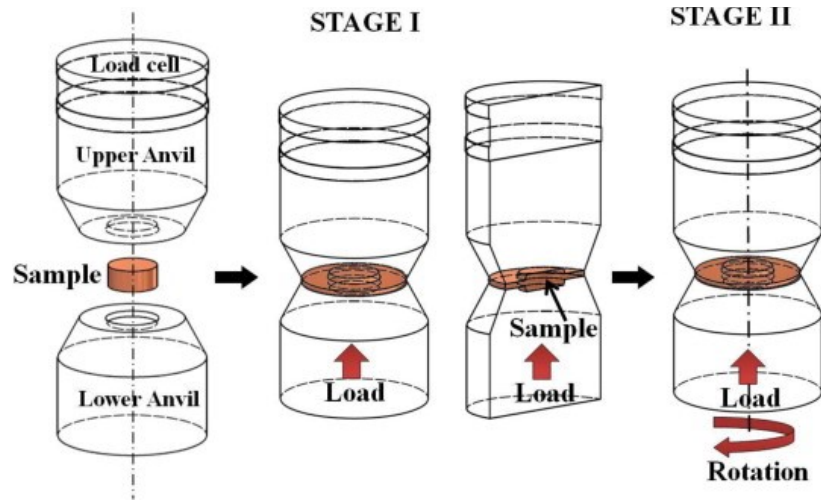


Figure 1.5 Schematic representation of the principle of high pressure torsion [65].

It was reported that the imposed strain during HPT leads to an exceptional grain refinement accompanied by an improvement of room temperature strength in various materials [66–71]. A major disadvantage of HPT processing is the non-uniform deformation across the sample; the imposed strain increases with the distance from the center of the specimen (as it is indicated by Equation 1.11). The inhomogeneous distribution of strain across the specimen may be easily mapped by microhardness measurement as first reported in high-purity Ni [71]. Another disadvantage of the HPT deformation is the small size of the specimens which limits their practical use. Nevertheless, they are often used in micromanufacturing [61]. Recently, some progress in upscaling of the HPT process was made: Sakai et al. designed an HPT machine for cylindrical samples with a thickness up to ~ 8 mm [72], Um et al. reported

the deformation of hollow cone samples with a diameter larger than 30 mm [73], or Horita et al. developed a so-called high pressure sliding to prepare metallic sheets of a rectangular shape [74].

1.5.2 Equal channel angular pressing

ECAP represents one of the most developed and commercially used SPD techniques. During ECAP, the sample is pressed through a specially designed die composed of two channels of the same cross-section, which intersect at an angle Φ . The most frequently used dies form the angle of 90° . However, a higher intersection angle, usually $\Phi = 120^\circ$, is used for poorly deformable materials, such as titanium alloy in our case, see Figure 1.6. Another characteristic angle Ψ of the die represents the "outer curvature" of the channel which can be either sharp ($\Psi = 0$) or rounded ($\Psi > 0$) - see also Figure 1.6.

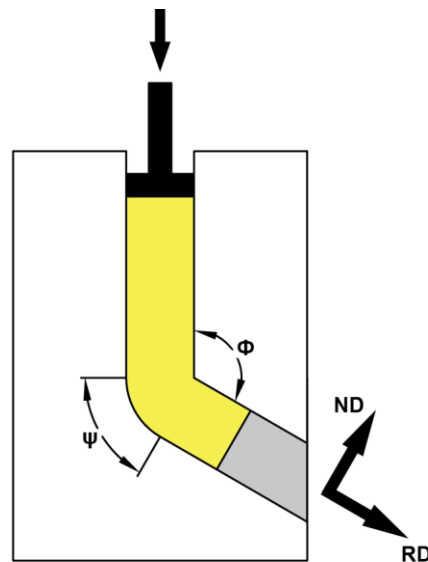


Figure 1.6 Schematic representation of equal channel angular pressing.

The sample processed using ECAP is deformed by a simple shear; the shear deformation is schematically displayed in Figure 1.7 for angles $\Psi = 0$ and $\Psi > 0$.

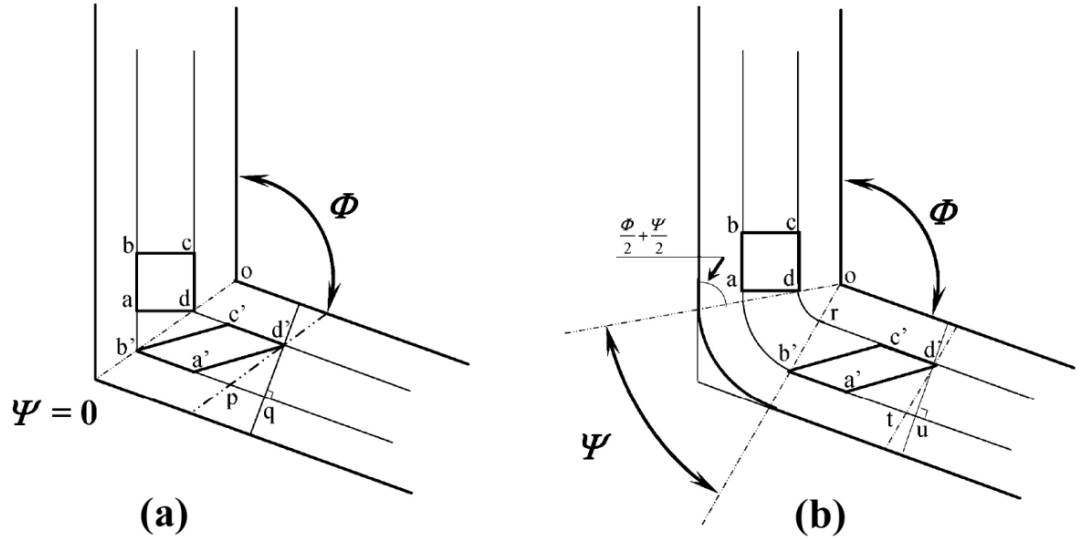


Figure 1.7 Schematic representation of shear deformation during ECAP for (a) $\Psi = 0$ and (b) $\Psi > 0$ [75].

The equivalent strain ε_{vM} imposed to the material after N ECAP passes through the die depends on its geometry and can be determined from the equation [75]:

$$\varepsilon_{vM} = N \cdot \frac{1}{\sqrt{3}} \left[2 \cotg \left(\frac{\phi}{2} + \frac{\psi}{2} \right) + \psi \operatorname{cosec} \left(\frac{\phi}{2} + \frac{\psi}{2} \right) \right] \quad (1.12)$$

This method was first successfully applied to produce UFG microstructure in several metals [76–79]. Nowadays, a wide variety of alloys have been successfully produced by ECAP. The main advantage of the ECAP technique compared to HPT method is a larger specimen size providing a wider range of potential industrial applications. On the other hand, HPT method is more efficient than ECAP in producing extremely small grains [80]. In order to upscale the ECAP process, a so-called ECAP-Conform method was developed by Raab et al. [81] which is able to produce material in the form of long rods.

1.6 Literature review

This work mainly focuses on the effect of heavily deformed microstructure and induced lattice defects on phase transformations in the metastable β Ti15Mo alloy. In this section recent research dealing with phase transitions in metastable β Ti alloys is briefly discussed and a literature review of titanium and its alloys after severe plastic deformation is provided.

UFG commercially pure (CP) Ti was first prepared by HPT at Ufa State Aviation Technical University (USATU), Ufa, Russian Federation, more than two decades ago,

in 1997 [82]. ECAP deformation of pure Ti was performed some years later by Stolyarov et al. [83]. The results showed that strength achieved by HPT is significantly superior to that achieved by ECAP. Later, several studies were dedicated to the investigation of deformation mechanisms during ECAP [84–88] – it was revealed that twinning and strain accommodation may take place during deformation.

The first SPD-processed titanium alloy, namely an $\alpha+\beta$ Ti alloy Ti6Al4V, was prepared by HPT [89] just three years after CP Ti. The investigation of SPD-processed $\alpha+\beta$ Ti alloys has mainly focused on the improved mechanical and physical properties [86, 90–94].

On the other hand, metastable β Ti alloys were subjected to SPD processing only in early 2010s [95–100]. The main advantage of UFG metastable β Ti alloys is their improved biocompatibility, higher strength with reduced Young's modulus which is essential for use in medicine [95, 100–102]. Moreover, the properties of metastable β Ti alloys can be controlled by thermomechanical treatments as they undergo various phase transformations [103, 104].

Mechanical properties of two types of metastable β Ti alloys (Ti15Mo and Ti LCB) processed by SPD methods were characterized in details in my Master thesis [105] and also in our previous works [95, 96, 106, 107]. Phase transformations in coarse-grained (CG) β Ti alloys (including Ti15Mo alloy) have already been extensively studied at the Department of Physics of Materials [19, 34, 37, 108, 109] and also by other authors [45, 110–113]. However, phase transitions in deformed and UFG metastable β Ti alloys and the effect of UFG structure on phase transformations were scarcely investigated:

- The first study of the α phase precipitation in UFG metastable β Ti alloy was performed by Xu et al. [114]. The authors subjected the Ti20Mo alloy to ECAP deformation which resulted in a formation of shear bands. These shear bands containing a high density of dislocations and low angle grain boundaries served as preferential nucleation sites for α particles. The authors observed equiaxed α precipitates in the SPD-processed samples as opposed to α lamellar forming in the coarse-grained material [115], [116].
- Xu et al. in their next study [117] showed that Ti20Mo alloy after HPT deformation also exhibits similar equiaxed and UFG $\alpha+\beta$ structure upon ageing.
- Jiang et al. [115] revealed an UFG structure containing shear bands in HPT-deformed Ti15Mo alloy which responds to ageing similarly to Ti20Mo in

previous studies. The authors investigated the kinetics of precipitation in SPD deformed alloy and reported that induced deformation and high density of lattice defects shifts the α phase precipitation to lower temperatures compared to non-deformed material. In addition, they observed high microhardness in aged samples. However, they did not relate the microhardness increase to possible ω phase formation, because laboratory X-ray diffraction was not able to detect the ω phase. The tensile tests also showed a higher strength and reduced ductility of the HPT-deformed and aged alloy compared to non-deformed alloy which the authors explained by the precipitation of fine α particles not by the presence of the ω phase.

- Zafari and Xia [118] investigated another metastable β Ti alloy (Ti5Al15V5Mo3Cr – Ti5553) subjected to HPT deformation. They claimed that SPD enhances recrystallization of β grains upon heating with a high heating rate (> 100 °C/min) which is followed by nucleation and growth of the α phase. Slower heating rate can result in nucleation of α particles without recrystallization, provided element partitioning occurs.
- Jiang et al. have recently studied the Ti5553 alloy subjected to HPT deformation [119]. They observed equiaxed α particle formation in severely deformed material and claimed that segregation of the β stabilizers near α/β interfaces in the UFG structure blocks diffusion of atoms. Therefore, the growth of α precipitates is hindered, which results in equiaxed and small particles.

Nevertheless, to our best knowledge, direct comparison and discussion of phase transformations occurring in non-deformed and deformed metastable β Ti alloy using in-situ methods have not yet been performed.

2 AIMS OF THE THESIS

The ultimate goal of the research presented in this work is to investigate the effect of severe plastic deformation on phase transformations in the metastable β Ti15Mo alloy upon thermal treatment.

The study focuses in detail on:

- Characterization of the effect of severe plastic deformation on the microstructure of the alloy.
- Analysis of the ageing response of the Ti15Mo alloy processed by severe plastic deformation.
- Comparison of phase transformations in Ti15Mo alloy occurring upon heating in non-deformed and deformed materials.
- Investigation of the enhanced precipitation of the α phase in a severely deformed alloy.

3 EXPERIMENTAL MATERIAL AND METHODS

3.1 Experimental material

A simple binary metastable β Ti alloy, Ti15Mo, was used for this research. It contains 15 wt.% of molybdenum and a negligible amount of other elements. The exact chemical composition of the alloy is summarized in Table 3.1 [120]. Main advantages of this alloy are its exceptional corrosion resistance, low elastic modulus, high strength, good fatigue resistance and good ductility [121].

Table 3.1 Chemical composition of the Ti15Mo alloy [120].

Element	Chemical composition (wt.%)
H ₂	0.001
N ₂	0.014
O ₂	0.185
Fe	0.030
C	0.007
Mo	15.200
Si	0.090
Ti	Balance

The alloy was supplied by Carpenter Co., USA in the form of a rod with the diameter of approx. 10 mm. The received material was solution treated (ST) in an inert Ar atmosphere at the temperature of 810 °C for 4 hours and subsequently quenched in water. The ST material was subjected to severe plastic deformation by HPT and ECAP at USATU, Russian Federation. The effect of the severely deformed and UFG microstructure on phase transformations was thoroughly investigated using advanced experimental methods. The microstructure was studied by scanning and transmission electron microscopy. The evolution of phase composition and the evolution of lattice defects were studied using X-ray diffraction and positron annihilation spectroscopy, respectively.

3.1.1 High pressure torsion

Cylindrical samples with the diameter of approx. 10 mm and the height of approx. 5 mm were cut from the ST material and subjected to HPT deformation at room temperature. First, the cylinders were pressed with 6 GPa to achieve disk-shaped samples with the diameter of 20 mm and the thickness of approx. 1 mm. Consequently, the specimens were deformed in torsion by rotating one of the anvils. For this study,

samples after $N = 1$ HPT revolutions were prepared (hereafter referred as HPT samples). Due to heterogeneous nature of the deformation, the equivalent imposed deformation calculated according to equation (1.11) ranges from 0 to 36 from the center to the periphery part of the sample.

3.1.2 Equal channel angular pressing

The ST material was subjected to $N = 2$ ECAP passes (hereafter referred as ECAP samples). Deformation by ECAP was performed at the elevated temperature of 250 °C in a die with the channels angle of $\Phi = 120^\circ$ and $\psi = 0^\circ$ (see Figure 1.6). The equivalent (von Mises) strain determined using equation (1.12) was 1.33.

3.1.3 Ageing and heat treatments

Two kinds of heat treatment were performed to assess the details of phase transitions:

- 1) Isothermal annealing (ageing) at temperatures 400 °C and 500 °C for 1, 4 and 16 hours was carried out in a preheated molten salt bath to avoid oxygen contamination and to ensure a high heating rate; the samples were subsequently quenched in water.
- 2) Thermal treatment using linear heating was carried out in a furnace with a controlled heating rate of 5 °C/min. Samples heated to temperatures 350 °C, 500 °C and 650 °C were sealed in a quartz tube in Ar atmosphere to avoid contamination. After reaching the desired temperature, the sample was immediately quenched in water.

3.2 Experimental methods

3.2.1 Scanning electron microscopy

An extensive microstructural observation was performed using scanning electron microscopy (SEM). An accelerated electron beam having a high energy (usually 20 keV) interacts with atoms of the specimen. Several types of signals are created and those emitted from the specimen surface can be detected by different detectors. These signals contain valuable information about the microstructure and topography of the specimen. Among the several types of signals, back-scattered and secondary electrons are the most important for this research.

Back-scattered electrons (BSE) are primary beam electrons which were reflected by elastic interactions with atoms of the specimen. Elements with a higher atomic number scatter electrons more strongly than light elements; therefore, the

number of BSE is higher and the regions with heavier elements appear brighter in a BSE image. For that reason, BSE reflect the chemical contrast of the specimen (so-called Z-contrast). Furthermore, the amount of BSE also depends on the local crystallographic orientation. It can be assumed that the crystal lattice can be viewed as channels or paths through which electrons of the primary beam can penetrate to a greater depth before scattering. Hence, certain orientations of the crystal lattice will backscatter more electrons than others – the obtained so-called electron channeling patterns provide a direct information about grain orientation relative to the incident beam.

Secondary electrons (SE) are generated by inelastic scattering of the primary beam with the outer electron shell of specimen atoms. As the solid specimen is a heavily absorbing medium, only electrons from atoms which lie near the specimen surface may be detected. The information about the topography of the specimen may be therefore obtained from the SE signal. More SE tend to be emitted from steep surfaces and ledges, thus they appear brighter.

An electron from the primary beam can also interact with inner electron shells of an atom, ejecting an electron from its orbital. This vacancy in the inner electron shell is usually very quickly filled by a higher energy electron from an outer shell. The difference in the energy of these two electrons can be released in two ways. Firstly, in the Auger process, the energy is used to eject another outer shell electron. Secondly, in the characteristic X-ray process, the energy difference is released in the form of an X-ray signal. The energies and quantities of characteristic X-rays are measured by an analytical technique called energy dispersive X-ray spectroscopy (EDS or EDX). The elemental composition of the specimen can be determined by EDS, as the energies of individual shell electrons are characteristic for a particular atom.

3.2.1.1 Electron backscatter diffraction

Electron backscatter diffraction (EBSD) is a microstructural technique which allows the determination of the crystallographic structure and orientation of grains. Moreover, the misorientation of individual grains, grain boundary character, texture, and many other microstructural features can be analyzed from EBSD data. The primary electron beam may be inelastically scattered on some inhomogeneities of the specimen structure. These inelastically scattered electrons may be further elastically diffracted by the crystal structure of the sample and form so-called Kikuchi bands on the detector

screen. Such analysis is performed automatically at individual points of the sample surface, acquired Kikuchi patterns are processed (indexed), and the crystallographic orientation of individual points is automatically determined by the EBSD postprocessing software (e.g. HKL Oxford Instruments and/or EDAX).

In order to perform the EBSD mapping in SEM, a polished specimen is mounted to the holder with a tilt angle of 70°. The tilt to 70° ensures a large and elongated interaction volume from which electrons are emitted (see Figure 3.1). The size of the interaction volume limits the resolution of the EBSD. Spatial resolution differs in lateral and longitudinal directions and strongly depends on the material. The best achieved resolution of 34.5 nm was obtained in Cu using accelerating voltage of 10 kV [122].

Sample preparation for standard SEM observation included grinding on SiC emery papers of progressively finer grit up to 2000 followed by three step vibratory polishing. In some cases, additional polishing was required using Leica EM RES102 ion polisher. The same specimens were used for EBSD observation and SEM imaging.

3.2.1.2 *Transmission Kikuchi diffraction /transmission electron backscattered diffraction*

In their study, Keller and Geis [123] suggested an alternative method to improve the spatial resolution of the EBSD, the so-called transmission EBSD (tEBSD)¹ or transmission Kikuchi diffraction (TKD).

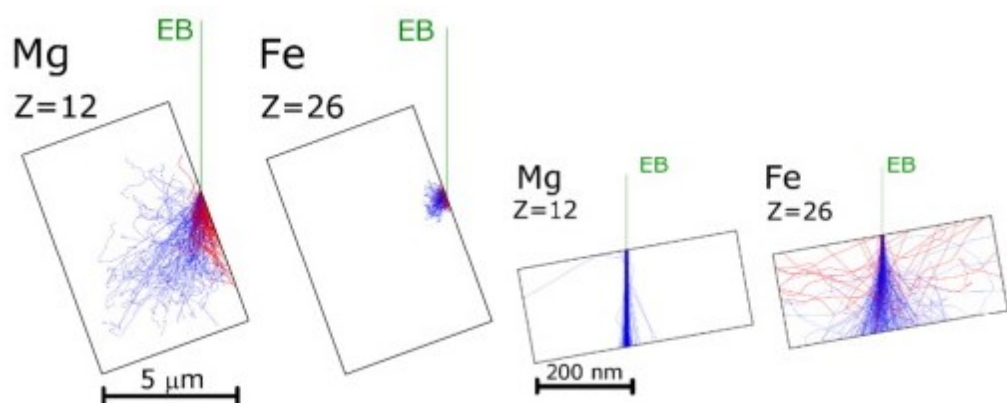


Figure 3.1 Simulated electron trajectories in EBSD and TKD configurations at 20 kV. Red trajectories show back-scattered electrons, blue ones transmitted electrons or those which do not leave the material. Note the significantly different scale of the images [124].

¹Both names – tEBSD and TKD - are used. In the following, the latter term will be used, since it is formally correct (comparing with “transmission . . . back-scattered”).

The TKD measurement can be carried out in a conventional SEM equipped with an EBSD camera. A thin specimen transparent for electrons at typical SEM energies or a lamella for transmission electron microscopy (TEM) observation must be used. Focused ion beam (FIB) employing Ga ions for nano- and micromilling can be used for site-specific preparation of lamellae suitable for TKD (and also for TEM). During preparation of the sample, Pt was first deposited on the surface of the sample using gas injection system (GIS). This layer formed the top surface of the lamella and protected it during milling process. The lamella is then cut out, mounted to the holder, and gradually thinned using FIB until it reaches the final thickness of $\sim 100 - 200$ nm.

The data acquisition, processing and pattern indexing is the same as for conventional EBSD. Contrary to the conventional EBSD, electrons do not have to be back-scattered to be detected. In TKD, primary electron is first scattered (forward scattered) and then diffracted. A transparent specimen is tilted by 20° with respect to the primary beam in our setup (as shown in Figure 3.2). TKD reduces the interaction volume because the electron beam leaves the sample before it can be significantly widened (Figure 3.1). Therefore, TKD allows a spatial resolution as good as 2.5 nm (this value is valid for Cu) [125].

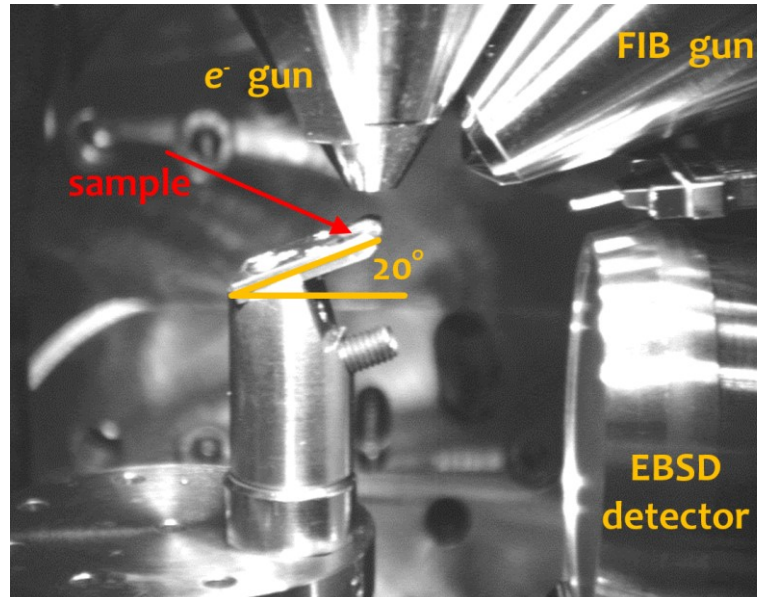


Figure 3.2 Inside view of the Zeiss Auriga Compact FIB-SEM chamber with the setup for TKD [126].

A scanning electron microscope Zeiss Auriga Compact CrossBeam equipped with field emission gun (FEG), FIB, GIS, EBSD, and EDS detector was used for microstructural observations and sample preparation. For SEM, EBSD, and EDS

measurements the accelerating voltage of 10 kV was employed, while the accelerating voltage of 30 kV was used for TKD measurement.

3.2.2 Transmission electron microscopy

Detailed microstructural observations of the samples were performed using transmission electron microscopy (TEM). TEM is technique for microstructural observation using a high energy electron beam which are emitted from the heated cathode and subsequently accelerated by the gradient of electric field between the cathode and anode to reach the energy of several hundreds of electronvolts (usually 200 keV). The path of electron beam is further controlled by a set of electromagnetic coils, called lenses. In the upper part of the microscope, electrons pass through the system of condenser lenses which focus it on the specimen. Specimens (thin foils) with large transparent areas (the thickness varies between 150 – 250 nm depending on the material) for electrons are required.

In the TEM the specimen is placed in the pole pieces of the objective lens (OL) which displays the result of the interaction of electrons with the specimen. In the back focal plane of the OL the diffraction pattern, i.e. the result of the diffraction of the electron beam with the crystal lattice of the specimen is formed while the virtual enlarged image of the specimen structure is formed in the back image plane of the OL. The image, i.e. the distribution of the intensity of electron beam on the lower surface of the specimen, is further magnified in the lower part of the microscope (consisting of the set of intermediate lens and the projector) and projected to the fluorescent screen and/or charge-coupled device (CCD) camera. If the studied specimen has a crystal structure, the diffraction pattern may be also projected on the screen giving the second function of the microscope – the diffractograph.

The specimen is placed in the holder allowing its tilting (usually in two axes) to the required orientation, i.e. placing the particular crystal plane perpendicular to the electron beam. In most cases so called two-beam condition is employed, i.e. one primary beam and one diffracted beam are allowed to form the image. Only one of these two beams is selected, i.e. allowed to pass through the objective lens providing the bright field (BF) image and dark field (DF) image if the former and or latter beam is used for the imaging of the crystal structure, respectively. In the conventional TEM lattice defects (line defects – e.g. dislocations, plane defects – e.g. grain and/or phase boundaries, and bulk defects – e.g. precipitates) may be observed as their presence in

the specimen causes the distortion of the lattice and thus the deflection of the path of electron beam with respect to the ideal crystal lattice resulting in the typical contrast for each of these defects – so called diffraction contrast. Therefore, the alternative work in a diffraction mode provides an information about the specimen orientation and in the image mode, is needed to get the detail information about the microstructure of the studied specimen.

3.2.2.1 Automated crystallographic orientation mapping in TEM

Automated crystal orientation mapping in a TEM (ACOM-TEM) is an effective technique for mapping phases and grain orientations of a sample. A selected area is scanned with the focused primary beam and electron diffraction patterns are collected using a camera. Every diffraction pattern is compared to the pre-calculated templates (for a given crystalline phase, lattice parameters and orientation) and the best match is selected. A map of crystal orientations, similar to an inverse pole figure orientation map in EBSD, is achieved by ACOM-TEM. The main difference from EBSD is that in ACOM-TEM, point diffraction patterns are analyzed instead of Kikuchi lines. The method represents a powerful tool for microstructural characterization for UFG or nano-grained materials, where high resolution is required.

ACOM-TEM method was first introduced by Schwarzer et al. in 1994 [127], while an ACOM-TEM device was developed by E. Rauch [128].

Thin samples for TEM observation were prepared by three consecutive steps – mechanical grinding and polishing, electrolytical polishing and ion polishing. The mechanical grinding of the sample slices up to the thickness of 0.3 mm was done using SiC emery papers. Disks with a diameter of 2.7 mm were then cut using a Gatan puncher and subsequently grinded using fine emery papers (1200 grit) to the final thickness of 100 – 150 μm . The disks were subsequently pre-electropolished using a Tenupol 5 unit for 1 min employing the solution of 6% HClO_4 + 33% $\text{C}_4\text{H}_{10}\text{O}$ + 61% CH_3OH at the temperature of $-20\text{ }^\circ\text{C}$. The final step was ion polishing using a Leica EM RES102 ion polisher until a small hole in the center of the sample was formed (sufficiently large thin areas transparent for electrons were formed in the vicinity of the hole by this procedure). Alternatively, samples from a selected area were prepared by FIB in SEM (described in Section 3.2.1).

The TEM microscope JEOL 2200 FS equipped with selected area electron diffraction (SAED) detector and ACOM-TEM operated at 200 kV was used for microstructure investigation.

3.2.3 X-ray diffraction

In order to characterize the phase composition of the samples (polycrystals), X-ray powder diffraction (XRD) measurements were carried out. XRD is based on elastic scattering of X-rays on the periodic crystal structure of a sample. The constructive interference of scattered photons occurs when Bragg's law is satisfied:

$$n\lambda = 2d_{hkl}\sin\theta, \quad (3.1)$$

where n is an integer which denotes the order of diffraction, λ is the wavelength, d_{hkl} is the interplanar distance, and θ is half of the angle between the incident and the reflected beam.

The dependence of the intensity of diffracted X-rays on the angle 2θ is measured. Diffraction patterns show peaks corresponding to various plane systems of a crystal. In addition, the deviations of the peak intensity from random grain distribution characterizes the possible preferred orientation of grains. Finally, detailed analysis of peak broadening allows the determination of microstrain, crystallite size and dislocation density.

3.2.3.1 Standard X-ray diffraction

XRD of non-deformed and ECAP-deformed Ti15Mo alloy was measured at the Department of Physics of Condensed Matter at Charles University employing a Bruker D8 Advance powder X-ray diffractometer using Cu K_α radiation, with a variable divergent slit and a Sol X detector. Diffraction patterns were collected at room temperature in the 2θ range from 30° to 130° with a step size of 0.02° and an exposure time of 5 s/step.

XRD measurements of the HPT-deformed Ti15Mo alloy were carried out in the periphery part of the samples on Bruker D8 Discover powder X-ray diffractometer at the Institute of Plasma Physics, Czech Academy of Sciences. Vertical Bragg-Brentano geometry (2.5° Soller slits in both primary and secondary beam and 0.24° divergence slit) with filtered Cu K_α radiation was used. The XRD patterns were acquired by scanning the 2θ region from 20° to 135° with a step of 0.04° and acquisition time of 1.5 s/step.

Measured patterns suffered from strong preferred orientation and therefore were fitted and refined using the Le Bail algorithm. Pseudo-Voigt profile of peaks was assumed and ten terms of Legendre polynomials for the background were used. The refinement using the program Jana2006 [129] was done in a couple of consecutive steps. Two phases, β and ω , were considered for non-deformed and deformed conditions, while for some samples after thermal treatment, α phase was also included in the fit. Refinement of β phase parameters was done first, followed by refinement of less intense ω phase peaks and α phase. All parameters were finally refined together to achieve the best possible fit. Note that this approach does not allow quantitative determination of volume fraction of individual phases due to preferred orientation of grains, poor statistics, and a coincidence of the β and ω peaks.

3.2.3.2 High energy synchrotron X-ray diffraction

High energy synchrotron X-ray diffraction (HEXRD) was carried out at the P07-HEMS beamline of PETRA III (Deutsches Elektronen-Synchrotron) [130] using the energy of 100 keV ($\lambda = 0.124 \text{ \AA}$). Patterns of entire Debye-Scherrer rings were acquired using a PerkinElmer XRD 1621 image plate detector. The samples were fixed during acquisition and measured 5 mm from the centre of the sample with an incident beam limited by slits to the size of $1 \times 1 \text{ mm}^2$. Obtained diffraction patterns were processed by TOPAS v5 (Bruker AXS) software for Rietveld structural refinement. Samples after HPT exhibited strong texture; therefore, the patterns were treated by March-Dollase approach [131]. The refinement was performed using software FullProf [132].

Diffraction patterns were acquired at room temperature during an ex-situ measurement. An in-situ measurement during heating was performed with the constant heating rate of $5 \text{ }^\circ\text{C}/\text{min}$ from room temperature up to $800 \text{ }^\circ\text{C}$, while XRD patterns were acquired every 15 s and processed using software Matlab.

3.3 Positron annihilation spectroscopy

Positron annihilation spectroscopy (PAS) was used to determine the density of dislocations and concentration of vacancies in the specimen. The measurement is based on the well-known physical phenomenon that a positron annihilates after meeting an electron. Each annihilation event is accompanied by emission of two gamma photons which can be detected. Radioactive source Na^{22} decays by a β^+ -decay during which a positron is created. Simultaneously, the source emits a gamma photon

that serves as a start signal. The high energy positron enters the sample and within tens of ps (depending on the material) its energy decreases due to interaction with sample atoms to the energy of the ambient temperature, so-called thermalization. After thermalization, the positron diffuses in the lattice until it meets an electron and annihilates. During annihilation, two gamma photons are emitted and detected, providing the end signal of the measurement – the time between start and stop signal corresponds to the lifetime of the positron. In a defect-free sample with comparatively high electron density, the probability to meet an electron is high and the lifetime of the positron is short. In this case the positron is delocalized (free positron). Lattice defects can act as potential wells (traps) and the positron is localized in the defect where electron density is comparatively lower. As a result, the positron trapped at a defect has a longer mean lifetime. Hence, the mean positron lifetime strongly correlates with the concentration of lattice defects. The measured spectrum of lifetimes of positrons can be decomposed into individual components with different mean lifetimes with the use of the two-state simple trapping model (STM) [133]. This model assumes that only trapping of the thermalized positrons occurs, the release of the trapped positrons does not take place, and defects are distributed homogeneously in the sample. Different types of defects can be associated with specific mean lifetimes – components. Intensities of the components provide information on the concentration/density of individual lattice defects.

3.4 Electrical resistance measurement

Electrical resistance measurement was carried out in order to characterize the structural changes and phase transformations in the material during heating. The measurements were performed employing a self-made apparatus, described in detail elsewhere [134]. The four-point method of electrical resistance measurement and rapid commutation of direct current were implemented in order to minimize parasitic effects. For the measurement of voltage and current a high precision nanovoltmeter Keithley 2182A and SourceMeter Keithley 2400 devices were used, respectively, achieving the relative error lower than 0.0001 at each measured point and relatively fast acquisition rate of 2 points/second.

Electrical resistance was measured during linear heating with the heating rate of 5 °C/min up to temperature of 750 °C. The specific electrical resistivity cannot be calculated due to the complicated shape of the sample; therefore, only the absolute

resistance (R) was evaluated. The relative resistance with respect to the resistance at the ambient temperature (R_0) was computed in order to compare the results between different samples

$$\text{Relative resistance} = \frac{R}{R_0}, \quad (3.2)$$

where R_0 is the absolute electrical resistance of the specimen at the temperature of 40 °C.

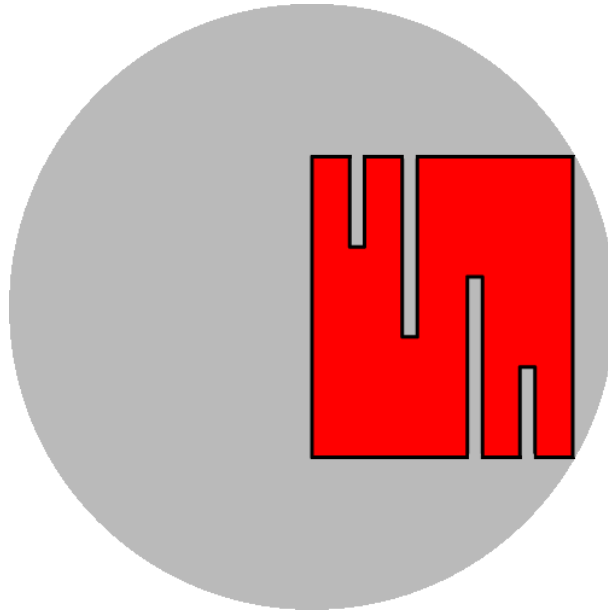


Figure 3.3 Schematic representation of a sample prepared for measurement of electrical resistance from an HPT sample (the sample has a shape of a disk with a diameter of 20 mm).

Samples for electrical resistance measurement are flat, typically 1 mm thick and their shape is adjusted to maximize the effective length of the sample and thus to increase the precision of resistance measurement (see example in Figure 3.3 – this is so-called N-shaped sample). Specimens from non-deformed material were prepared from a longitudinal section of the ST rod. Preparation from the HPT material is schematically shown in Figure 3.3 (note that deformation through HPT sample is the lowest in the center of the disk and therefore the sample is intentionally not centered). Each sample with the thickness ~ 0.7 mm was grinded using Struers SiC emery papers up to 800 grit. Four contacts made from CP Ti wire were spot-welded on the sample.

3.5 Microhardness measurement

The main aim of the microhardness testing by Vickers hardness is to determine mechanical properties of the material. Note that tensile and compression tests could

not be performed due to the small size of the specimens, especially in the case of HPT samples.

A diamond indenter in the form of a square pyramid and with the top angle between sides equal to 136° (Vickers indenter) is pressed to the flat surface of the specimen using a controlled load. An indent left in the sample has a surface area A which can be determined by the formula

$$A = \frac{d^2}{2 \sin\left(\frac{136^\circ}{2}\right)} \approx \frac{d^2}{1.8544}, \quad (3.3)$$

where d is the average length of the diagonal of the indent.

The resulting microhardness (value of HV) is determined by the ratio F/A

$$HV = \frac{F}{A} \approx \frac{1.854F}{d^2}, \quad (3.4)$$

where F is the applied force in kilogram-force (kgf). Therefore, the physical unit of such HV is kgf/mm^2 . In order to get the HV value in MPa, it should be multiplied by 9.81 (standard gravity).

Microhardness measurements were performed using a microhardness tester Qness Q10a by the Vickers method with 0.5 kg load (HV 0.5).

Note, that SEM, XRD and PAS methods are non-destructive and therefore all these measurements were done consecutively on the same set of samples. These samples were ultimately used for microhardness measurement.

4 RESULTS

The chapter Results is divided into 4 subchapters. The first part is dedicated to the characterization of the initial material, namely to Ti15Mo alloy in the non-deformed, solution treated condition and after severe plastic deformation by HPT ($N = 1$ turn) and ECAP ($N = 2$ passes). The second part characterizes precipitation of the α phase in the non-deformed and both deformed conditions upon ageing using ex-situ methods. Electrical resistivity, X-ray diffraction using synchrotron radiation and transmission electron microscopy were used for in-situ observation of phase transformations in the non-deformed and HPT-processed material and achieved results are described in detail in the third subchapter. Based on the in-situ results, a specific thermal treatment was selected and the HPT material after this treatment was thoroughly characterized. Results of microstructure and phase composition characterization of the material after the dedicated thermal treatment are presented in the last subchapter.

4.1 Initial material

In this section, the initial microstructure, phase composition, and microhardness of the non-deformed (after solution treatment) and deformed (after HPT and after ECAP) Ti15Mo alloy is characterized.

4.1.1 Ti15Mo in solution treated condition

The initial microstructure of the ST Ti15Mo alloy is shown in Figure 4.1. A coarse-grained (CG) structure with the grain size $\sim 50 \mu\text{m}$ is well visible due to the channeling contrast. In addition, darker and brighter areas are also visible in the material due to the chemical contrast in the BSE micrograph (pointed out by yellow arrows in Figure 4.1). These chemical inhomogeneities were investigated by EDS. The results of the EDS point analysis are summarized in Table 4.1. It must be noted that EDS results are not fully reliable in terms of exact quantitative Mo content. Nevertheless, the relative difference in chemical composition between different areas is unambiguous and accurate.

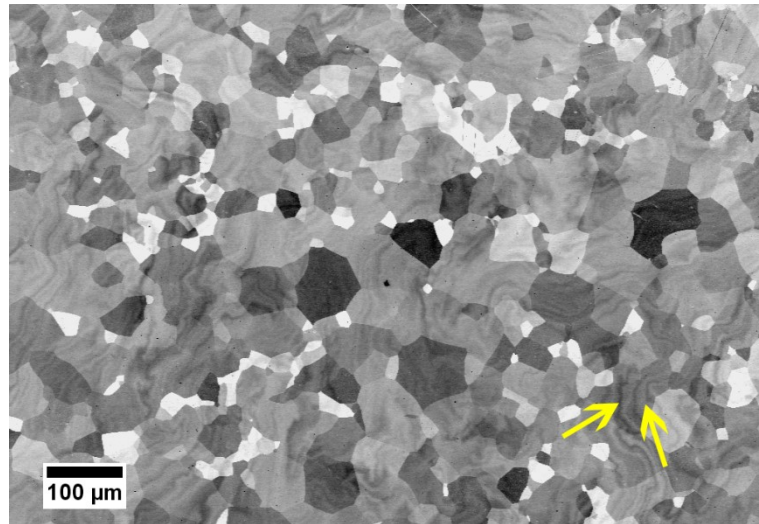


Figure 4.1 SEM–BSE micrograph of the solution treated Ti15Mo alloy (the yellow arrows indicate chemical inhomogeneities in the material).

Table 4.1 Chemical composition of the darker and brighter bands (chemical inhomogeneities, see yellow arrows in Figure 4.1) measured by EDS.

	Brighter part (wt.%)	Darker part (wt.%)
Ti	83.3 ± 0.5	85.7 ± 0.4
Mo	16.7 ± 0.5	14.3 ± 0.4

Additionally, an EDS mapping was performed in order to study the local chemical inhomogeneities in the ST material. Figure 4.2(a) shows a few β -grains visible due to channeling contrast and darker and lighter areas (visible especially in the top left corner of the image) which are distinguishable due to chemical contrast (Z-contrast). EDS mapping confirms the chemical inhomogeneity - darker areas in Figure 4.2(a) contain less Mo as shown in Figure 4.2(b). This difference in the local content of Mo (β stabilizing element) may affect the phase stability of the β phase matrix.

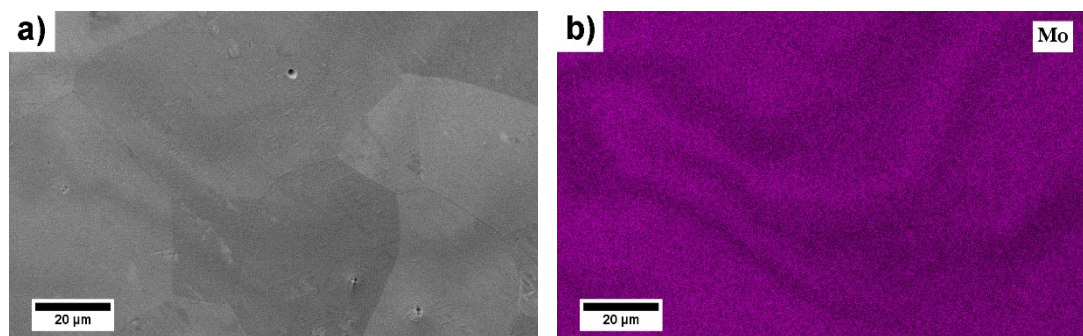


Figure 4.2 Local chemical inhomogeneities in ST Ti15Mo alloy: (a) SEM–SE micrograph of the area of interest, (b) corresponding element map of Mo using EDS.

4.1.2 Ti15Mo processed by HPT

The Ti15Mo alloy after solution treatment was subjected to HPT at room temperature. The microstructure of the Ti15Mo alloy after HPT deformation was thoroughly investigated in my Master thesis [105] and published in papers [95, 106, 107, 135]. The microstructure of this highly deformed material was observed using both scanning and transmission electron microscopy. All measurements were performed in the periphery part of the sample where the strain imposed by HPT reaches the highest values.

4.1.2.1 Scanning electron microscopy

The fine grain structure of the material after $N = 1$ HPT turn could not be observed by SEM due to its limited resolution. Nevertheless, the SEM–BSE micrograph in Figure 4.3 clearly shows chemical inhomogeneities (note that the black dots in the image are polishing artifacts), which was confirmed by EDS analysis. Darker areas with lower Mo content form curly bands in the ST material (Figure 4.1), while after HPT deformation they appear as straight bands elongated in the direction of the deformation (Figure 4.3).

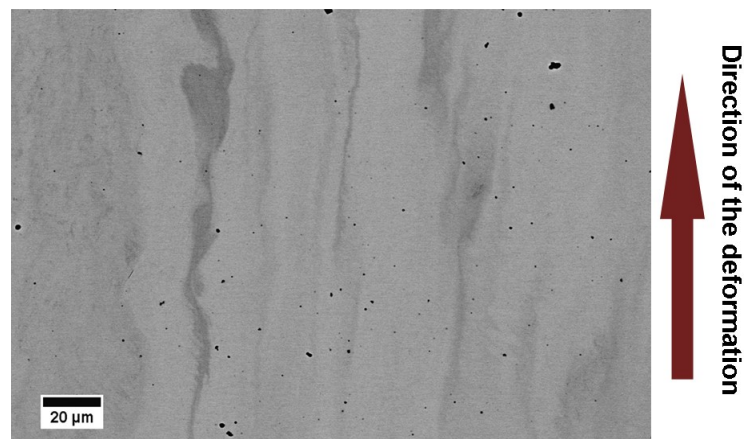


Figure 4.3 SEM–BSE micrograph of Ti15Mo alloy after HPT processing. Darker and brighter areas are caused by the difference in chemical composition (black dots are polishing artifacts).

4.1.2.2 Transmission electron microscopy

As the microstructure cannot be properly studied by SEM, an investigation using TEM was needed.

The TEM BF image in Figure 4.4(a) shows the microstructure of the HPT-processed Ti15Mo alloy after $N = 1$ HPT turn. The non-uniform contrast of grains

in the BF image is associated with the distortion of the lattice and with high density of dislocations [115]. The same non-uniform contrast is also visible in the TEM DF image shown in Figure 4.4(b) (acquired using a selected β phase reflection), where the individual β grains cannot be distinguished due to severe deformation. Hence, the exact grain size cannot be estimated from the DF image, but it can be assumed that it is below 100 nm. The phase composition was determined using SAED – see Figure 4.4(c). It was confirmed that the HPT sample contains both β and ω phases. The distortion of the individual spots in SAED pattern suggests a highly deformed and fragmented β matrix with a strong texture in the direction $[111]_{\beta}$.

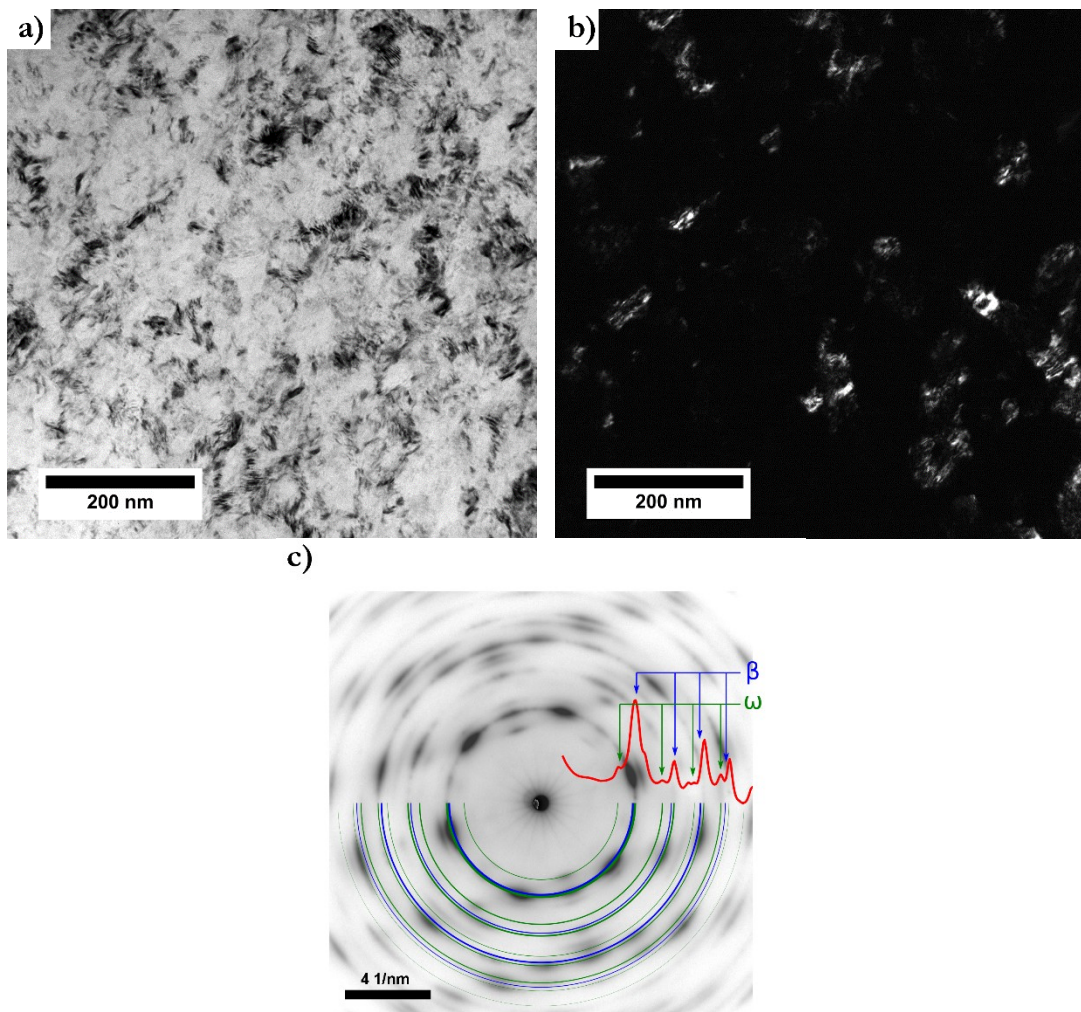


Figure 4.4 (a) TEM BF image, (b) TEM DF image, and (c) the corresponding SAED pattern of the Ti15Mo alloy after $N = 1$ revolution of HPT – periphery part of the sample.

4.1.3 Ti15Mo processed by ECAP

Alternatively, the ST Ti15Mo alloy was deformed using ECAP. The microstructure and mechanical properties of the ECAP material have been already thoroughly studied

in our previous research [136]. For the purpose of the investigation of phase transformations in the ECAP material, sample after $N = 2$ ECAP passes was chosen. The microstructure of this specimen is briefly described in the following sections.

4.1.3.1 Scanning electron microscopy

The microstructure of the ECAP specimens after $N = 2$ ECAP passes was studied by EBSD. Figure 4.5(a) and (b) shows the inverse pole figure (IPF) maps of the ECAP sample parallel to rolling and normal directions of the ECAP, respectively. The IPF maps indicate a highly deformed, but not UFG structure of the material. The black areas could not be successfully indexed (i.e. the crystallographic orientation could not be determined) due to poor quality of diffraction patterns, which suggests a large stored deformation. The interiors of grains are heavily deformed, which can be inferred from continuous changes of orientation (color) within individual grains. The activity of the twinning process during ECAP deformation is also visible in Figure 4.5; examples of twins are highlighted by arrows. Twinning in the system $\{112\} \langle 111 \rangle$ was determined from the misorientation and is consistent with our previous finding for Ti15Mo alloy [135]. The interior of the observed twins is also heavily deformed.

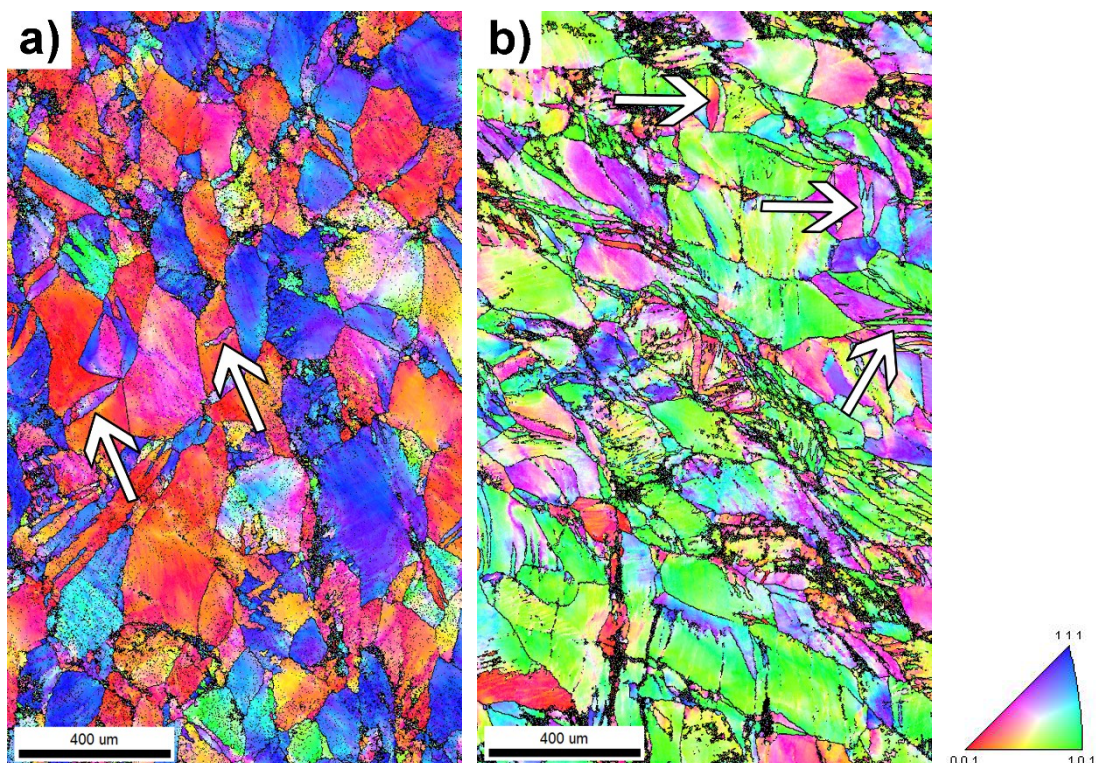


Figure 4.5 IPF maps of ECAP samples in (a) rolling and (b) normal direction of the deformation and the corresponding orientation triangle for bcc structure. The white arrows indicate twins.

4.1.3.2 Transmission electron microscopy

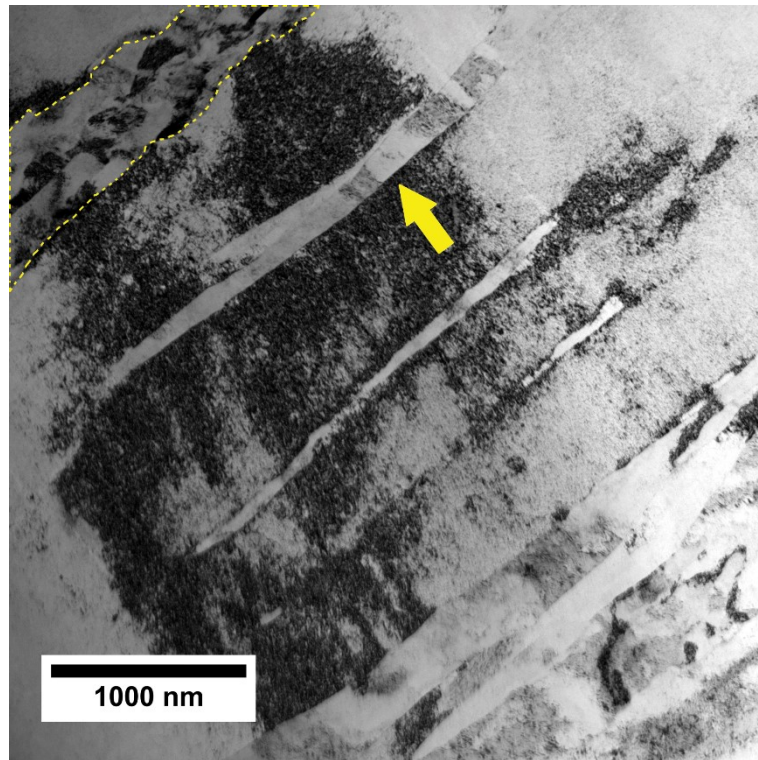


Figure 4.6 TEM BF image of the microstructure of Ti15Mo alloy after $N = 2$ ECAP passes.

The deformed microstructure in a plane parallel to the rolling direction was studied in detail by TEM. In the TEM BF image (Figure 4.6) a severely deformed grain is shown. The observed grain contains a high dislocation density and is twinned – one of the twins is marked by a yellow arrow. Note that the twin can also include dislocations, but those are not in diffraction condition and therefore are not visible. In the upper left corner of the image (highlighted by a yellow dashed line), an area containing a high dislocation density – so-called shear band (SB) – is visible [137]. Figure 4.7(a) shows the $[110]_{\beta}$ zone axis electron diffraction pattern from the coarse β grain shown in Figure 4.6. SAED pattern contains ω phase reflections at $1/3$ and $2/3$ $\{112\}_{\beta}$ positions. TEM DF image from one of the ω phase reflections (highlighted by the yellow circle in Figure 4.7(a)) is shown in Figure 4.7(b); nanometer-sized ω phase particles can be observed. However, neither the volume fraction nor the exact size can be determined from TEM images due to limited resolution. Note also that only one of the possible four ω variants is visible in Figure 4.7(b), because only one diffraction spot corresponding to a single ω variants was selected in the SAED pattern.

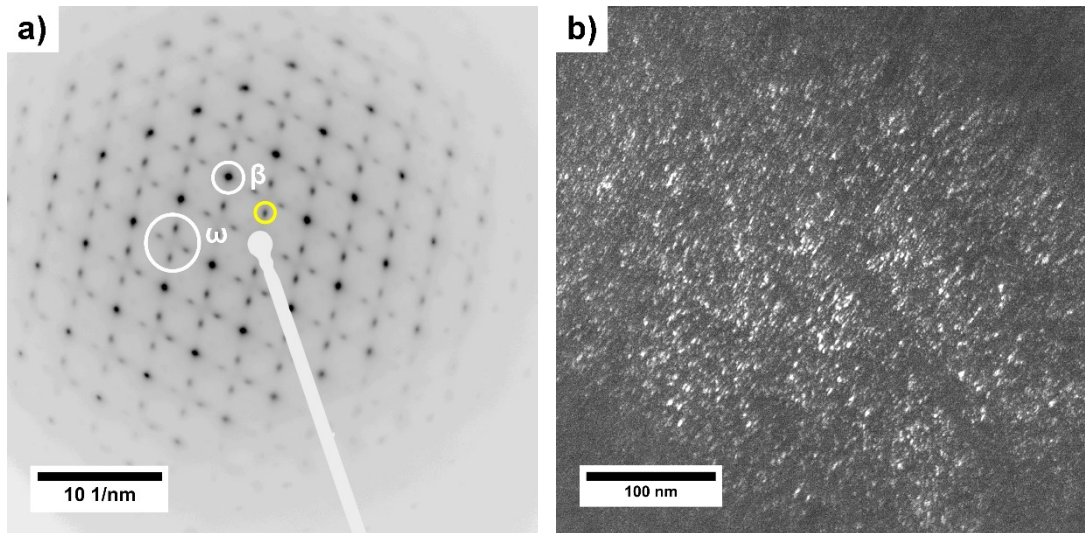


Figure 4.7 (a) SAED pattern in the $[110]_{\beta}$ zone axis showing reflections from the parent β matrix and ω phase particles and (b) TEM DF image displaying ω phase particles.

4.1.4 Phase composition of the initial materials

4.1.4.1 X-ray diffraction measurement

The phase composition of the Ti15Mo alloy in the solution treated (hereafter referred to as non-deformed) condition and in the two deformed conditions was studied using XRD. The measured (black curve) and fitted (colored curves) XRD patterns of all three conditions are shown in Figure 4.8(a). The interplanar distance is displayed on the horizontal axis, while the y-axis shows the intensity in a logarithmic scale, in order to distinguish even a small contributions of individual phases (especially that of the ω phase). The most noteworthy peaks of the ω phase are indicated with open arrows. For a better visibility, the same XRD pattern as displayed in Figure 4.8(a) is shown in Figure 4.8(b) in detail (the x-axis is in range of $d_{hkl} = (1.1-1.5) \text{ \AA}$). A quantitative determination of phase content from a standard laboratory XRD is not possible since both non-deformed and ECAP conditions contain large grains with the size of hundreds of micrometres. Moreover, all three conditions have distinctive preferred orientation of grains, which can be inferred from the relative intensity of the peaks. These facts complicate the quantitative analysis of the XRD patterns and only qualitative conclusions can be therefore made.

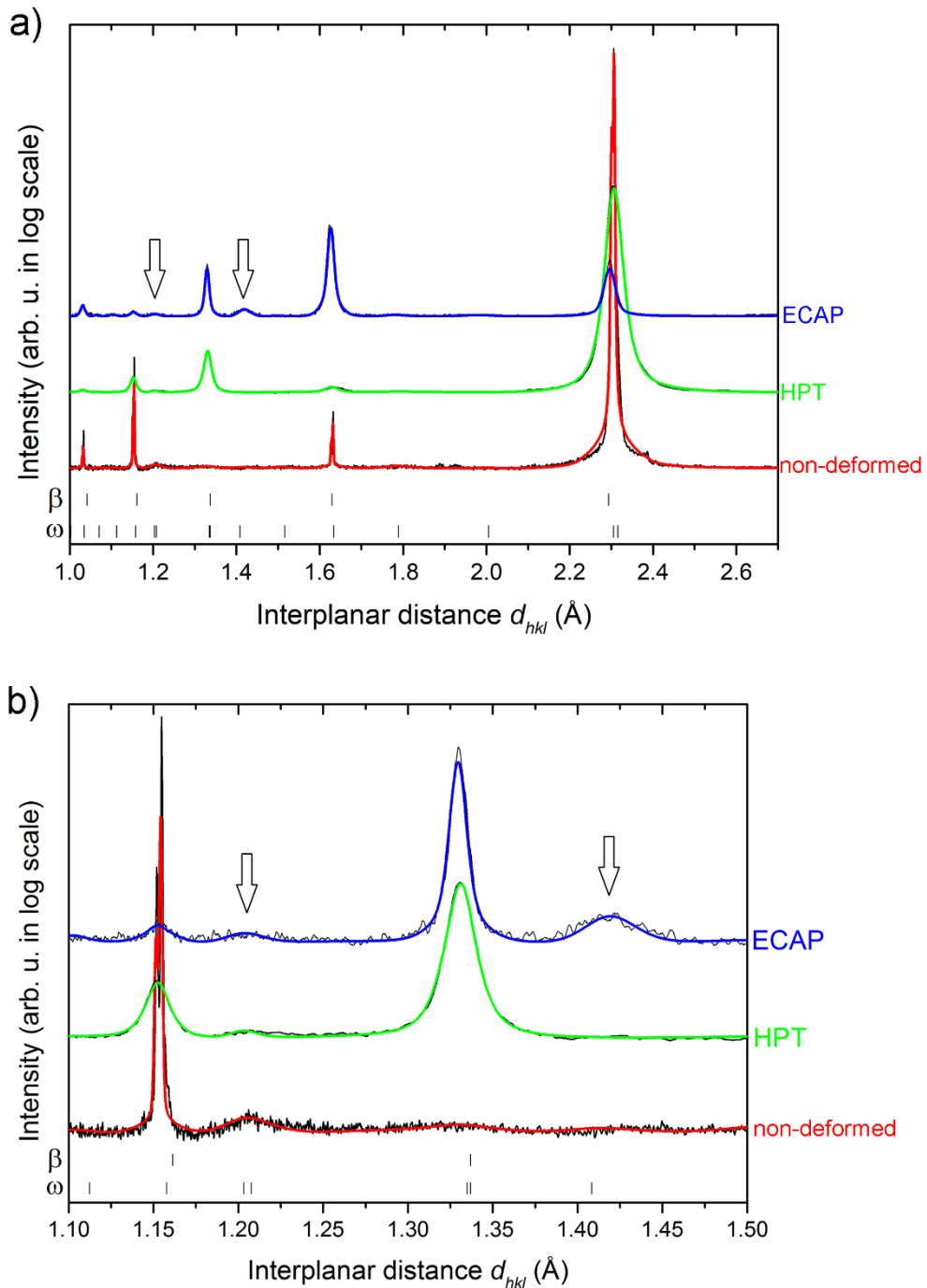


Figure 4.8 (a) XRD patterns and (b) detailed XRD patterns of the non-deformed, HPT-processed and ECAP-processed materials. The XRD patterns are vertically shifted for clarity. The most noteworthy peaks of the ω phase are indicated with open arrows.

The non-deformed Ti15Mo alloy contains both β and ω phase. Determination of the ω phase contribution is not straightforward due to overlapping peaks of the β and ω phase. Nevertheless, a small ω peak is visible at $d_{hkl} \approx 1.2 \text{ \AA}$ (the positions of visible ω peaks are indicated with open arrows in Figure 4.8). The XRD pattern of the materials after deformation (HPT and ECAP) exhibits significantly broadened peaks

due to increased dislocation density and reduced crystallite size in the severely deformed material (green and blue curves in Figure 4.8, respectively). Furthermore, due to residual stresses in the deformed material, the peaks are slightly shifted to different values of interplanar distances – the direction of the shift depends on the type of the residual stress [138].

The ω phase content seems to be lower in the HPT sample compared to the non-deformed one; only a small peak is visible at the interplanar distance $d_{hkl} \approx 1.2 \text{ \AA}$. At the same time, the peaks of the ω phase can coincide with the peaks of the β phase. It was previously proved (see Figure 4.4(c)) by TEM that the ω phase is also present in the HPT material; however, its exact volume fraction cannot be determined from standard XRD.

As it can be observed from the intensity of the ω phase peaks, the volume fraction of the ω phase seems to be higher in the ECAP material than in non-deformed and HPT ones (the most noteworthy peaks of the ω phase are marked with open arrows in Figure 4.8 at $d_{hkl} \approx 1.2 \text{ \AA}$ and 1.4 \AA). The increase may be caused by ECAP being carried out at the elevated temperature of $250 \text{ }^\circ\text{C}$ which is sufficient for irreversible formation of the diffusion stabilized ω_{iso} phase [19]. However, the actual increase of the volume fraction of the ω phase is uncertain due to large grains, preferred crystal orientation, small and broadened ω peaks.

4.1.4.2 High energy (synchrotron) X-ray diffraction measurement

The HPT-deformed Ti15Mo alloy was also examined using HEXRD in order to provide a more accurate measurement and to determine the volume fraction of the individual phases. In contrast to standard XRD, HEXRD penetrates deeper into the material and thus provides better statistics and better resolution of small peaks of the ω phase.

The HEXRD pattern of the HPT material is presented in Figure 4.9. The graph shows both the measured and the fitted intensities. The difference curve between the fitted and measured intensity is shown in the figure as well. The results indicate that the HPT-deformed alloy is a two-phase material with volume fractions of the β and ω phase of 72% and 28%, respectively (the error of the volume fractions is approximately $\pm 4 \%$).

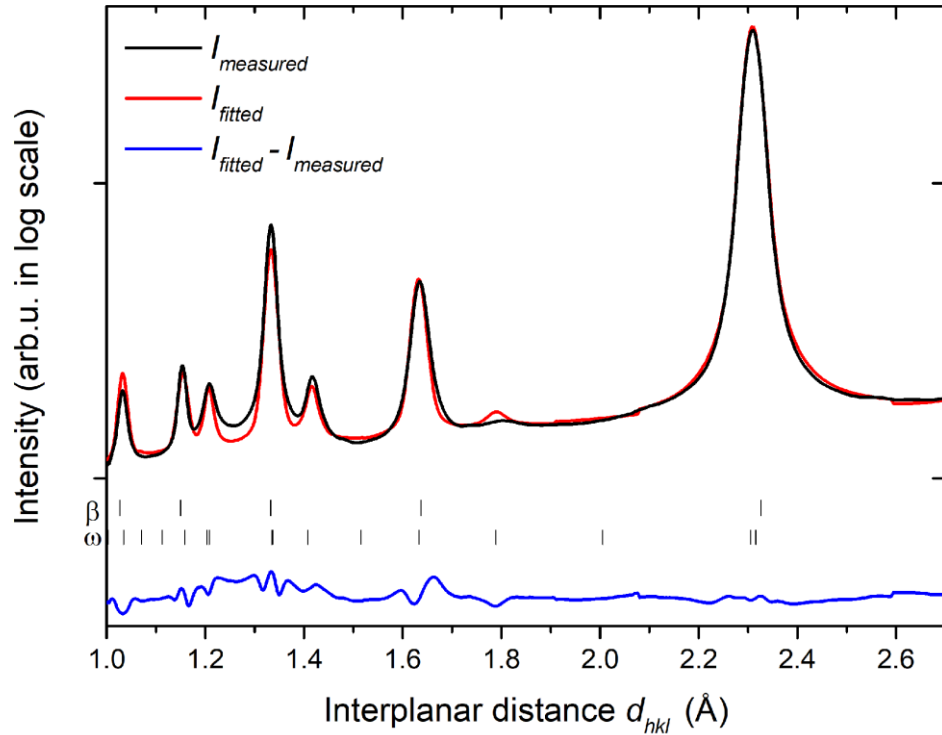


Figure 4.9 HEXRD pattern of the Ti15Mo alloy after HPT processing. The intensity is shown in a logarithmic scale. Measured and fitted data are displayed by black and red curves, respectively. The difference curve is shown in blue color.

4.1.5 Microhardness of the initial materials

The microhardness of the non-deformed, HPT ($N = 1$ turn), and ECAP ($N = 2$ passes) materials was measured using Vickers method. The results are summarized in Table 4.2.

The microhardness of the non-deformed sample is ~ 278 HV and significantly increases after HPT deformation up to values of ~ 400 HV. The increase of the microhardness in the ECAP specimen is slightly lower, it reaches the value ~ 378 HV. The increase of the microhardness of the deformed samples can be attributed to the grain refinement and also to the increased amount of the ω phase.

Table 4.2 Vickers microhardness of the Ti15Mo alloy in non-deformed and both deformed (HPT and ECAP) conditions.

	Vickers microhardness (HV)
Non-deformed	278 ± 14
HPT ($N = 1$ turn)	400 ± 5
ECAP($N = 2$ passes)	378 ± 11

4.2 Effect of deformed microstructure on α phase precipitation

The second subchapter is dedicated to the ageing response of the microstructure, defects, phase composition and microhardness of the non-deformed, HPT ($N = 1$ turn) and ECAP ($N = 2$ passes) material. Each material was investigated after ageing treatment at temperatures 400 °C and 500 °C for 1, 4 and 16 hours.

4.2.1 Microstructure evolution with ageing

SEM–BSE micrographs in Figure 4.10 show the microstructures of the non-deformed Ti15Mo alloy after ageing at 400 °C and 500 °C for 1 – 16 h. The individual microstructures consist of a CG β matrix and, with increasing ageing temperature and time, α phase precipitates which appear darker in BSE images due to their lower Mo content. After ageing at 400 °C for 1 and 4 hours, no α phase can be observed. After a longer ageing time (400 °C/16 h), nanometer scale, darker precipitates are visible on the SEM–BSE image (note the higher magnification of this particular image – small precipitates could not be observed in low magnification micrographs). On the other hand, ageing at 500 °C resulted in precipitation of thick and continuous α phase along grain boundaries already after ageing for 1 hour as indicated by white arrows in Figure 4.10 (hereafter referred to as grain boundary α or GB α). In the vicinity of the β grain boundary, lamellar α phase particles precipitated. Small and rather ellipsoidal particles, which were observed already after ageing 400 °C/16 h, are clearly visible in β grains interior. These particles, which are more pronounced after ageing 500 °C/16 h are ω particles as it will be shown using TEM in Section 4.2.1.1.

The microstructures of the HPT and ECAP samples after ageing are displayed in Figure 4.11 and Figure 4.12, respectively. Significant differences in the α phase precipitation between the non-deformed and deformed (HPT and ECAP) conditions can be observed already after ageing at 400 °C/1 h. While in the non-deformed material there is no evidence of α phase particles, small and equiaxed α phase particles precipitated in HPT and ECAP samples. In the ECAP material, the tiny and equiaxed α particles are arranged in chains (highlighted by circles in Figure 4.12). These chains seem to be shear bands with a higher concentration of lattice defects which were observed using TEM (see Figure 4.6).

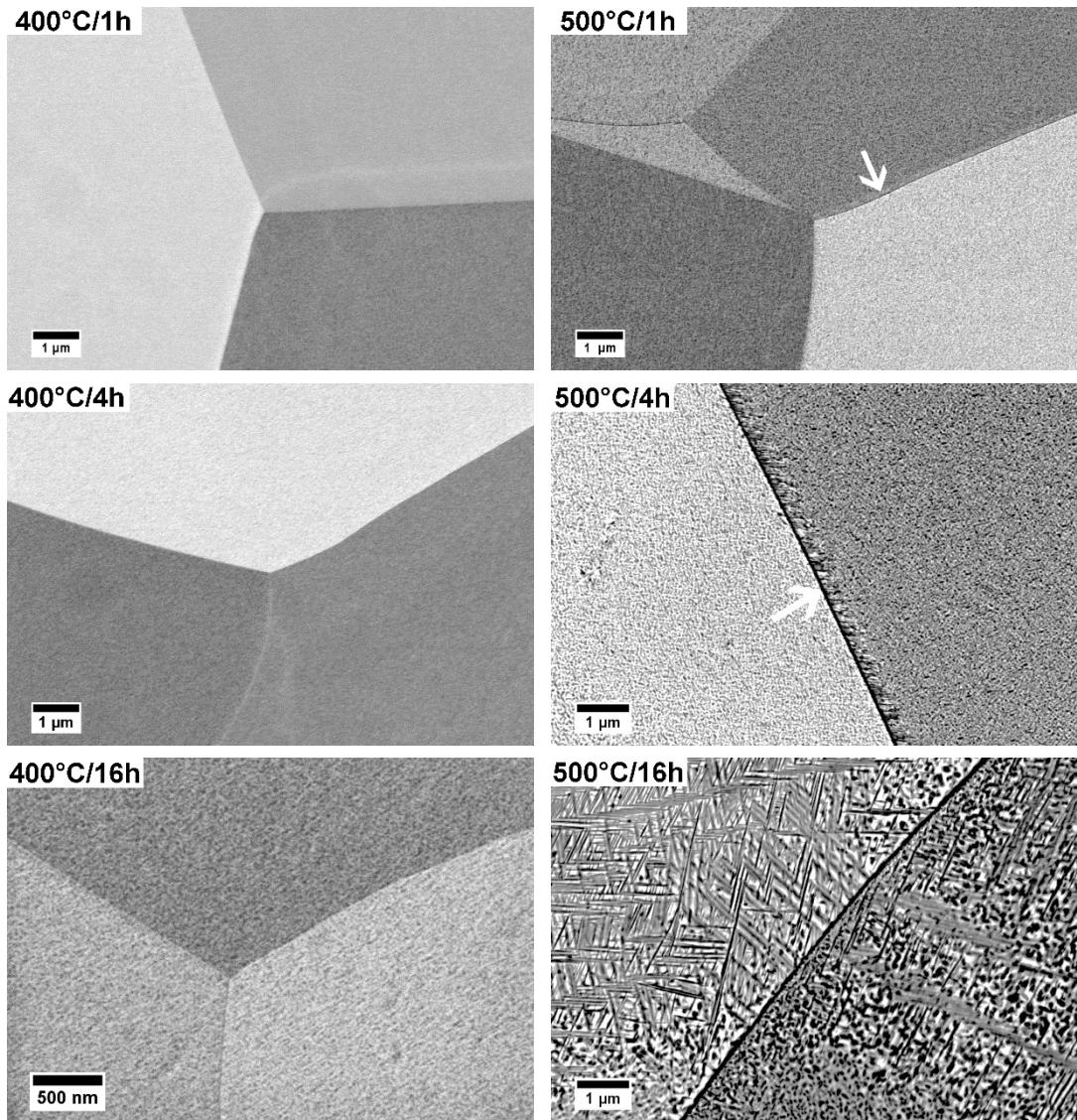


Figure 4.10 SEM–BSE images of the non-deformed Ti15Mo alloy after ageing at 400 °C and 500 °C for 1 – 16 hours. Note the higher magnification of the image after ageing 400 °C/16 h. White arrows indicate the grain boundary α phase.

After a longer ageing at 400 °C for 4 h and 16 h, the volume fraction of the α phase increased and α precipitates simultaneously coarsened in both deformed materials. In the HPT material, the precipitation is significantly inhomogeneous despite the relatively homogeneous deformation. On the other hand, in the material after ECAP deformation the formation of α particles is still limited to shear bands (as pointed out by an arrow in the SEM–BSE image after ageing 400 °C/4 h in Figure 4.12).

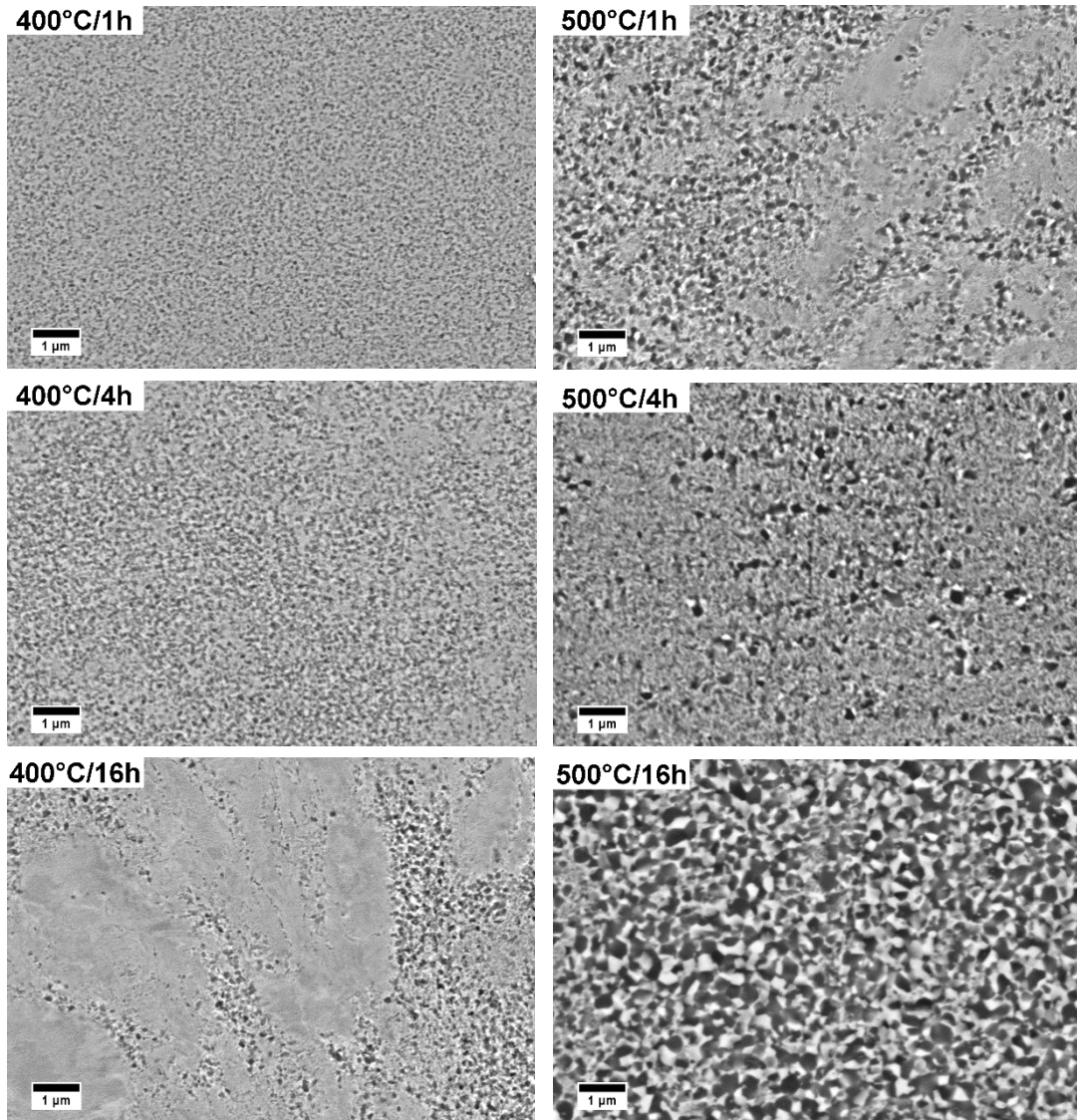


Figure 4.11 SEM–BSE images of the HPT-processed Ti15Mo alloy after ageing at 400 °C and 500 °C for 1 – 16 hours.

Upon ageing at 500 °C, the HPT material contains only equiaxed α phase particles, that are, however, rather polygonal and sharp edged. Areas with a lower amount of α phase are observed after ageing 500 °C/1 h and can be also noticed in 500 °C/4 h image as areas with more refined precipitates. After ageing of the HPT material at 500 °C/16 h, α phase particles become significantly coarser when compared to the non-deformed material.

ECAP material contains a higher amount of the α phase in shear bands compared to areas consisting only coarse-grained β phase. More pronounced coarsening of α phase particles is observed after ageing at 500 °C. Ageing of the ECAP material at 500 °C for 16 hours resulted in an abnormal growth of the β grains, with the size exceeding 1 µm in shear bands. These β grains contain significantly coarser α lamellae

when compared to α particles in the non-deformed and aged material. Apart from these coarse precipitates, small α lamellae are observed in other regions.

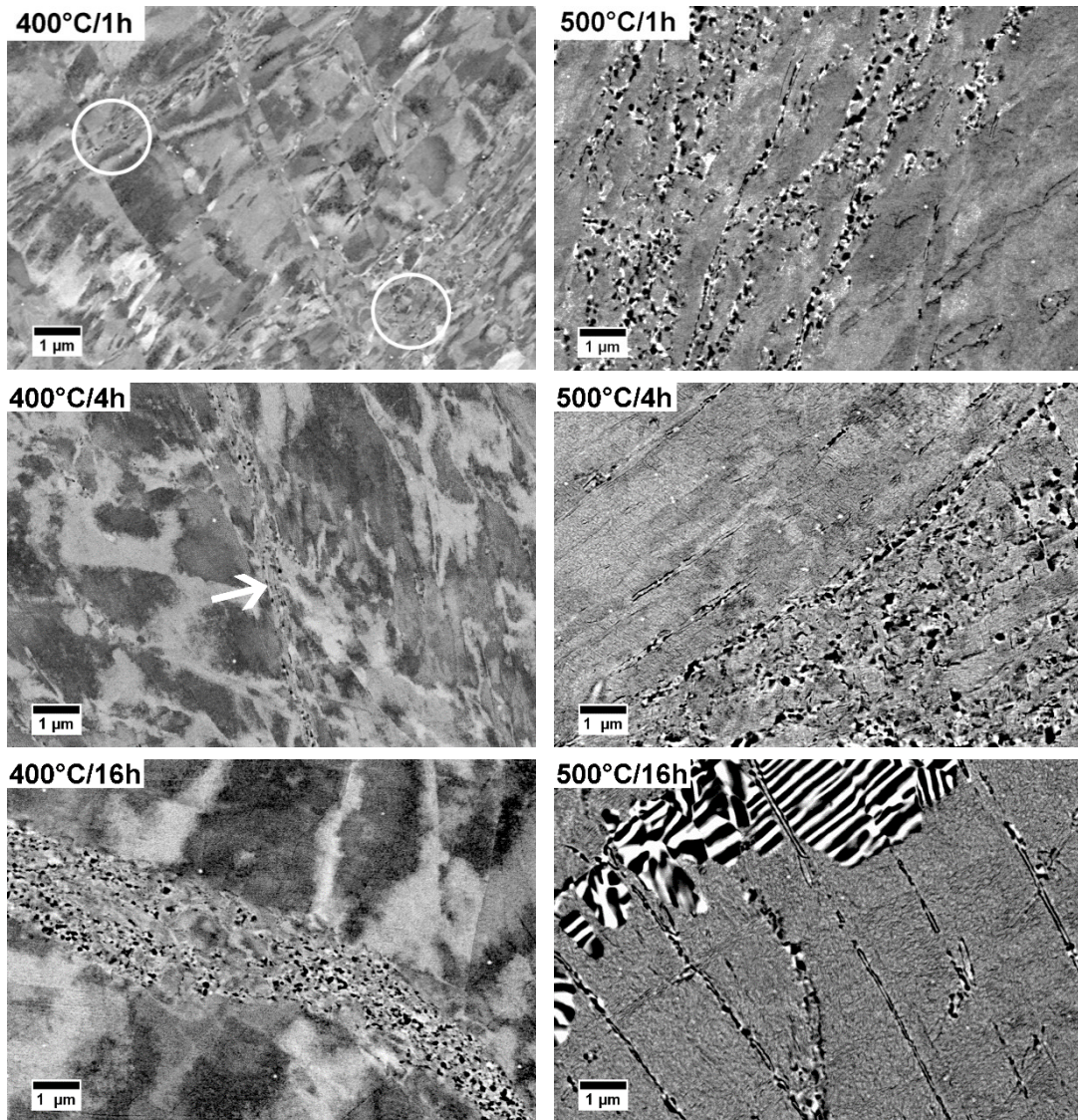


Figure 4.12 SEM–BSE images of the ECAP-processed Ti15Mo alloy after ageing at 400 °C and 500 °C for 1 – 16 hours. The white circles and the arrow denote α precipitates arranged in chains.

4.2.1.1 Detailed observation of the aged non-deformed microstructure by TEM

In the non-deformed specimen in the condition aged at 500 °C for 16 hours a microstructure consisting of coarse β grains with GB α , α lamellae, and nanometer-sized particles which are assumed to be ω particles can be observed (see Figure 4.10). In order to describe the microstructure more accurately, a detailed investigation was carried out using TEM. A site-specific thin sample (across grain boundary) for TEM observation was prepared using FIB as shown in Figure 4.13 (note that the large black dots are polishing artifacts).

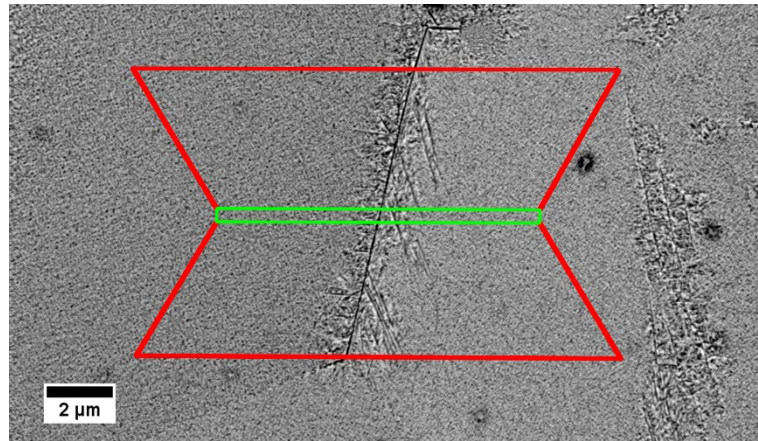


Figure 4.13 SEM–BSE micrograph and highlighted area of interest for TEM lamella preparation from the non-deformed sample after ageing 500 °C/16 h (black dots are polishing artifacts). The top of the lamella is shown in green. Material from the red area was removed by FIB during lamella preparation.

The TEM lamella containing coarse β grains, GB α , α lamellae, and small particles inside the β grain mentioned above was thoroughly characterized by TEM. Figure 4.14(a) shows the SAED pattern of the β matrix in the $[110]_{\beta}$ zone axis, where diffraction spots belonging to β matrix and ω phase particles are clearly visible and distinguishable (the unindexed diffraction spots within one unit cell are caused by double diffraction). The TEM BF image in Figure 4.14(b) shows an interior of the β grain with ellipsoidal ω phase particles exceeding the size of 100 nm along the longer axis. All ω particles in diffraction contrast appearing dark in the TEM BF image in Figure 4.14(a) are elongated in one of a possible four $[111]_{\beta}$ directions and belong to a single ω family. ω particles in different orientations (different families of ω particles) appear bright in the BF image, since they are not in diffraction contrast. The corresponding TEM DF image from the reflection of the ω phase, highlighted by a red arrow in Figure 4.14(a), is shown in Figure 4.14(c).

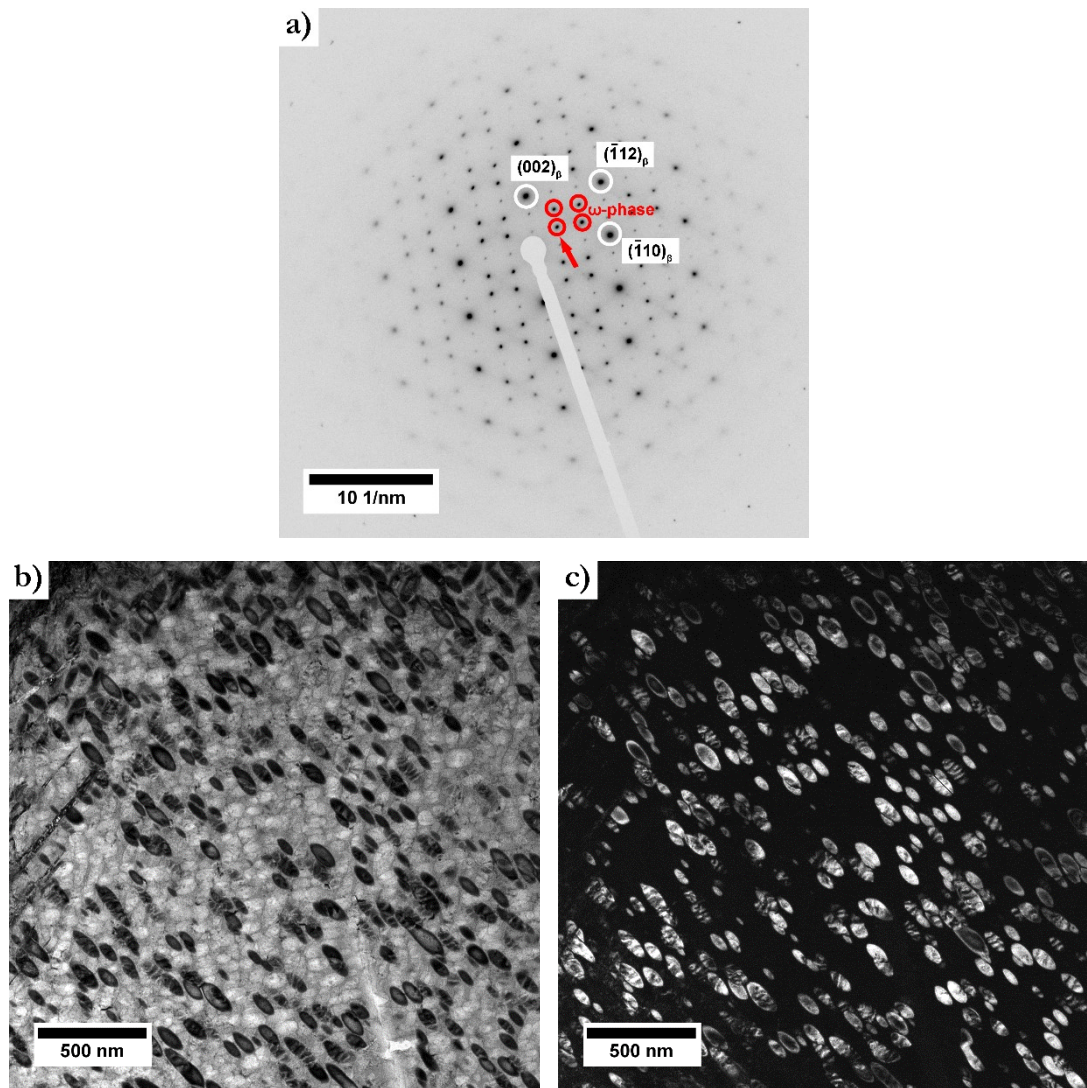


Figure 4.14 (a) SAED pattern from one grain of the TEM lamella containing β and ω phase, highlighted by white and red circles, respectively. (b) TEM BF image of the grain with clearly visible ω particles from one family, and (c) corresponding TEM DF image from one reflection of the ω phase highlighted by red arrow in Figure 4.14 (a).

α lamellae in the vicinity of the β grain boundary were also observed in detail. Figure 4.15(a) shows the SAED pattern of an area of the β matrix containing α lamellae. The unit cell of the β phase and α phase are indexed by red and blue color, respectively. Unindexed diffraction spots within one unit cell are caused by double diffraction. One reflection from the α phase was chosen to form a TEM DF image of α lamellae – see Figure 4.15(b). The thickness of lamellae does not exceed 100 nm.

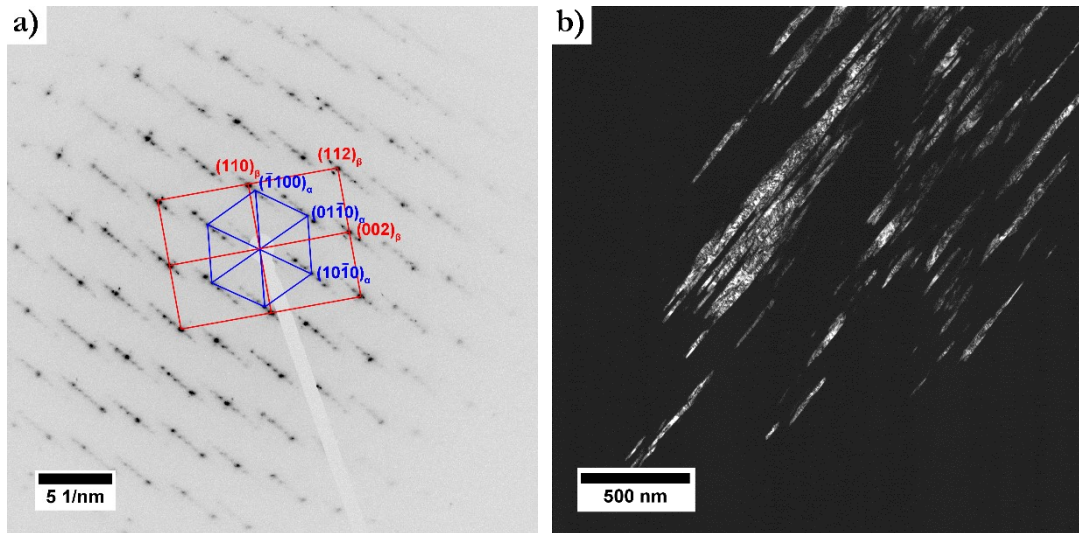


Figure 4.15 (a) SAED pattern from the α lamellae near the grain boundary (the unit cell of the β phase and α phase are indexed by red and blue color, respectively, and unindexed diffraction spots within one unit cell are caused by double diffraction), and (b) TEM DF image from one reflection of the α phase.

4.2.1.2 Detailed observation of the aged ECAP material using TKD

The Ti15Mo alloy after ECAP deformation followed by ageing at 400 °C for 16 hours was investigated in detail in order to obtain information about the morphology of α phase precipitates in shear bands. Site-specific thin lamella preparation was carried out using FIB as it is schematically displayed in Figure 4.16. A thin lamella transparent for electrons was cut across a fine-grained strip containing α phase particles. An investigation of the lamella was carried out using TEM and TKD.

TEM BF image in Figure 4.17 shows a shear band (denoted with letter A), the intermediate area between β matrix and the SB (B) and a large β grain (C). In the shear band (A), a high density of dislocations and an UFG structure is observed. In the transition area between the SB and the β grain (B), elongated particles are visible which appear bright in diffraction contrast (indicated by red arrows). In the lower left side of Figure 4.17 (area C), the β grain contains nanosized particles which appear dark in the image. Each part (A, B and C) of the material was investigated separately and the results are described in detail below.

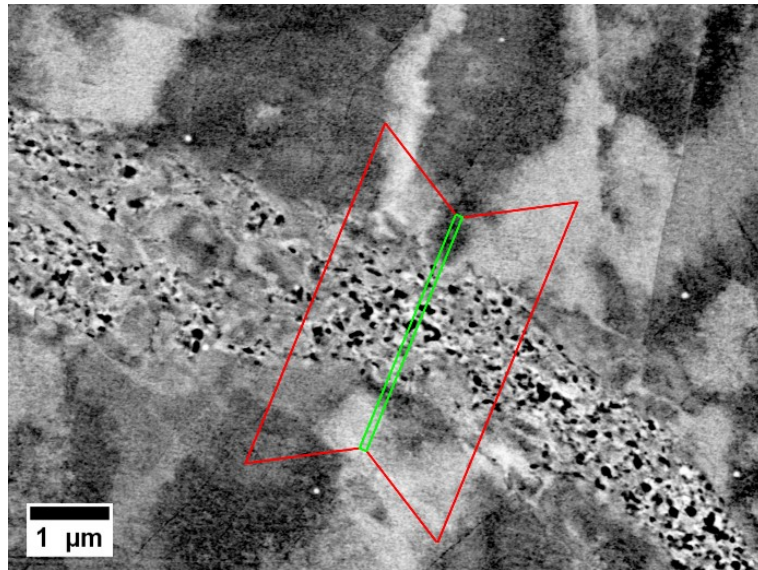


Figure 4.16 SEM–BSE micrograph and highlighted area of interest for TEM lamella preparation from ECAP sample aged at 400 °C for 16 hours. The top of the lamella is shown in green. Material from the red area was removed by FIB during lamella preparation.

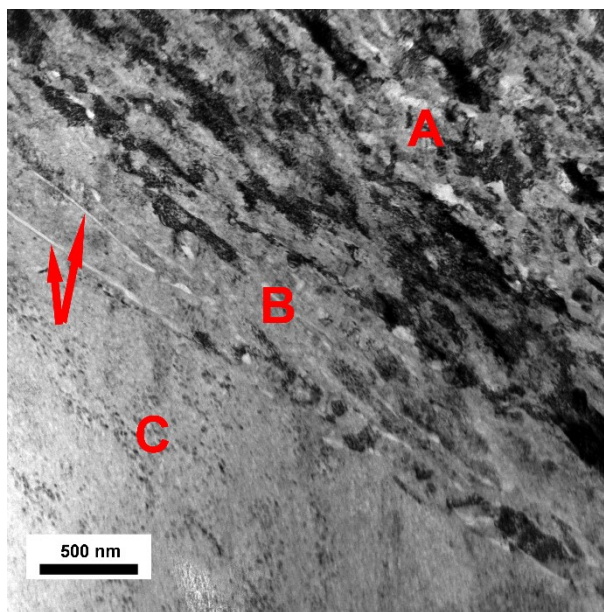


Figure 4.17 TEM BF image containing the interface of SB with β matrix. The letters A, B, and C represent the areas of interest for further investigation. Red arrows indicate elongated particles in the intermediate area (B).

The shear band (denoted with letter A in Figure 4.17) is displayed with a higher magnification in Figure 4.18(a) and consists of $\beta+\omega+\alpha$ phases as proven by SAED pattern in Figure 4.18(b). The microstructure consists of ultra-fine β and α grains with the size of 100 – 200 nm. The particles of the ω phase cannot be distinguished in Figure 4.18(a) due to their small size.

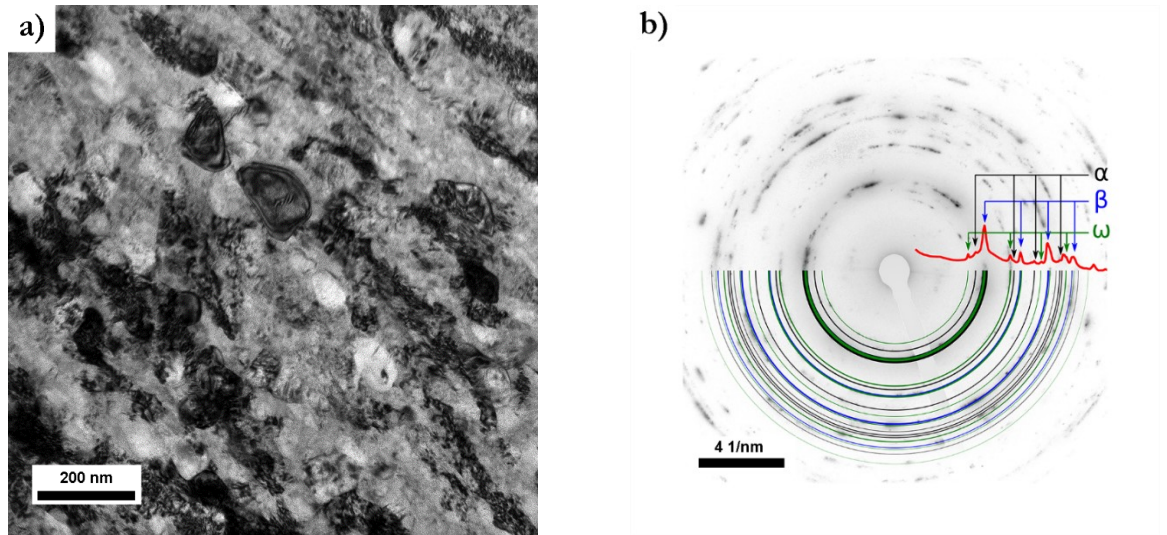


Figure 4.18 (a) TEM BF image of the UFG structure consisting of $\beta+\omega+\alpha$ phases and (b) corresponding SAED pattern.

Figure 4.19(a) illustrates an elongated and highly deformed particle that precipitated along the β/β grain boundary in the transition region between the shear band and the CG β matrix (denoted by letter B in Figure 4.17). The particles was identified as α phase due to its hcp structure, see the inset SAED pattern in $[2-1-10]_{\alpha}$ zone axis in Figure 4.19(a). Figure 4.19(b) shows a TEM DF image of the α phase particle.

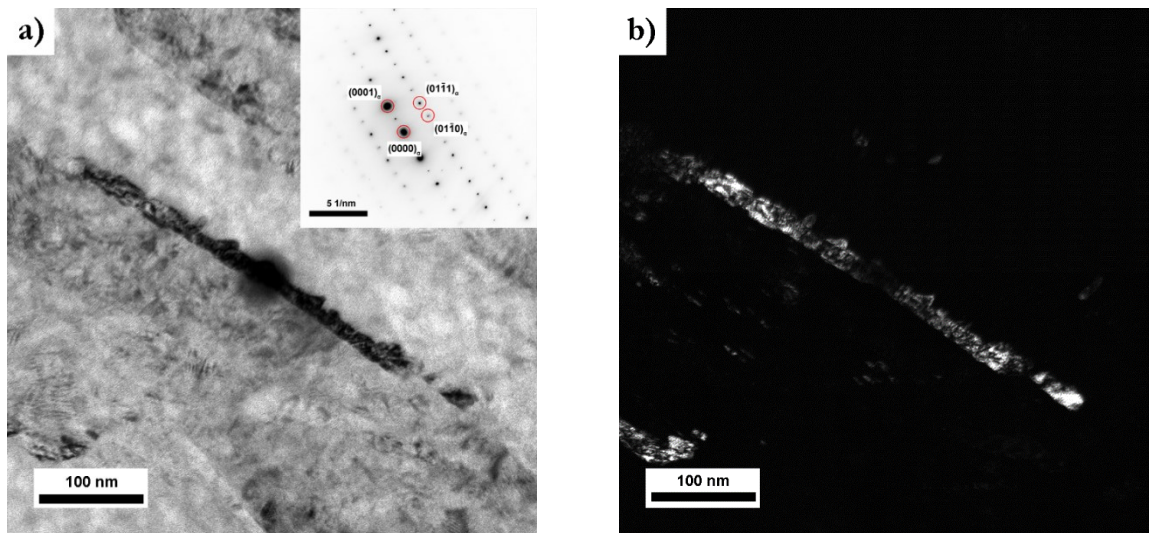


Figure 4.19 (a) TEM BF image and (b) TEM DF image near the interface of the CG β matrix with the shear band (area B in the Figure 4.17) with corresponding SAED pattern of the elongated α phase particle in $[2-1-10]_{\alpha}$ zone axis.

Figure 4.20(a) represents the SAED pattern from the interior of the β grain in $[110]_{\beta}$ zone axis (denoted by letter C in Figure 4.17). β spots can be clearly identified

in the SAED pattern along with the low intensity reflections which are associated with the presence of the tiny ω phase particles [19]. These nanosized particles of the ω phase are well visible in TEM DF image obtained using one reflection of the ω phase (Figure 4.20(b)).

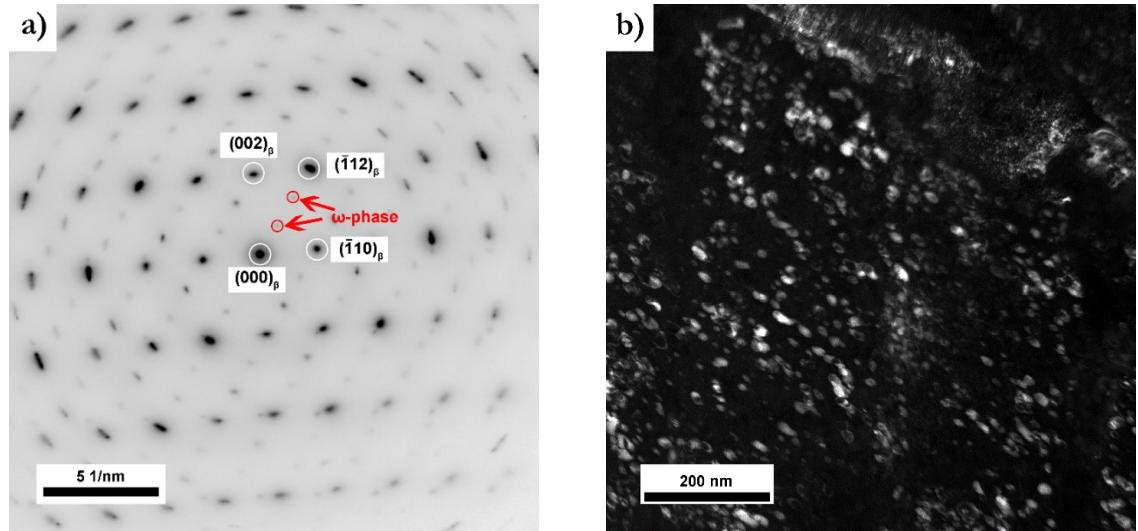


Figure 4.20 (a) SAED pattern of the β matrix (zone C in the Figure 4.17) in $[110]_{\beta}$ zone axis and (b) corresponding TEM DF image from ω phase reflection.

The area of the shear band and the coarse β grain (areas corresponding to letters A and C in Figure 4.17) were also studied by TKD. Figure 4.21(a) shows an SEM-BSE micrograph of the analyzed area from the shear band. Darker areas can be associated with Mo depleted α phase particles due to the chemical contrast. Figure 4.21(b) shows the phase map, while Figure 4.21(c) and (d) show the IPF maps from the β phase and α phase, respectively. These images were obtained by the TKD method. The microstructure within the observed $\alpha+\beta$ layer is UFG composed of refined β phase matrix and equiaxed α phase particles. Although the TEM analysis proved the phase composition of $\beta+\alpha+\omega$ (Figure 4.18 (b)), ω phase cannot be identified by TKD due to its nanometer size and ambiguous indexation of Kikuchi patterns of ω and α phases (both phases are hexagonal) [139].

Note that the theoretical interaction depth for the generation of backscattered electrons (~ 200 nm) is larger than the thickness of the lamella, which is approximately 150 nm. Thus, the observed chemical contrast (Figure 4.21(a)) is averaged over the thickness of the lamella, while small α particles may not span through the whole thickness. On the other hand, the signal from TKD arises only from the (bottom)

surface layer with the thickness of approximately 50 – 100 nm [12, 13]. Therefore, the match of the BSE micrograph and IPF maps is not perfect.

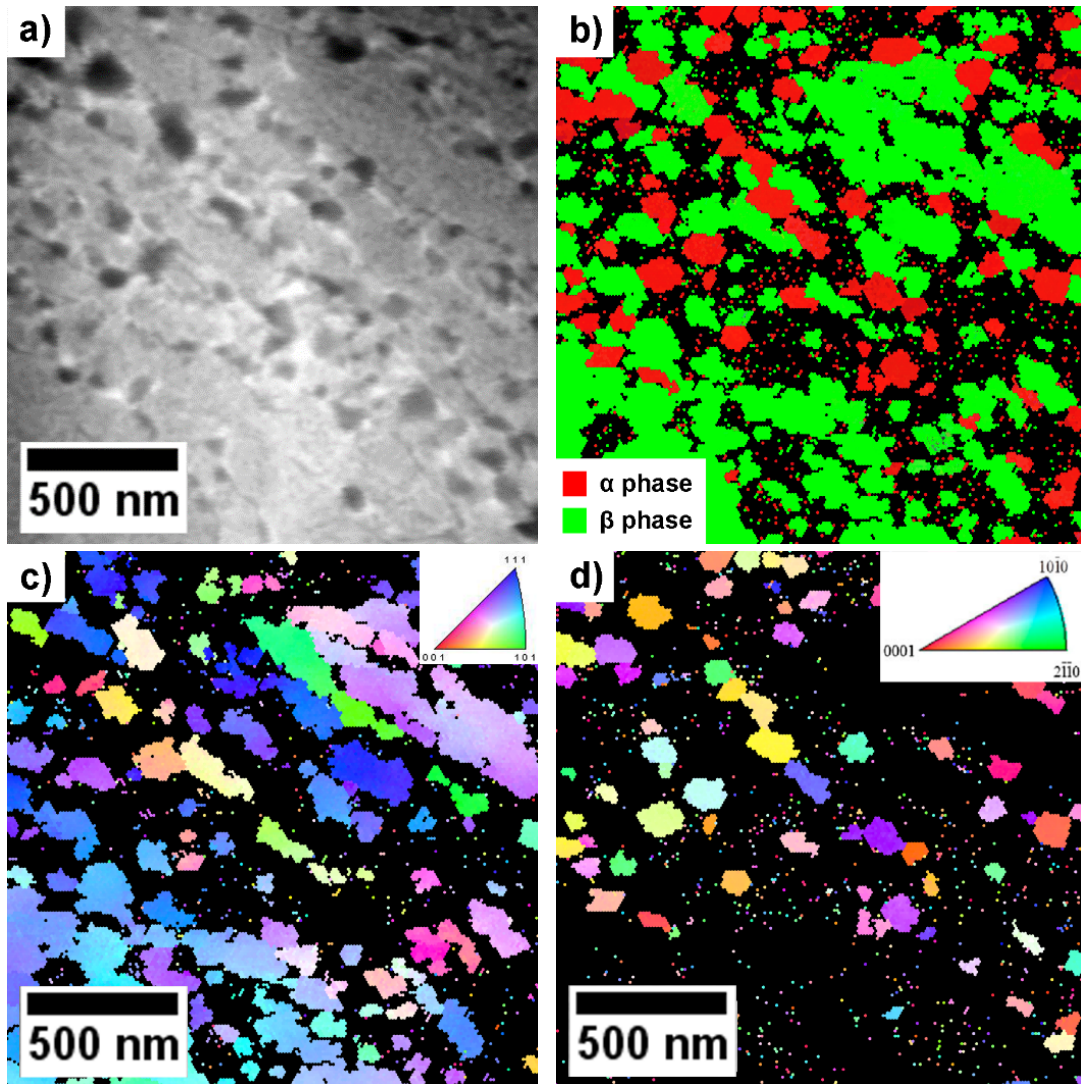


Figure 4.21 (a) SEM–BSE micrograph, (b) phase map of α and β phases (c) IPF map from the β phase and (c) IPF map from the α phase in the shear band of the ECAP sample aged at 400 °C for 16 hours.

The IPF map obtained from a coarse β grain using TKD outside the refined layer is shown in Figure 4.22. The coarse grain was determined as a pure β phase by TKD. However, the material contains also ω phase particles (proved above by TEM) which cannot be resolved by TKD. The observed β grain is strongly deformed, the crystal lattice is rotated and contains low angle-grain boundaries. The degree of the deformation within one β grain was characterized by the change of orientation along the red line shown in Figure 4.22(a) from its origin marked as O. Figure 4.22(b) shows the dependence of the misorientation on the distance from the origin O in Fig. 4.22(a) (point to origin misorientation). The misorientation increases to 25° within 2 μm

distance which indicates a highly deformed microstructure, without any high-angle grain boundaries.

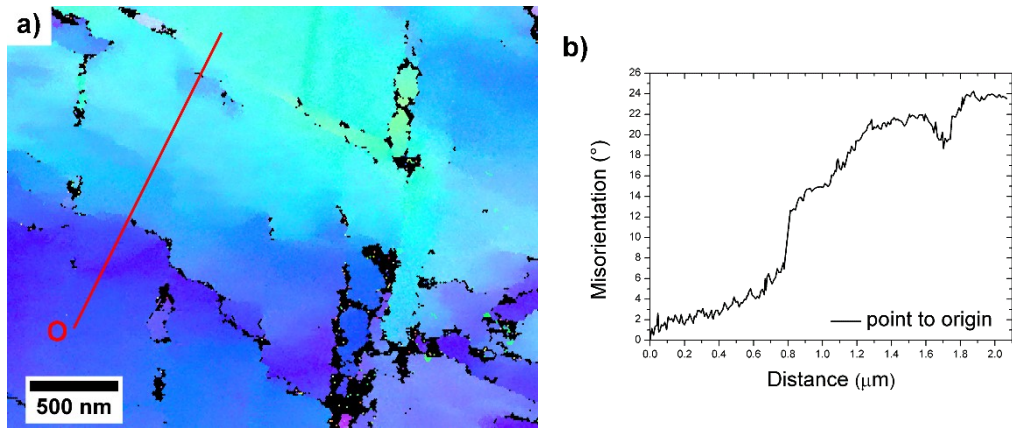


Figure 4.22 (a) IPF map from the β matrix with a highlighted line for misorientation measurement with origin O, (b) the dependence of the misorientation on the distance from the origin (O) measured along the red line in Figure 4.22(a).

4.2.2 Evolution of the phase composition with ageing

The evolution of individual phases in the non-deformed and deformed material after ageing was studied using standard XRD. For a more accurate determination of the evolution of phases, HEXRD measurement was done on selected HPT samples. For a better comparison of XRD patterns obtained using these two methods, the XRD pattern is not displayed as function of 2θ angle which depends on wavelength, but as a function of the interplanar distance d_{hkl} . The intensity is shown in a logarithmic scale.

4.2.2.1 X-ray diffraction measurement

The evolution of phases in the non-deformed, HPT and ECAP samples is shown in XRD patterns in Figure 4.23, 4.24 and 4.25, respectively. For clarity, only a fitted curves are displayed. The most important peaks, where the evolution of emerging phases is the most apparent, are marked with arrows – filled and open arrows for α and ω phase, respectively. A quantitative determination of phase content is not possible since the non-deformed materials contain large grains with the size of hundreds of micrometres and the statistics for powder diffraction evaluation is not sufficient. ECAP deformed alloy contains also large grains. Although the HPT material is ultra-fine grained, it is significantly textured. Nevertheless, several qualitative comparisons can be made.

As it was described in Section 4.1.4, the non-deformed material (without ageing) consists of a mixture of $\beta + \omega_{ath}$ phase. However, only a broad peak of the ω phase at

the interplanar distance $d_{hkl} \approx 1.2 \text{ \AA}$ is visible, see Figure 4.23. Ageing of non-deformed material at $400 \text{ }^\circ\text{C}/1 \text{ h}$ (red curve in Figure 4.23) results in an increase of the intensity and narrowing of ω phase (open arrows). Small peaks from the α phase are also visible (filled black arrows). XRD patterns of the non-deformed material aged at $400 \text{ }^\circ\text{C}$ for 1, 4 and 16 hours are very similar. After ageing at $500 \text{ }^\circ\text{C}/1 \text{ h}$, the α phase is clearly present (filled arrows in Figure 4.23) and its volume fraction increases with increasing ageing time (4 – 16 hours), which is consistent with SEM observations. Even after ageing at $500 \text{ }^\circ\text{C}$ for 16 hours, ω phase is still present which supports SEM and TEM observations described in detail in the previous text.

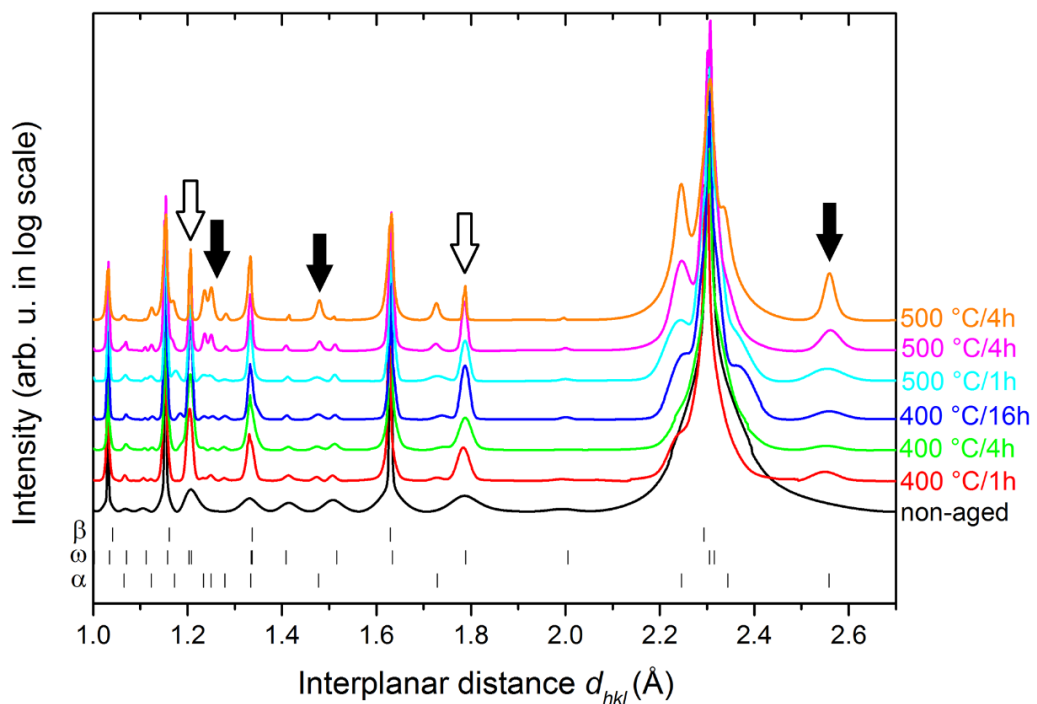


Figure 4.23 XRD patterns of aged conditions of the non-deformed Ti15Mo alloy: non-deformed without ageing (black curve) and aged under different conditions (colored curves) are displayed. The patterns are vertically shifted for clarity. The most important peaks are marked by filled arrows for α phase and open arrows for ω phase.

XRD patterns in Figure 4.24 show the phase evolution in the HPT material during subsequent ageing. As it was described above (Section 4.1.4.2) the alloy after deformation by HPT contains a significant fraction of the ω phase. In contrast to the non-deformed material, a significant increase of the volume fraction of the α phase is apparent even after aging at $400 \text{ }^\circ\text{C}/1\text{h}$ (red curve in Figure 4.24, visible especially at $d_{hkl} \approx 2.58 \text{ \AA}$). After longer ageing at $400 \text{ }^\circ\text{C}$ and also at $500 \text{ }^\circ\text{C}$, the α phase volume fraction continuously increases. On the other hand, no evident peak of the ω phase is observable in individual ageing conditions. However, the apparent absence of the

ω phase in aged HPT material may be caused by the coincidence of the ω and β peaks (e.g. at interplanar distances $d_{hkl} = 1.15 \text{ \AA}$, 1.33 \AA , or 2.3 \AA), by insufficient statistics of the measured data, or by strong texture. More precise results can be obtained using HEXRD; an example of the HEXRD measurement on a selected sample (HPT-deformed and aged at $400 \text{ }^\circ\text{C}/1 \text{ h}$) is shown below in Section 4.2.2.2.

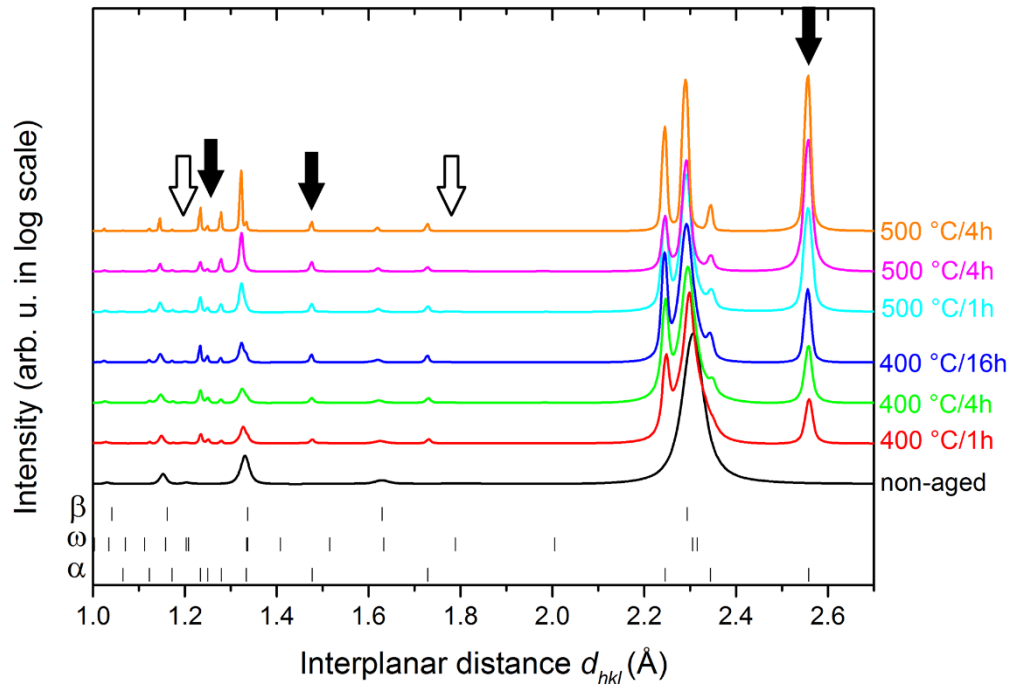


Figure 4.24 XRD patterns of aged conditions of the HPT-deformed Ti15Mo alloy: non-aged condition (black curve) and aged under different conditions (colored curves) are displayed. The patterns are vertically shifted for clarity. The most important peaks are marked by filled arrows for α phase and open arrows for ω phase.

In the ECAP material, the volume fraction of the ω phase increases after ageing at $400 \text{ }^\circ\text{C}/1 \text{ h}$, similarly to the non-deformed material (red curve in Figure 4.25, open arrows). However, the increase of the α phase content is not so evident as in the HPT-deformed specimen. After ageing at $400 \text{ }^\circ\text{C}$ for 16 hours (blue curve in Figure 4.25, filled arrows) the α phase is clearly present. The volume fraction of the α phase is significantly higher in samples aged at $500 \text{ }^\circ\text{C}$ and increases with increasing ageing time. An increased volume fraction of the α phase is accompanied by a decrease of the volume fraction of ω phase. After ageing at $500 \text{ }^\circ\text{C}$ for 16 hours, the ECAP material does not contain any ω phase, it is composed of a mixture of $\beta+\alpha$ phase.

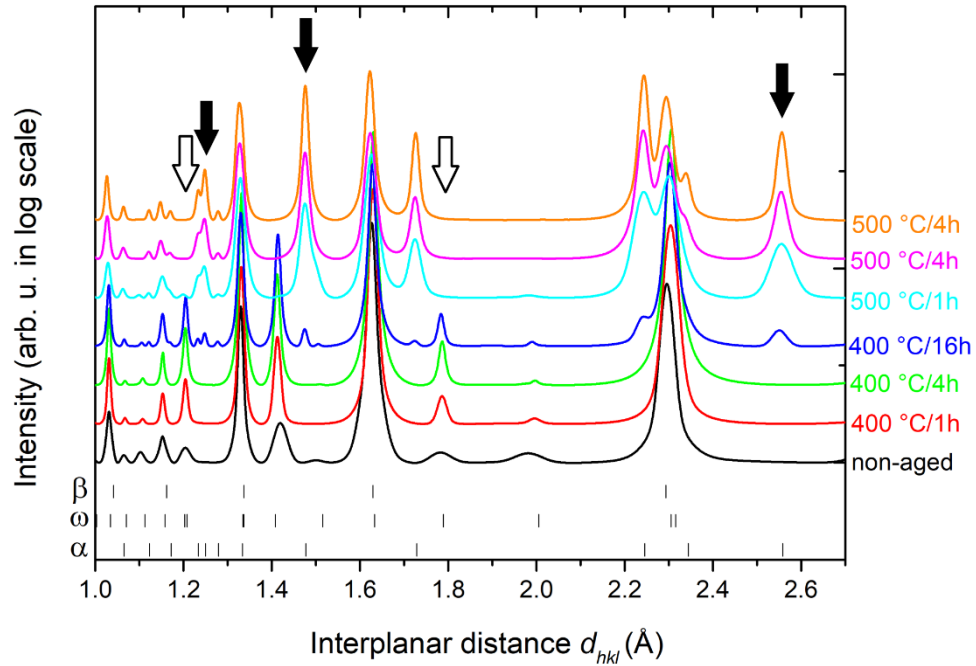


Figure 4.25 XRD patterns of aged conditions of the ECAP deformed Ti15Mo alloy: non-aged condition (black curve) and aged under different conditions (colored curves) are displayed. The patterns are vertically shifted for clarity. The most important peaks are marked by filled arrows for α phase and open arrows for ω phase.

4.2.2.2 High energy (synchrotron) X-ray diffraction measurement

The specimen of the HPT material after ageing at 400 °C/1h was examined using HEXRD in order to get more accurate results. The HEXRD pattern is shown in Figure 4.26. It presents both the measured and fitted intensity and also the difference between the fitted and measured data. In Figure 4.27 the comparison of the HEXRD patterns of the HPT specimens without ageing and after ageing 400 °C/1h is shown (the sample without ageing is described in detail in Section 4.1.4.2). The calculated volume fractions of individual phases in both specimens are summarized in Table 4.3 (the errors of determination of volume fractions are also shown). The HPT material contains a significant volume fraction of the ω phase (28 %). The volume fraction decreases to approximately 9 % after a short ageing time (1 hour). This is a consequence of the significantly increased volume fraction of the α phase, which reaches 23 % in this condition.

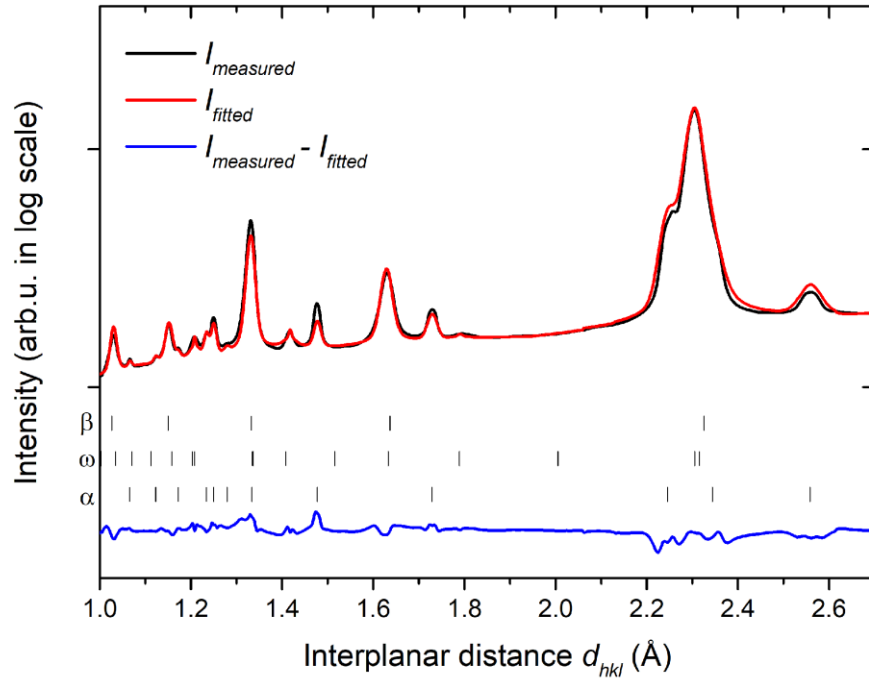


Figure 4.26 HEXRD pattern of the Ti15Mo HPT after ageing 400 °C/1 h. The intensity is shown in logarithmic scale. The measured and fitted data as well as the difference between them are displayed.

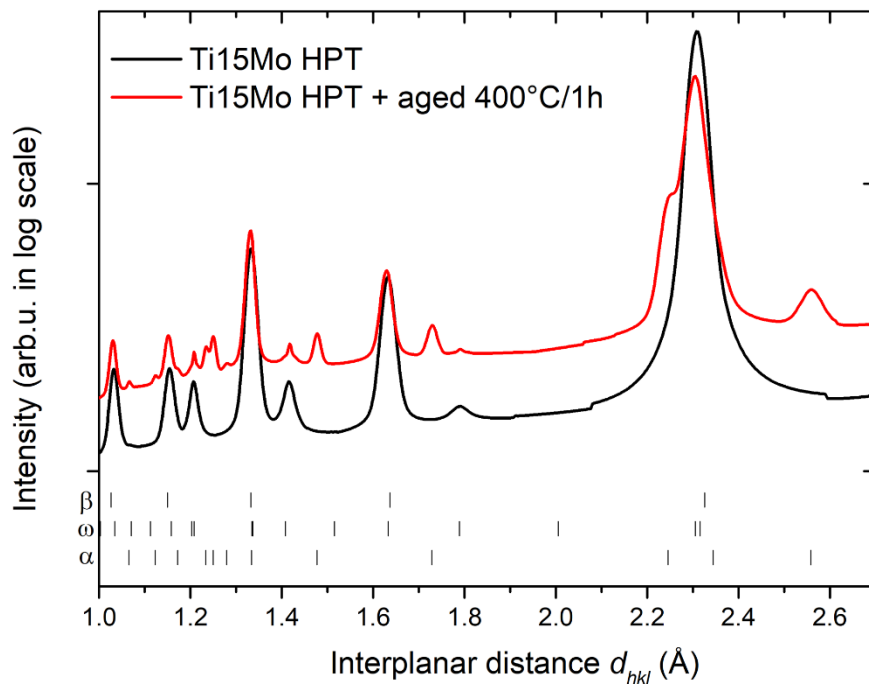


Figure 4.27 A comparison of HEXRD patterns of the Ti15Mo HPT samples without ageing and after ageing 400 °C/1 h. The intensity is shown in logarithmic scale. The patterns are vertically shifted for clarity. The measured and fitted data as well as the difference between them are displayed.

Table 4.3 Volume fraction of individual phases in Ti15Mo HPT determined from HEXRD. The errors of determination of volume fractions are also shown.

Material	Volume fraction of the β phase	Volume fraction of the ω phase	Volume fraction of the α phase
Ti15Mo HPT	72% \pm 5%	28% \pm 5%	-
Ti15Mo HPT + ageing 400 °C/1 h	67% \pm 5%	9% \pm 3%	23% \pm 4%

4.2.3 Defect structure and its evolution with ageing

The evolution of defects in the HPT-deformed Ti15Mo alloy after ageing was studied using PAS. The mean positron lifetimes (LT) as a function of the ageing time for both ageing temperatures of 400 °C and 500 °C are shown in Figure 4.28. The positron source was placed 7 mm from the center of the sample corresponding to the periphery of the disk (the specimen's radius is 10 mm). The mean positron LT is a robust parameter which is suitable for determination of defect evolution during ageing. After ageing at 400 °C for 1 and 4 hours the mean positron LT remained the same within experimental error. However, after ageing at 400 °C for 16 hours it significantly decreases indicating a recovery of lattice defects. Ageing at 500 °C does not result in a decrease of the mean positron LT as it may be expected due to assumed recovery of defects. On the contrary, ageing at 500 °C/16 h results in a slight increase which may be attributed to the formation of new lattice defects such as incoherent α/β interfaces – so-called misfit defects.

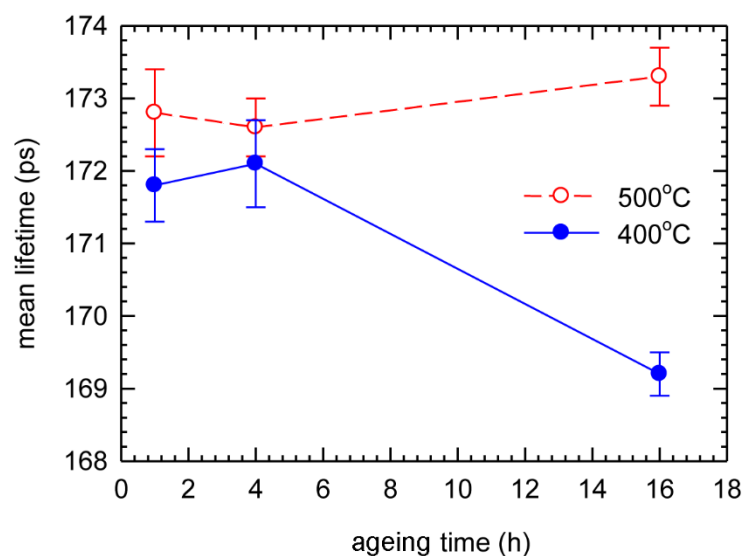


Figure 4.28 The mean positron lifetime in the HPT sample as a function of ageing time for ageing temperatures of 400 °C and 500 °C

The decomposition of the lifetime spectra into individual components is shown in Figure 4.29. The spectra contain 2 components: the component with a shorter lifetime τ_1 represents a contribution of free positrons, while the other one with longer lifetime $\tau_2 \approx 170$ ps may originate from positrons trapped at dislocations.

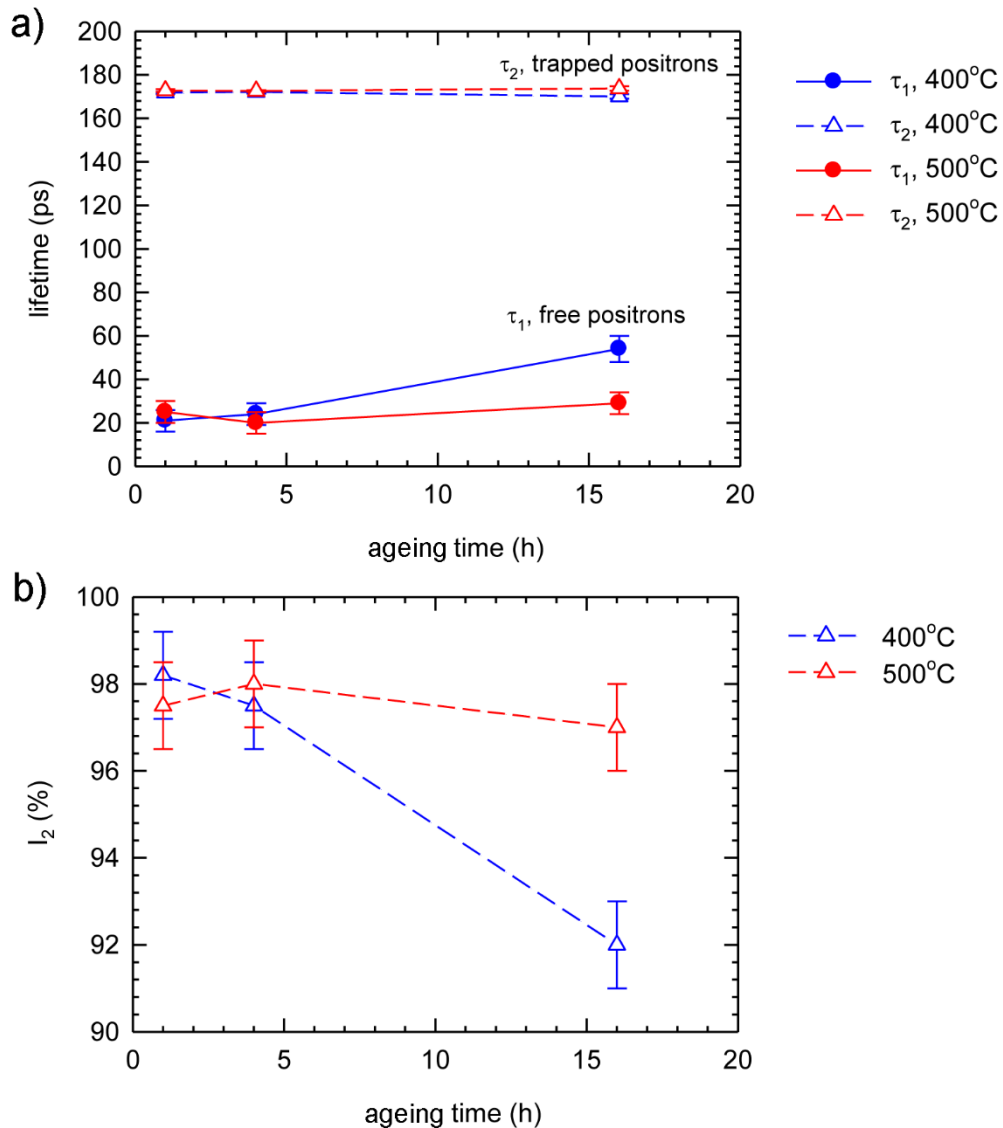


Figure 4.29 Dependence of the (a) lifetime of positrons trapped at defects and of positrons annihilating as free positrons, and (b) intensity I_2 of positrons trapped at defects in the HPT sample on the ageing time for ageing temperatures of 400 °C and 500 °C.

However, during ageing of the material, precipitation of the α phase introduces new positron traps into the material. These are misfit defects at the incoherent α/β interface where the LT of positrons can be comparable to the LT of positrons trapped at dislocations [141]. The distinction of these components in the LT spectra is not possible and the density of misfit defects and/or dislocations cannot be unambiguously determined. The dependence of the positron LT and the intensity I_2 of

positrons trapped at defects on the ageing time for both ageing temperatures are shown in Figure 4.29(a) and (b), respectively. The lifetime τ_2 is approximately constant for both ageing temperatures of 400 °C and 500 °C confirming that the nature of defects remains unchanged. The intensity component corresponding to positrons trapped at defects I_2 has a dominant intensity of 98 % (it means that 98 % of positrons is trapped at defects and do not annihilate as free positron). This intensity gradually decreases with increasing ageing time at 400 °C due to the recovery of defects. However, the intensity I_2 for the ageing temperature of 500 °C remains constant within experimental error despite recovery of defects introduced by deformation may occur. This can be caused by increasing fraction of incoherent α/β interfaces which also act as traps for positrons (see SEM-BSE images in Figure 4.11).

4.2.4 Evolution of the microhardness with ageing

The dependence of the Vickers microhardness on different ageing conditions of the non-deformed and deformed (HPT and ECAP) samples is shown in Figure 4.30.

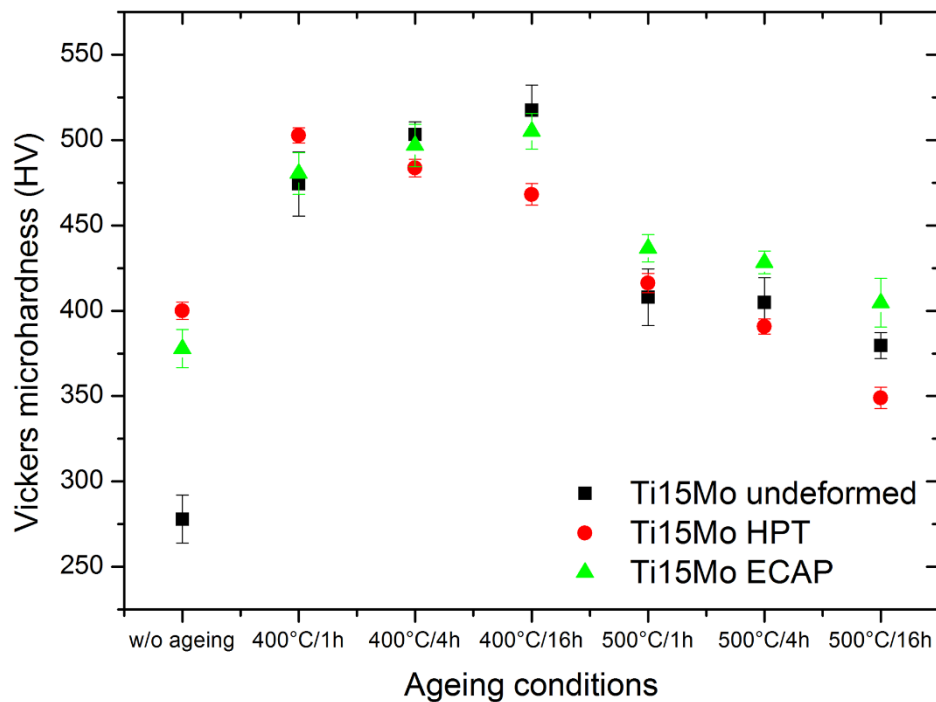


Figure 4.30 Evolution of the Vickers microhardness with ageing for non-deformed and deformed (HPT and ECAP) specimens

Ageing of all types of materials at 400 °C results in an abrupt increase of microhardness. Microhardness of both the non-deformed and ECAP specimen increases with increasing time of ageing at 400 °C. In contrast, the microhardness of the HPT sample is the highest (500 HV) after ageing at 400 °C/1 h and continuously

decreases with increasing ageing time. Ageing at the temperature of 500 °C results in lower microhardness values than after thermal treatment at 400 °C. The HPT sample after ageing at 500 °C/16 hours exhibits lower microhardness than the non-aged HPT specimen.

4.3 In-situ observations of phase transformations

Phase transformations were studied also in-situ during heating by various advanced experimental methods. The non-deformed and HPT materials were investigated using HEXRD, electrical resistivity and TEM. The measurements were carried out on HPT samples only due to their more deformed and UFG structure compared with the ECAP material.

4.3.1 In-situ high energy X-ray diffraction measurement

The non-deformed and HPT specimens were heated with the heating rate of 5 °C/min up to 800 °C. HEXRD patterns were simultaneously acquired every 15 seconds, the acquisition time being 1 s. Figure 4.31(a) and (b) show a two-dimensional plot of diffracted intensities for the non-deformed and HPT specimen, respectively. The intensity is in logarithmic scale and the horizontal and vertical axes correspond to the interplanar distance (d_{hkl}) and temperature, respectively. Furthermore, positions of β , ω , and α phase peaks are indicated in the lower part of each image.

The non-deformed sample contains $\beta + \omega_{ath}$ phase at room temperature (the most significant ω peak is at $d_{hkl} \approx 1.2 \text{ \AA}$) – this is consistent with the measurement of the phase composition by laboratory XRD described in Section 4.1.4.1 and also with measurements reported in [19]. The broadening of the ω peak at $d_{hkl} \approx 1.2 \text{ \AA}$ is caused by the small size of ω_{ath} particles. At a higher temperature, approximately 250 °C, the intensity of the ω peak decreases, which suggests the dissolution of the ω_{ath} phase. Just below 300 °C, the peak at $d_{hkl} \approx 1.2 \text{ \AA}$ starts to become stronger again and new peaks of the ω phase appear (for instance at $d_{hkl} \approx 1.4 \text{ \AA}$). With further heating these peaks become narrower and their intensity decreases, until at approximately 560 °C, they disappear completely. This behavior can be attributed to increasing volume fraction of ω_{iso} phase (increasing intensity of ω peaks), to the growth of the ω_{iso} phase particles (peaks narrowing) and to the dissolution of the ω_{iso} phase at 560 °C (disappearance of ω peaks) [37]. Heating above the temperature of 600 °C results in formation and growth of the α phase. α particles are present to the temperature of $\sim 770 \text{ °C}$, while above 770 °C they disappear and the material contains only the β phase (the

temperature of the β -transus of Ti15Mo alloy is ~ 774 °C [120]). Note that ω_{iso} phase during heating dissolved before the precipitation of the α phase started, i.e. the ω and α phase do not coexist in the non-deformed material upon continuous heating with the heating rate of 5 °C/min.

Figure 4.31(b) represents the evolution of the phase composition of the HPT sample upon heating. At room temperature, only a very weak and broad ω peak at $d_{hkl} \approx 1.2$ Å is present. In contrast, ex-situ HEXRD unambiguously confirmed the presence of the mixture of $\beta + \omega_{ath}$ phases as described in Section 4.1.4.2. Low intensity of ω peaks obtained by in-situ measurement may be attributed to relatively short acquisition time of a single HEXRD pattern (1 s). As a consequence, ω peaks with a low intensity cannot be distinguished as they are close to the noise level.

Heating of the HPT sample exhibits a similar evolution of the phase composition as the non-deformed material. First, ω_{ath} phase partly dissolves upon heating and is followed by continuous growth and coarsening of the ω_{iso} phase with increasing temperature. ω_{iso} particles dissolve at the same temperature range as in the non-deformed sample. On the other hand, due to accelerated precipitation of the α phase, α peaks are observed already at lower temperatures than in the non-deformed material. Contrary to the non-deformed material, ω and α phase coexist in the HPT material at 550 °C.

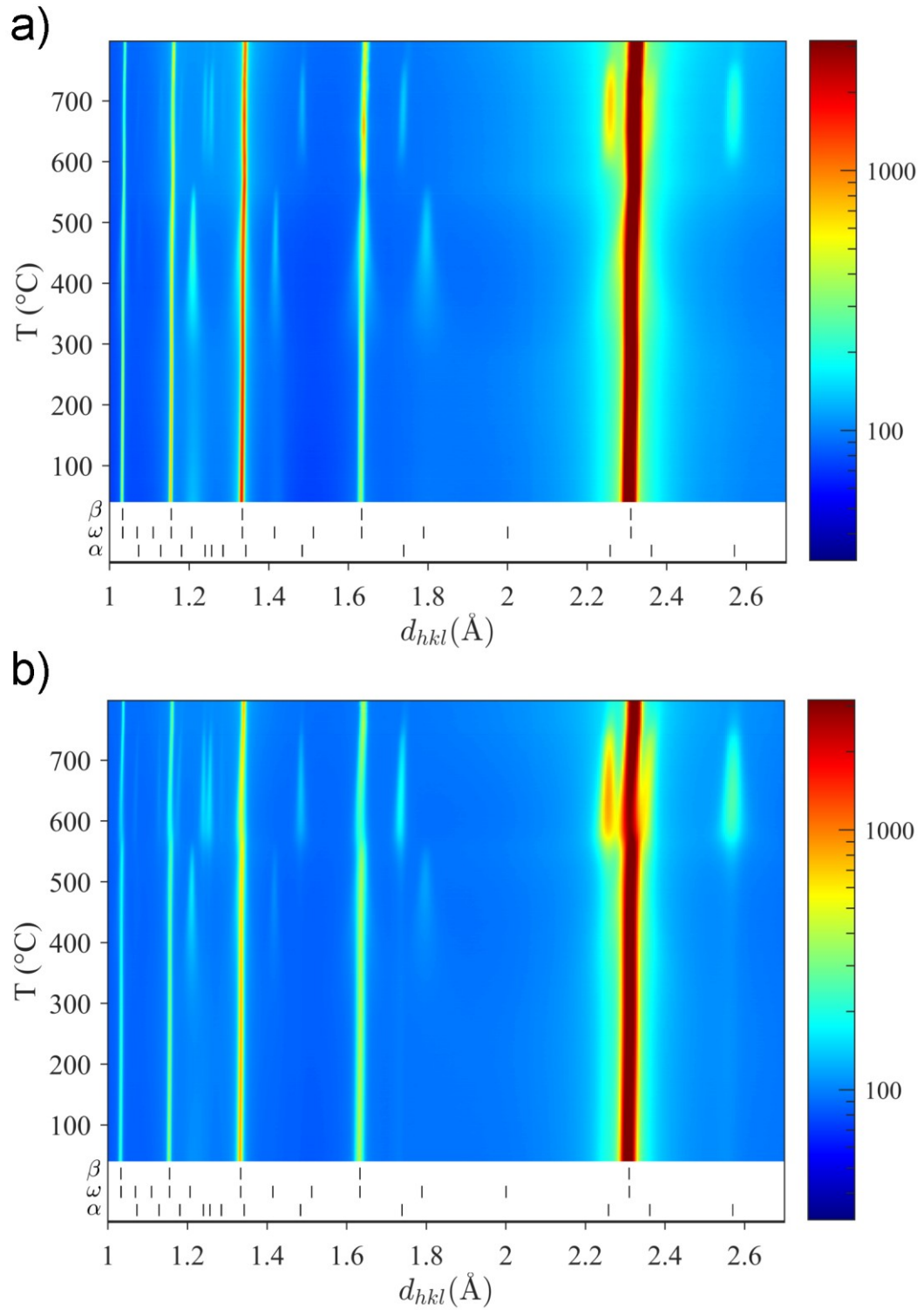


Figure 4.31 Two-dimensional plot of diffracted intensities collected during heating of the (a) non-deformed and (b) HPT-deformed Ti15Mo alloy. The logarithmic scale bar of intensities, and peak positions of individual phases (β , ω , and α) are also shown on the right side and below the plot, respectively.

4.3.2 In-situ electrical resistance measurement

The evolution of electrical resistance was measured employing the same temperature regime as for in-situ HEXRD measurements, i.e. during linear heating with the heating rate of 5 °C/min from room temperature to 750 °C. The result of the measurement is shown in Figure 4.32. Note that the specific electrical resistivity of the material cannot be determined due to a complex shape of the sample required for the measurement (see Figure 3.3). In order to compare results obtained from different samples, relative electrical resistance is calculated by dividing the measured resistance by the reference value of the electrical resistance of the same sample measured at the beginning of heating (at 40 °C).

In Figure 4.32, the black and red lines represent the evolution of the relative electrical resistance of the non-deformed and HPT-deformed Ti15Mo alloy, respectively. The non-deformed material was studied in previous work by Zháňal et al. [37]. According to this work, the description of electrical resistance measurements is based on separation of the evolution to several stages corresponding to the monotonous increase and/or decrease of electrical resistance.

In the non-deformed material, the stage 1 (RT – 250 °C) corresponds to the first decrease of relative electrical resistance which is caused by the dissolution of ω_{ath} particles [19]. In the vicinity of the β/ω interface, the elastic strain fields act as scattering zones for conducting electrons [142]. Thus, during heating at this temperature range ω_{ath} particles dissolve, the elastic strain fields are continuously released and the matrix is cleared for electron drift and as a consequence, electrical resistance decreases. The decrease is lower in the HPT sample because the material contains a high density of lattice defects which act as obstacles for electron drift even after dissolution of ω_{ath} particles.

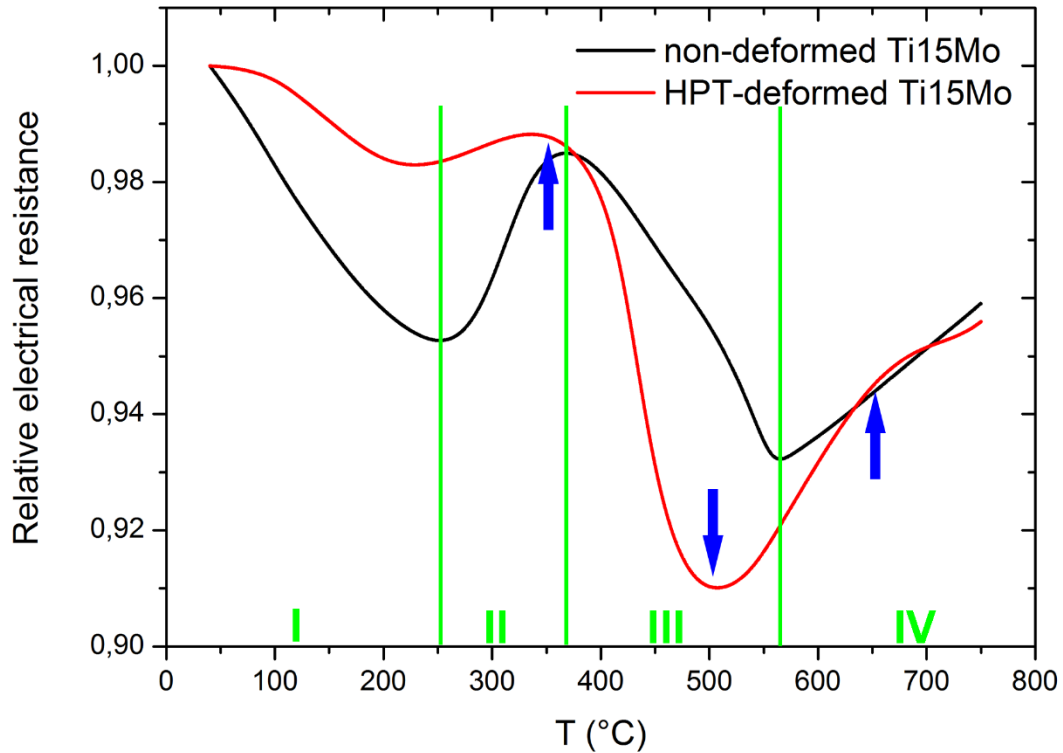


Figure 4.32 Temperature dependence of relative electrical resistance of the non-deformed and HPT-deformed Ti15Mo alloy. The green lines and marks indicate individual stages of the evolution of electrical resistance for the non-deformed sample. The temperatures selected for subsequent ex-situ observations are indicated by blue arrows.

In the second stage (250 °C – 365 °C), the increase of relative electrical resistance is caused by formation and growth of ω_{iso} particles [143], resulting in an increasing amount of β/ω interfaces [144]. The increase of electrical resistance is reduced in stage II for the HPT specimen, since electrical resistivity of the HPT material is arises both from lattice defects and ω phase particles.

In stage III (365 °C – 560 °C), the relative electrical resistance decreases with increasing temperature. The reason of the decline is the decreasing amount of β/ω interfaces due to simultaneous growth of ω_{iso} particles and a decrease of their volume fraction [38]. In the HPT material, the decrease of electrical resistivity is even more pronounced. The dissolution of ω phase is slightly accelerated due to earlier precipitation of the α phase and more importantly, recovery and recrystallization processes contribute to the drop of the electrical resistance. The minimum of the electrical resistance is achieved at a lower temperature of 500 °C in the HPT material than in the non-deformed material. This may be attributed to $\beta \rightarrow \alpha$ transformation being shifted to lower temperatures in the HPT material which outweighs the effect of

ω phase dissolution. Due to simultaneous α precipitation and ω phase dissolution, the abrupt change in the slope is not observed in the HPT specimen. Note that the particular temperature of individual extremes does not correspond to the onset of a new phase transformation. It is rather related to the temperature at which the new process (electron scattering mechanism) prevails over the previous one.

The stage IV (560 °C – 750 °C) shows an abrupt change of slope of the relative electrical resistance of the non-deformed specimen which is caused by a sudden dissolution of ω_{iso} phase [37]. The increase of electrical resistance of the non-deformed material is almost linear in this temperature range, suggesting that the undergoing precipitation of α phase has only a limited effect on the electrical resistance. A possible explanation can be that the volume fraction of α phase is relatively low, even though the precipitates are large. The number of β/α interfaces which affect electrical resistance is therefore negligible. Further heating of the HPT sample shows a small peak between 600 °C and 700 °C. This can be associated with the increased volume fraction of α phase, which is observed by HEXRD. As the temperature approaches the β -transus temperature (~ 770 °C), the equilibrium α phase content decreases, resulting in a dissolution of α phase precipitates in the vicinity of the β -transus temperature.

4.3.3 In-situ transmission electron microscopy

In-situ observation by TEM during heating was performed with the aim to directly observe the microstructure changes in the HPT material during annealing. The sample was heated with the heating rate of 50 °C/min to the temperature of 700 °C and subsequently isothermally aged for 30 minutes.

The TEM BF image in Figure 4.33(a) shows the heavily deformed microstructure of the HPT-deformed Ti15Mo alloy before heating. In Figure 4.33(b), the microstructure of the sample after in-situ heating and isothermal ageing at 700 °C is shown. It is apparent that the microstructure of the specimen in the observable area by TEM (i.e. in the transparent area for electrons) did not change significantly. This result is confusing and contradicts previously achieved results. The same sample was observed also using BSE in SEM – the results significantly differing from TEM observations can be seen in Figure 4.34. The explanation for the lack of α phase particles in the TEM in-situ experiment lies in the reduced thickness of the TEM foil. The thickness of the TEM foil increases from the top right corner to the bottom left corner (Figure 4.34). It is clearly visible that in the thin part of the specimen, α phase

particles did not precipitate. On the other hand, with increasing thickness of the sample, coarser α particles can be observed, which is in accordance with all previous results. The fundamental reason of this difference can be attributed to the so-called “thin foil effect” [145]. Note that only a thin part of the foil can be observed by TEM which explains why no α phase formation was observed. The transparent part of the thin foil may be considered as a two dimensional object and therefore diffusion is significantly reduced. As a result, α phase cannot nucleate in this regions even at the temperature of 700 °C.

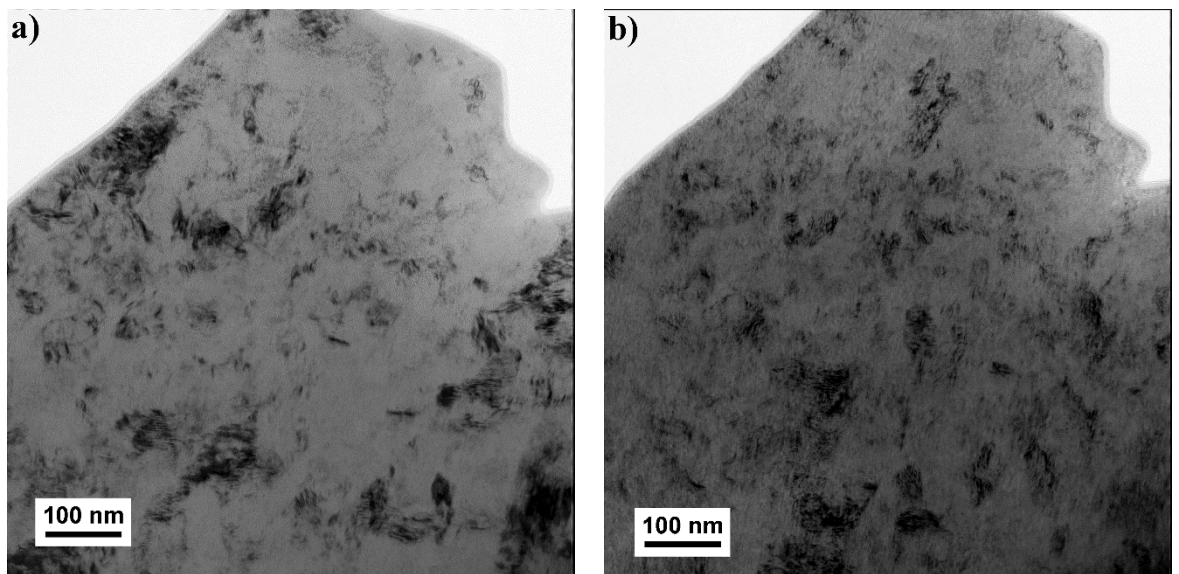


Figure 4.33 In-situ TEM observation: (a) TEM BF image from the sample before thermal treatment, and (b) TEM BF image from the same area of the specimen after thermal treatment.

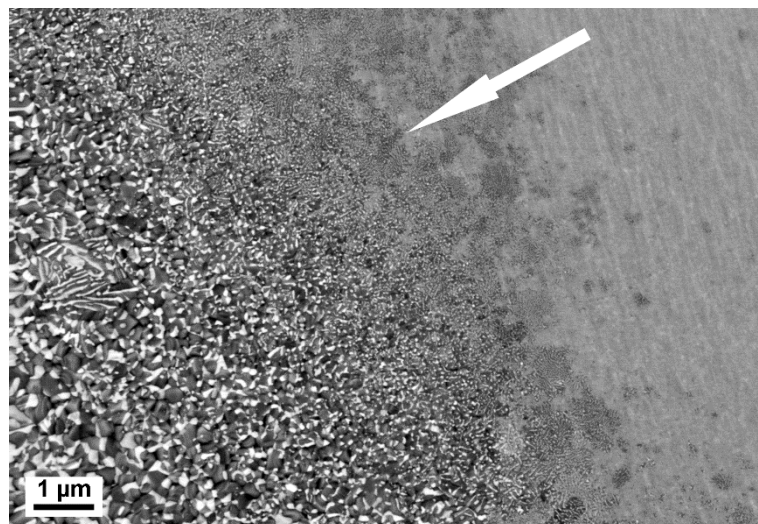


Figure 4.34 SEM–BSE micrograph of the TEM sample. The white arrow indicates the increasing thickness of the sample.

Detailed microstructural observation of the sample was done in the thicker part, where α particles are visible by SEM. The SEM–BSE micrograph in Figure 4.35 shows both chemical contrast (darker α precipitates due to Mo depletion) and a remarkable contrast due to the topography of the specimen. Lighter areas which are attributed to grains of the β phase exhibit “step-like” structures on the surface. This structure can be a consequence of the internal stress imposed by precipitation of α phase particles.

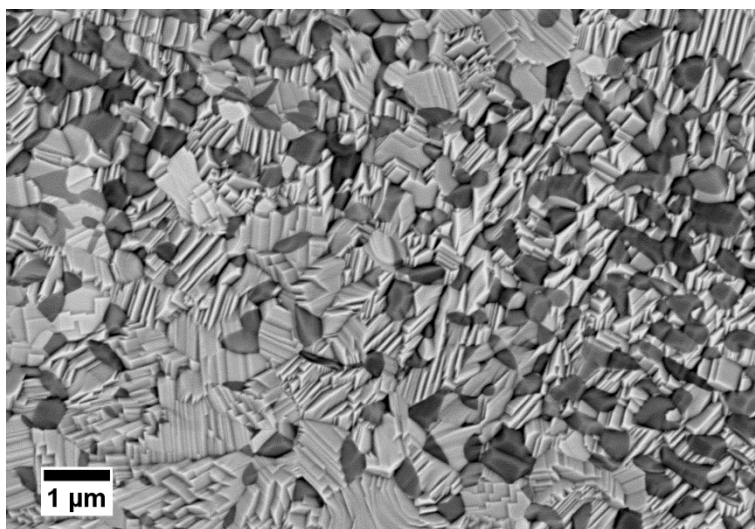


Figure 4.35 SEM–BSE micrograph of the thicker part of the TEM sample.

4.4 Ex-situ observations based on the resistivity measurement

Based on the in-situ measurement presented in Section 4.3, three temperatures were chosen to obtain more insight into the undergoing phase transformations in the HPT material. The temperatures 350 °C, 500 °C, and 650 °C, where the evolution of the electrical resistance undergoes distinctive changes, were selected for ex-situ (post mortem) experiments as indicated by blue arrows in Figure 4.32.

The individual samples were heated with controlled heating rate of 5 °C/min in an inert atmosphere to the desired temperature and immediately quenched in water.

4.4.1 Microstructure observed by TEM

The microstructure of the samples in each heating condition was observed using TEM.

4.4.1.1 Heating to the temperature of 350 °C

In Figure 4.36(a), the SAED pattern of the HPT sample heated to 350 °C is shown. The angular averaging and indexing of the diffraction pattern revealed that the material contains both β and ω phases. The microstructure is similar to the non-heated counterpart (Ti15Mo after HPT deformation) as it is shown in TEM BF image

presented in Figure 4.36(b). TEM DF image from one β phase reflection (highlighted by a red arrow in Figure 4.36(a)) is shown in Figure 4.36(c). The β grains are ultra-fine with the grain size ~ 200 nm and contain a high density of dislocations.

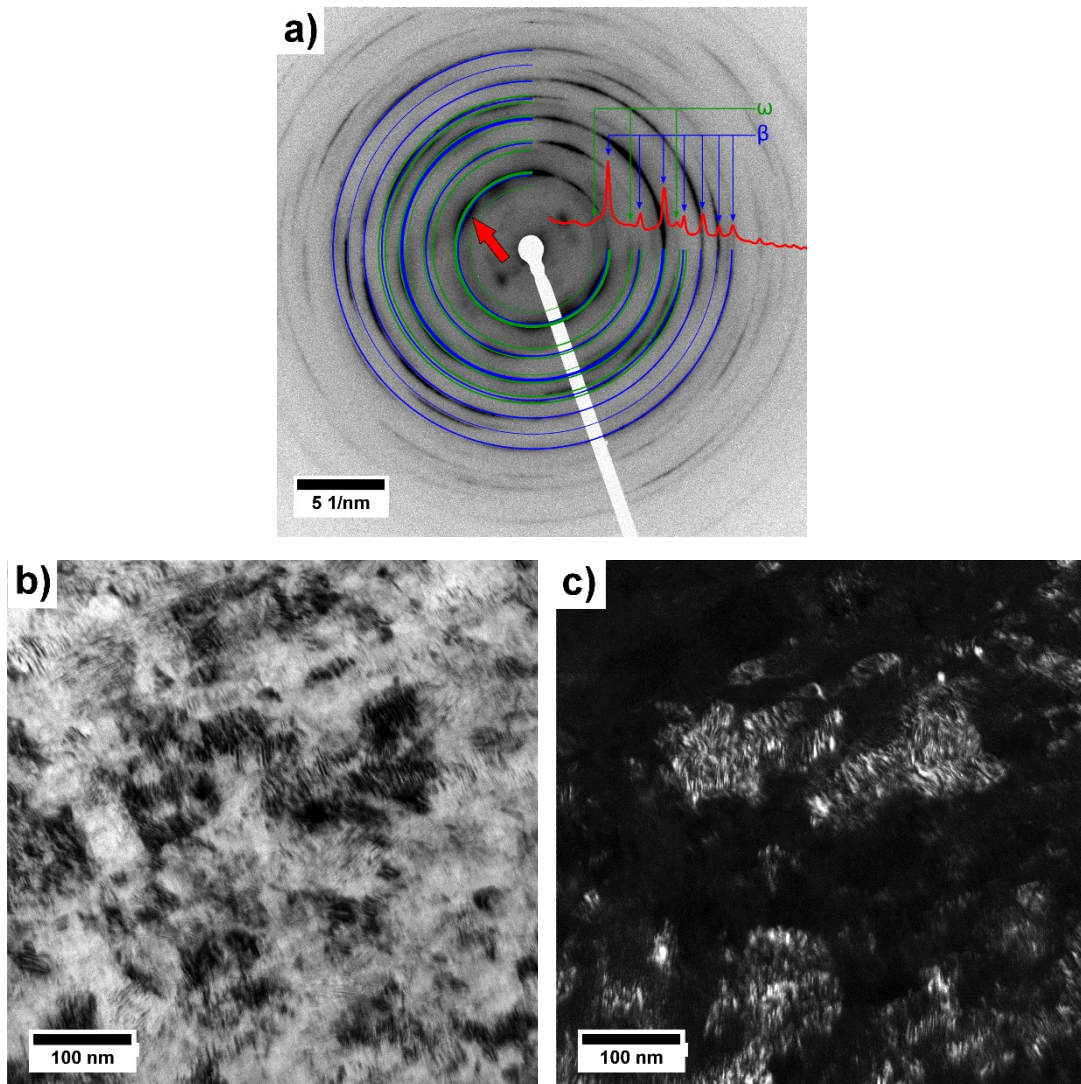


Figure 4.36 Ti15Mo alloy after HPT deformation and heating to 350 °C (a) SAED pattern with evaluated phases and highlighted β phase reflection used for TEM DF image, (b) TEM BF image, and (c) TEM DF image.

4.4.1.2 Heating to the temperature of 500 °C

Figure 4.37(a) shows the SAED pattern of the Ti15Mo alloy after heating to 500 °C. It can be observed, that the SAED pattern consists of concentric circles, indicating the persisting UFG structure, and also clearly visible diffraction points which can be attributed to new α precipitates and to recrystallized β grains. The evaluation of the SAED pattern revealed that all β , ω , and α phases are present in the specimen. The TEM bright and dark field images in Figure 4.37(b) and (c) indicate a still severely deformed UFG structure.

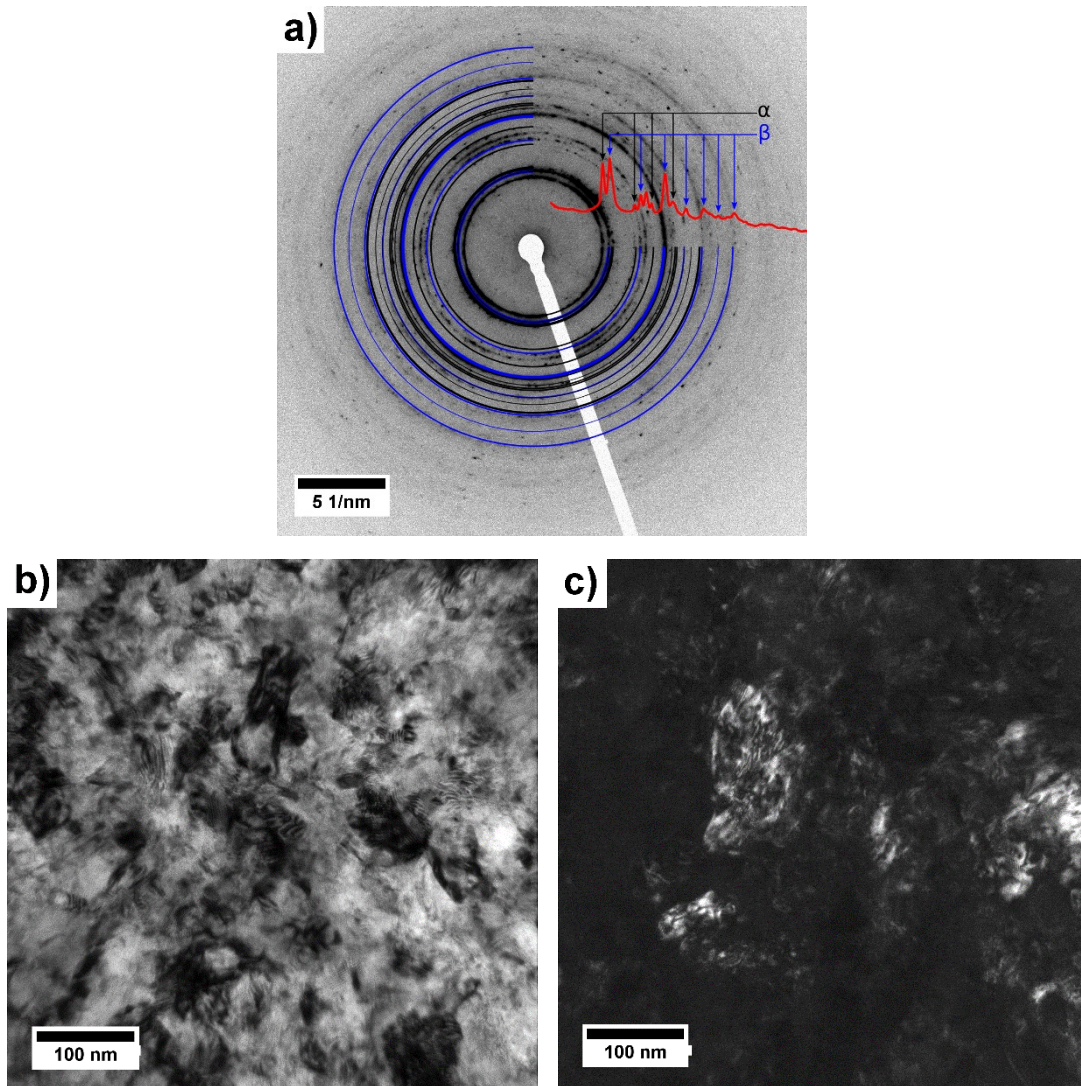


Figure 4.37 Ti15Mo alloy after HPT deformation and heating to 500 °C (a) SAED pattern with evaluated phases, (b) TEM BF image, and (c) TEM DF image from one β phase reflection.

4.4.1.3 Heating to the temperature of 650 °C

Heating of the HPT sample up to the temperature of 650 °C significantly changed its microstructure. The microstructure consists of a mixture of UFG β and α phases (note the lower magnification of the images in Figure 4.38 compared to images in Sections 4.4.1.1 and 4.4.1.2). In the TEM micrograph presented in Figure 4.38(a), the recrystallized microstructure is seen with the central β grain in diffraction contrast (indicated by the red arrow). The β grain is tilted to the zone axis $[110]_{\beta}$ and the corresponding SAED pattern is displayed in Figure 4.38(b). Weak distorted diffraction spots corresponding to ω phase are the diffraction spots of the ω_{ath} phase formed during quenching of the specimen after heating. Figure 4.38(c) shows the TEM BF image from the same area as in Figure 4.38(a), but tilted such that the grain

of the α phase indicated by the red arrow is in diffraction contrast (zone axis $[11-20]_{\alpha}$). The corresponding SAED pattern is shown in Figure 4.38(d). Note that β grains are still deformed and contain a high density of dislocations, while grains of the α phase seem to be defect-free.

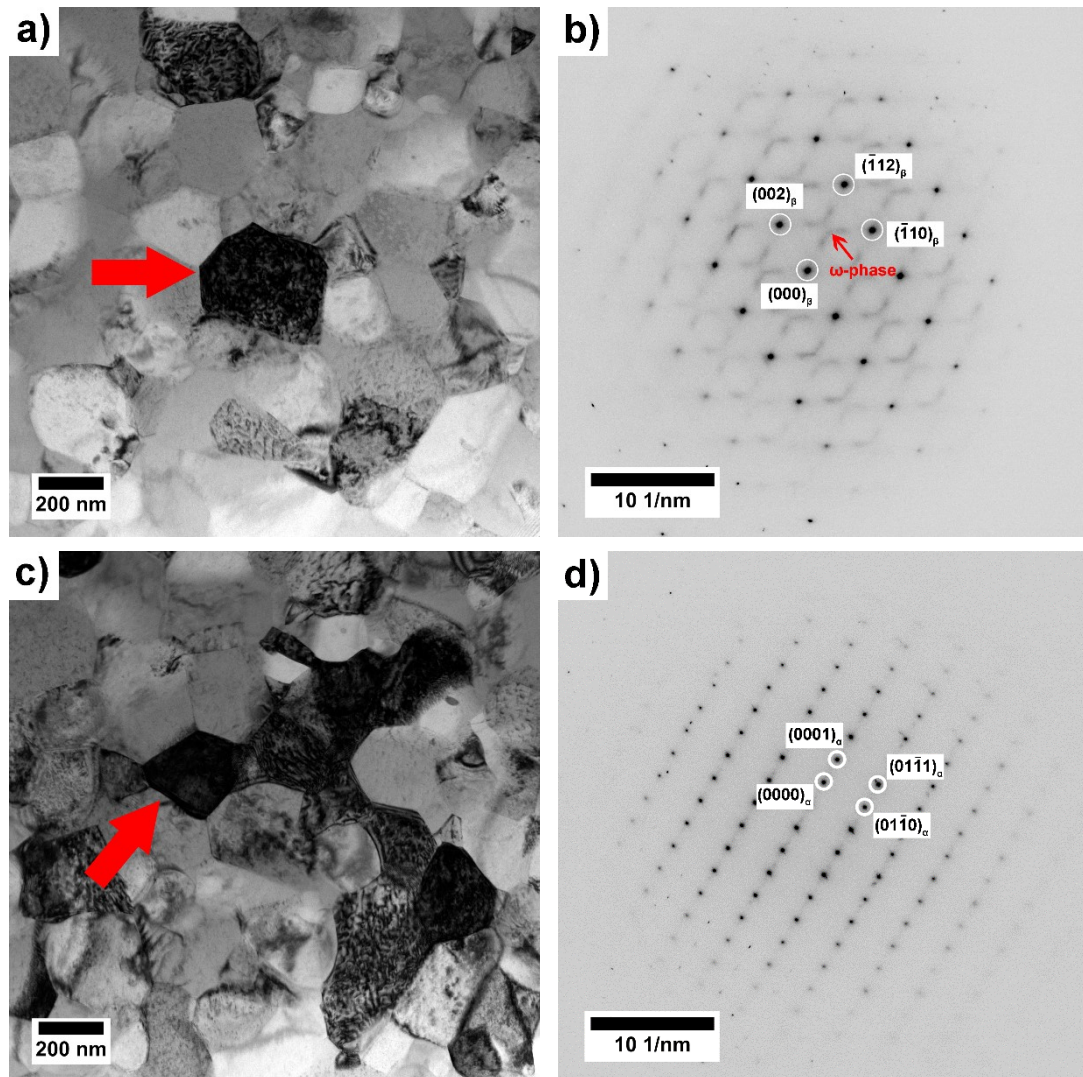


Figure 4.38 Ti15Mo alloy after heating to 650 °C: (a) TEM BF image with a β grain in diffraction contrast, indicated by a red arrow, and (b) the corresponding SAED pattern, (c) TEM BF image with an α grain in diffraction contrast, indicated by a red arrow, and (d) the corresponding SAED pattern.

The microstructure of the specimen heated to 650 °C was observed also using ACOM-TEM. The phase map containing α and β phases overlaid with reliability map is shown in Figure 4.39. The microstructure remains UFG even after heating to 650 °C and contain β and α grains with the grain size ~ 300 nm.

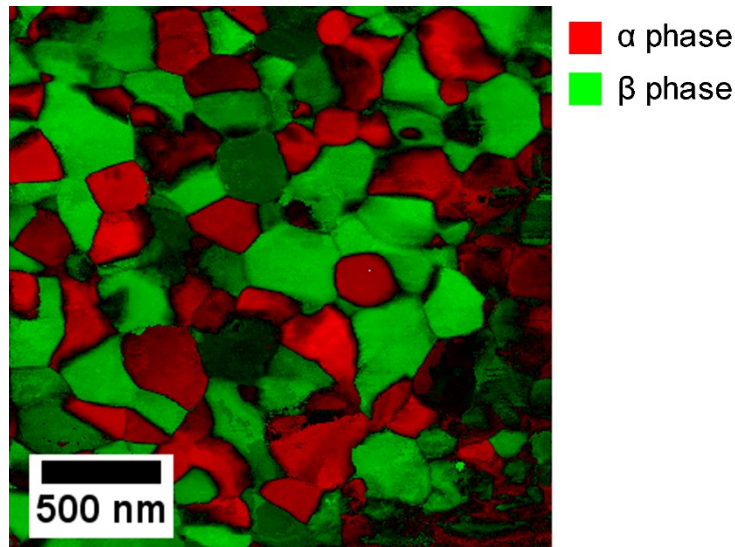


Figure 4.39 Microstructure of the Ti15Mo alloy after heating to 650 °C observed using ACOM-TEM. The red color corresponds to α phase grain, the green to β grains.

4.4.2 Phase composition

The phase composition of the samples heated to 350 °C, 500 °C, and 650 °C was finally investigated using HEXRD by synchrotron radiation. The individual XRD patterns corresponding to each heating temperature are shown in Figure 4.40, where the dependence of the intensity on the interplanar distance d_{hkl} is displayed in logarithmic scale. The evaluated volume fractions of individual phases present in the material are summarized in Table 4.4. For clarity, the phase composition of the HPT material (without heating) is also shown.

Heating of the sample to 350 °C results in a similar HEXRD pattern as for the non-heated material. The evaluation of the phase composition revealed a comparable volume fraction of the ω phase within experimental error. After heating to 500 °C, the ω phase almost completely dissolved, while the α phase is already present in the material in a significant volume fraction. Heating to 650 °C results in disappearance of ω particles and a two phase $\alpha+\beta$ structure.

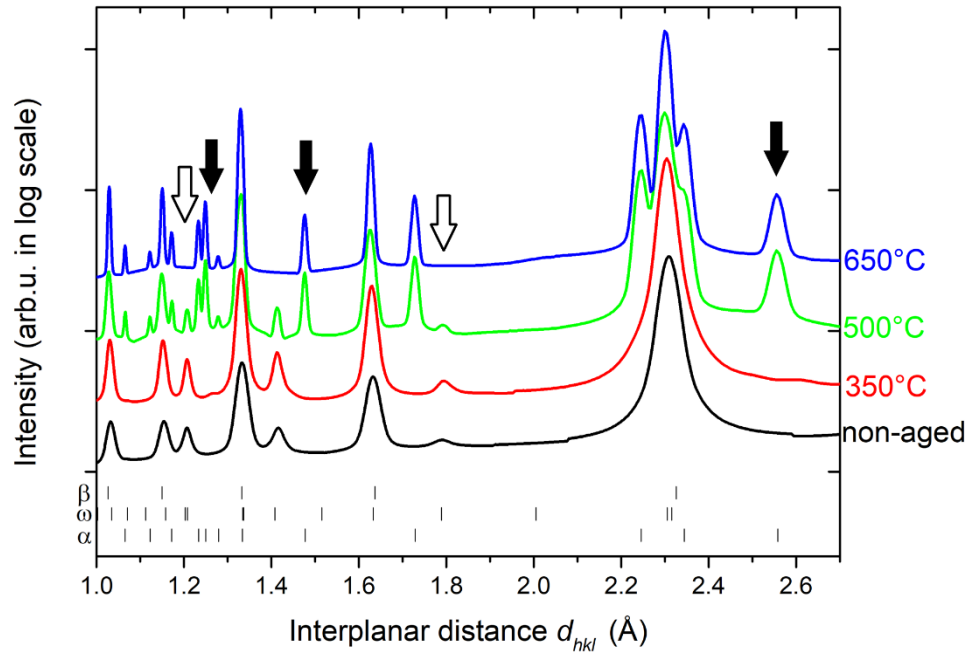


Figure 4.40 HEXRD patterns of the Ti15Mo HPT sample after heating to temperatures 350 °C, 500 °C and 650 °C. The intensity is shown in logarithmic scale. Individual HEXRD patterns are shifted for clarity.

Table 4.4 Volume fraction of individual phases in Ti15Mo HPT samples without heating and heated to temperatures 350 °C, 500 °C, 650 °C determined by HEXRD.

	Volume fraction of the β phase	Volume fraction of the ω phase	Volume fraction of the α phase
HPT sample	$72\% \pm 5\%$	$28\% \pm 5\%$	-
HPT sample heated to 350 °C	$77\% \pm 4\%$	$23\% \pm 3\%$	-
HPT sample heated to 500 °C	$64\% \pm 3\%$	$2\% ^2$	$34\% \pm 3\%$
HPT sample heated to 650 °C	$69\% \pm 4\%$	-	$31\% \pm 4\%$

² The ω phase is clearly present in the material as observed in the HEXRD pattern (Figure 4.40) and its volume fraction was estimated as 2 %; however, this estimation is subjected to significant uncertainty and true volume fraction might be slightly lower or significantly higher (up to 6 %).

5 DISCUSSION

In this section the results obtained in the thesis are discussed in detail. The chapter consists of 5 subchapters. Firstly, the effect of HPT and ECAP deformation on the microstructure, phase composition and microhardness of Ti15Mo alloy is discussed. The second subchapter is devoted to the comparison of phase transformations in non-deformed and HPT material during linear heating. In contrast, the effect of isothermal annealing/ageing on the non-deformed and deformed materials is treated in the third subchapter. The fourth chapter discusses the enhanced precipitation of the α phase after deformation and its morphology. The last one deals with the effect of the ageing on the microhardness in all three materials conditions.

5.1 Effect of deformation introduced by severe plastic deformation

5.1.1 Effect of high pressure torsion

The Ti15Mo alloy in the solution treated condition was subjected to one revolution of high pressure torsion (HPT). The microstructure observed by TEM exhibits a highly deformed, UFG structure. Furthermore, EDS imaging showed chemical inhomogeneities, which may affect the subsequent α phase precipitation as discussed below.

Available literature is not conclusive on whether HPT deformation results in an increased or decreased content of ω phase. In studies [115, 146] the authors reported a decreased volume fraction of the ω phase after HPT deformation in Ti15Mo alloy and attributed it to the reverse $\omega \rightarrow \beta$ transformation during deformation [147]. On the other hand, Kilmametov et al. in study [148] claimed that the ω phase content may be increased after SPD processing thanks to a deformation induced ω phase.

Our results indicate that the standard XRD measurement is unable to determine the volume fraction of the ω phase. This is caused by several reasons, namely due to the extreme peak broadening caused by a nanometer-sized of ω particles, overlapping of many β and ω peaks and preferred orientation of grains. On the other hand, HEXRD measurements, which provide more reliable data due to higher signal to noise ratio and bigger interaction volume showed, that the HPT material contains ~ 28 % of the ω phase. In comparison with the solution treated Ti15Mo alloy, where the volume fraction of the ω phase is 40 % [134], the HPT material exhibits a decreased amount of the ω particles (it should be noted, that the volume fraction of the ω phase in ST

material was determined using neutron diffraction which provides more accurate results compared to HEXRD).

The microhardness increase in sample processed by one HPT turn is remarkable – it increases from ~ 278 HV (non-deformed sample) up to values of ~ 400 HV. This increase can be attributed to significant grain refinement and high density of lattice defects. Our previous study showed that microhardness after 10 HPT revolutions further increased to ~ 450 HV [96]. As reported in [149], ageing at $375\text{ }^\circ\text{C}/16\text{ h}$ of the non-deformed material results in even higher microhardness of ~ 490 HV, and was attributed to the formation of ω_{iso} phase which, however, causes significant embrittlement. In contrast, the microhardness of the Ti15Mo alloy in the coarse-grained aged $\alpha+\beta$ condition (without ω phase content) is ~ 293 HV, which is just slightly higher than in non-aged condition [149].

5.1.2 Effect of equal channel angular pressing

Equal channel angular pressing (ECAP; 2 passes) was another SPD method used for deformation of the solution treated Ti15Mo alloy. Contrary to the HPT samples, the grain fragmentation is not significant and processing by ECAP results in formation of deformed and twinned structure. This difference is substantiated by comparing the equivalent strain by HPT – $\varepsilon_{VM} = 36$ (1 HPT turn on the periphery part of the specimen) and by ECAP – $\varepsilon_{VM} = 1.33$ (2 ECAP passes), which is not sufficient for significant grain fragmentation in the β phase condition. Nevertheless, the deformation results in the formation of shear bands as already reported for ECAP materials elsewhere [117, 150, 151]. These SBs consist of dislocation cells with high density of dislocations [137].

XRD results suggest that fraction of the ω phase may have increased after ECAP deformation of the ST material (although laboratory XRD cannot give us a reliable quantitative result). This conclusion is supported by measured significant increase of microhardness which cannot be explained by induced deformation only [96]. The increased amount of the ω particles in Ti15Mo alloy after ECAP was caused also by processing at the elevated temperature of $250\text{ }^\circ\text{C}$ which is sufficient for the formation of ω_{iso} phase particles stabilized by diffusion [19]. It should be noted that lower temperatures disallow successful ECAP processing due to insufficient ductility of material, while higher temperatures promote phase transformations – namely formation of ω phase causing embrittlement [152, 153].

5.2 Phase transformations during linear heating

Linear heating with the heating rate of 5 °C/min allows direct comparison between results of electrical resistance measurements and data achieved using synchrotron radiation by HEXRD. Moreover, direct comparison with recent study by Zháňal et al. [37] is possible. In-situ measurements revealed significant differences in the evolution of phase composition between non-deformed and HPT material.

At room temperature, both materials consist of the mixture of $\beta + \omega_{ath}$ phases as proved in several studies of the non-deformed material [35, 37, 154] and in this thesis by means of HEXRD in both conditions. During linear heating, the content of ω_{ath} phase decreases in both conditions which is manifested by decreasing intensity of the HEXRD peak at $d_{hkl} \approx 1.2 \text{ \AA}$ in Figure 4.31 [18]. The same behavior was observed by measurement of electrical resistance also in other metastable β Ti alloy, namely in Ti LCB [155]. The decrease of ω_{ath} can be also inferred from the determination of elastic constants during heating by ultra-sound methods [113]. ω_{ath} particles increase both electrical resistance and elastic modulus of Ti15Mo alloy. The decrease of both these quantities during heating can be therefore related to the decrease of ω_{ath} phase content. This overall trend is reversed at the temperature of about 250 °C in the non-deformed material, and related to the onset of dominance of ω_{iso} phase formation by diffusion processes [16]. On the other hand, in the HPT material the onset of diffusional stabilization of ω_{iso} particles may occur at lower temperatures due to enhanced diffusion by high concentration of lattice defects. This assumption is consistent with electrical resistance measurement (see Figure 4.32), but unfortunately cannot be confirmed by in-situ HEXRD measurement due to extreme peak broadening caused by severe deformation.

HEXRD and electron diffraction in TEM proved the presence of β and ω phases in the HPT material heated to 350 °C. Direct TEM observation showed that microstructure remains in severely deformed and UFG condition.

Further heating results in progressive dissolution of ω_{iso} particles. In the non-deformed material, the complete dissolution of the ω_{iso} phase occurs at the temperature of 560 °C, which is manifested by the abrupt change in the evolution of the electrical resistance (cf. Figure 1 in [37], see also Figure 4.32 in Section 4.3.2, black curve).

The dissolution of the ω_{iso} phase during linear heating occurs also in the HPT material, but α phase nucleates at significantly lower temperatures. The in-situ

HEXRD indicates that α phase peaks are present already after heating to 500 °C (see Figure 4.31). Moreover, post mortem TEM observation of samples heated to 500 °C showed new, strain-free grains of α phase in SAED pattern (individual diffraction spots) and HEXRD proved a high volume fraction of α phase (~ 34 %). Hence, the coexistence of the β , ω , and α phases at 500 °C in HPT specimen was confirmed. Such coexistence of the β , ω , and α phases does not occur in the non-deformed material after heating at the rate of 5 °C/min. On the other hand, the coexistence of three phases was observed in the non-deformed material after isothermal annealing as described in Section 4.2.1.1.

The ex-situ observation of the HPT sample heated up to 650 °C showed two-phase $\alpha+\beta$ structure, which is recovered, but still UFG. The size of both β grains and α precipitates is comparable in range of 200 – 500 nm. Grains of both phases are equiaxed with polygonal shape, which is common for β grains, but very uncommon for α phase precipitates which grow as lamellae in the non-deformed coarse-grained material. It may be expected that in the HPT material, all α precipitates nucleate at the triple points of the UFG β matrix which results in their equiaxed shape. Similar morphology of α phase was also observed after isothermal annealing, and is discussed in detail in the following section.

5.3 Effect of isothermal annealing on phase composition and microstructure

All three type of studied materials – non-deformed, HPT and ECAP materials were subjected to isothermal annealing/ageing treatments in order to study the differences between phase transformation's sequence and microstructure evolution.

5.3.1 Non-deformed material

Ageing of the non-deformed material at 400 °C results in growth of ω_{iso} phase particles. These particles can be observed by SEM after ageing at 400 °C for 16h (Figure 4.10). Ageing at temperature of 500 °C causes precipitation of α phase. α phase particles precipitate first as large continuous lamellae along some β/β grain boundaries (GB α). Consequently, small lamellae of α phase grow from the GB α into the grain interior. α lamellae in the vicinity of the grain boundaries form a special acicular shape in order to reduce elastic distortion and create a coherent interface [9]. Moreover, the lamellar morphology satisfies the Burgers orientation relation and may indicate low

interfacial energy [46]. As a result α lamellae grow only into one of the adjacent β grains.

A significant amount of the ω phase is still retained in the material even after ageing at 500 °C/16 h – the material consists of a GB α + lamellar α + ellipsoidal ω particles in the β matrix as proved by TEM. Site-specific study by TEM (see Section 4.2.1.1) proved that ellipsoidal particles observed by SEM are ω particles with the size of approximately 100 – 200 nm along their longer axis. To our best knowledge, such observation of the ω phase using standard SEM methods has not been reported previously.

5.3.2 Deformed materials

In the deformed conditions (both HPT and ECAP) the α phase precipitation is accelerated – α peaks in XRD patterns and small α particles in SEM-BSE images are visible even after ageing at 400 °C for 1 h. With increasing ageing time, the amount of the α phase increases in SPD-processed materials along with the continuous decrease of the volume fraction of the ω phase.

A significant difference in the evolution of phases in the non-deformed and SPD materials can be observed also after ageing at 500 °C. While ω phase is retained in the non-deformed material, it completely disappears from the SPD-processed materials (visible mainly for ECAP material in Figure 4.25) after isothermal annealing at 500 °C. Enhanced precipitation of the α phase causes rejection of the β stabilizing Mo to the surrounding β matrix. This causes thermodynamic stabilization of the β matrix and suppresses the formation of the ω phase [156]. Similar preference of α phase precipitation over ω phase formation was observed in Ti-25Nb-2Mo-4Sn alloy deformed by cold-rolling [157].

5.4 Enhanced α phase precipitation in deformed materials

SPD-processing substantially enhances the precipitation of the α phase. In HPT material the enhanced precipitation occurs almost homogeneously. In contrary, in the ECAP material, the enhanced precipitation is localized in pre-existing shear bands containing high density of lattice defects which were formed by ECAP processing.

Dislocations and high density of grain boundaries in both HPT and ECAP conditions serve as nucleation sites for α particles by reducing the energy barrier for nucleation [9].

Once nucleated, the growth of α nuclei is diffusion-controlled [158], which means that coarsening of the α phase is controlled by the diffusion of Mo (β stabilizing element) in the β matrix. It is known, that the diffusion rate along grain boundaries and pipe diffusion along dislocation cores are several orders of magnitude higher than the bulk diffusion [51, 159]. The growth of the α precipitates is therefore also accelerated. The accelerated precipitation of the α phase in SPD-processed metastable β Ti alloys was reported in several studies [115, 118]. In addition, different alloys, such Al [151, 160] or Mg alloys [161] also exhibit enhanced formation of the high temperature stable phase upon thermal treatment.

Dense network of preferential nucleation sites results in high density of α nuclei. The growth of individual α phase particles is therefore limited by two processes. First, each α precipitate causes a barrier for the growth of another α precipitate due to impingement. Second, each α nuclei causes a barrier for the diffusion of Mo which limits the growth of α particles due to additional β stabilization of surrounding β matrix. As a result, α phase particles remain small and equiaxed in zones with high density of lattice defects.

The observation of the microstructure of the aged HPT material revealed an inhomogeneous precipitation of α particles (see Figure 4.11). It is reported that such inhomogeneity is caused by shear bands which are formed in the material after HPT deformation [114, 115, 117, 118]. However, we did not observe any shear bands in the HPT material. Contrarily, we observed chemical inhomogeneities in the non-deformed material and also in the HPT sample. In the latter case the inhomogeneities are elongated in the direction of deformation after HPT (see Sections 4.1.1 and 4.1.2). The nucleation of the α phase particles may be promoted in the areas with lower Mo content.

The heterogeneous growth of α phase lamellae occurs in the material after ageing of the ECAP specimen at 500 °C/16 h. The resulting microstructure resembles a discontinuous coarsening of lamellar structure which was observed in various alloying systems [162–164]. Discontinuous coarsening typically originates at grain boundaries of the parent matrix [162]. In our case, discontinuous coarsening is initiated in shear bands, as the driving force for the discontinuous coarsening arises from lowering the total energy of the system by decreasing the area of grain boundaries and decreasing interfacial area between phases. Parallel α lamellae are observed in Figure 4.12 (500 °C/16 h) which suggests that only one variant of α lamellae evolved in each

β grain. The preferred selection of the variants of α phase during $\beta \rightarrow \alpha$ transformation was reported for different alloys in studies [165, 166]. As a result of extra driving force causing discontinuous coarsening in the shear bands, the microstructure becomes coarser than in the non-deformed material.

It must be noted that phase transformations in metastable β Ti alloys have been thoroughly investigated in detail in coarse-grained polycrystalline materials or even in single crystals [19, 34, 37, 42, 46, 108, 113, 154, 167–170]. The effect of possible remaining lattice defects, such as dislocations or grain boundaries have been neglected in most of these studies. The key conclusion of our work is that the lattice defects have a significant impact on phase transformations and the morphology of particles in metastable β Ti alloys.

5.5 Effect of ageing on the microhardness

The hardness of the metastable β Ti alloys after SPD deformation and ageing depends on many factors as different several strengthening mechanisms operate in these materials.

Firstly, the severe plastic deformation causes grain fragmentation by introducing a high amount of grain boundaries and thus strengthens the material as it is described by Hall-Petch relation (Equation 1.10) [57, 58].

Secondly, severe plastic deformation introduces a high density of dislocations into the material causing significant dislocation strengthening. Upon subsequent ageing, the density of dislocations decreases by recovery and recrystallization. Furthermore, grain size increases. The effect of strengthening by dislocations and grain boundaries is therefore generally reduced by ageing.

Thirdly, the precipitates and their evolution during ageing play also an important role in strengthening. Despite limited knowledge of interactions between ω particles and dislocations, it can be assumed, that moving dislocations pass through (cut) ω_{ath} particles (known as Friedel effect [171]) as these particles are small, coherent and moreover, the $\beta \rightarrow \omega_{ath}$ transformation may be incomplete - only small shifts of atomic planes may take place after quenching [34]. The shear stress required for a dislocation to pass through a precipitate increases with the size of the particle (within Friedel's limit) and/or with the strength of the obstacle to dislocation motion [171, 172]. As the precipitates reaches the critical size (typically 5 – 30 nm) the stress for dislocation to pass through a precipitate is too high and the Orowan mechanism prevails – the

dislocation bends around the particle until it is enclosed completely and the dislocation can move on, leaving a dislocation loop around the bypassed particle [171]. The stress required to bow-out the particles during Orowan mechanism is inversely proportional to the radius of precipitates and correlate with the volume fraction of particles.

As shown in Figure 4.30, the ageing of all three studied materials at 400 °C results in an increased and similar microhardness values. The increase of the microhardness can be attributed to the effect of the ω phase - the nano-sized ω particles are stabilized by diffusion, their size increases and they can become significantly stronger obstacles for dislocation motion. The effect of ω phase particles outweighs the possible effect of refined microstructure after severe plastic deformation. The decreasing microhardness of the HPT material after longer ageing time at 400 °C (for 16 hours) can be related to the decreasing volume fraction of the ω phase. Recovery of defects and recrystallization of microstructure may also contribute to the reduction of microhardness.

The microhardness of all studied materials is lower after ageing at 500 °C than after ageing at 400 °C and also continuously decreases with increasing ageing time. The relative decrease of microhardness of the non-deformed material can be caused by increasing size of ω particles, which is well beyond the Friedel's limit and, is consistent with fundamentals of Orowan mechanism, namely that the increasing size of particles reduces the magnitude of precipitate strengthening. However, the non-deformed material after ageing at 500 °C still shows higher microhardness than the non-aged counterpart. It can be attributed to the fact that ω phase is still retained in the material as proved by XRD, TEM and SEM analysis. The same trend of decreasing microhardness with longer ageing time at 500 °C is observable for HPT and ECAP materials. Moreover, the microhardness of deformed materials is comparable to microhardness achieved in non-aged condition. It can be caused by decreasing volume fraction of the ω phase (or complete dissolution) and also a possible recovery of defects and recrystallization of the microstructure.

According to the microhardness evolution after ageing at 400 °C, the microhardness would eventually saturate similarly as in metastable Ti-6.8Mo-4.5Fe-1.5Al alloy [108]. The microhardness of the Ti15Mo alloy subjected to 10 revolutions of HPT does not exceed 450 HV [95] and the CG material can be also hardened only to ~ 450 – 500 HV by appropriate heat treatment promoting precipitation of ω and α particles. Hence, it can be concluded, that for Ti15Mo alloy

the microhardness cannot exceed 500 HV disregarding the processing and thermal treatment.

Several authors have proposed strategies how to improve mechanical properties by optimization of SPD parameters and by subsequent annealing treatment in Al alloys [173], Mg alloys [174], steels [175] or in Ti alloys [88]. In the case of the studied metastable Ti15Mo alloy, the advantage of SPD processing in β condition followed by thermal treatment is uncertain when the improvement of mechanical properties is concerned only. The effect of severely deformed microstructure is dominated by effect of phase transformations and the size of α phase precipitates is similar in coarse-grained and severely deformed material. However, two important findings concerning improvement of mechanical properties are promising, despite a detailed study of mechanical properties is beyond the scope of this thesis.

First, equiaxed α phase particles precipitate in the HPT material in contrast to α lamellae in the non-deformed counterpart. Equiaxed particles positively affect the strength and reduce the potential anisotropy of mechanical properties caused by lamellar microstructure, especially in a textured material.

Second, severe deformation of parent β phase and the introduction of high density of defects significantly enhances the α phase precipitation. Side effect of this enhancement is the reduced content of ω phase and the disappearance of ω phase at comparatively low temperatures. ω phase causes material embrittlement and its reduction at low temperature may result in good combination of strength and ductility.

6 CONCLUSIONS

This thesis aimed to investigate the effect of the ultra-fine grained microstructure on phase transformations upon thermal treatments in metastable β Ti15Mo alloy. The ultra-fine grained and deformed microstructure of the material was achieved by severe plastic deformation of high pressure torsion (HPT) and equal channel angular pressing (ECAP).

The most important findings of this research, structured according to the aims set of the thesis, can be summarized as follows:

Characterization of the effect of severe plastic deformation on the microstructure of the alloy.

- Deformation by HPT results in ultra-fine grained, severely deformed microstructure with a high density of lattice defects.
- Deformation by ECAP does not exhibit significant grain fragmentation. Nevertheless, the microstructure observation revealed a deformed, twinned microstructure with shear bands consisting of nano-sized grains with high density of dislocations.

Analysis of the ageing response of the Ti15Mo alloy processed by severe plastic deformation.

- Upon isothermal annealing/ageing of the non-deformed material, α phase precipitates preferentially at grain boundaries (GB α) and in the vicinity of grain boundaries as lamellae.
- In deformed materials the formation of the α phase is accelerated and it forms at lower ageing time and temperature. Moreover, the particles of the α phase remain equiaxed in deformed materials even after long time ageing.
- Isothermal annealing of the non-deformed material results in a coexistence of all three phases of β , ω , and α .

Comparison of phase transformations in Ti15Mo alloy occurring upon heating in non-deformed and deformed materials.

- During linear heating of the non-deformed material with a constant heating rate, the complete dissolution of the ω_{iso} phase occurs at 560 °C. Nucleation and growth of the α phase occurs subsequently at higher temperatures.
- In the HPT material the α phase formation is shifted to lower temperatures; a significant amount of α particles was detected already after heating to the temperature of 500 °C.

Investigation of the enhanced precipitation of the α phase in severely deformed alloy.

- The nucleation of the α phase in deformed materials is enhanced due to high density of lattice defects, such as dislocations or grain boundaries, which act as preferential nucleation sites.
- The accelerated growth of α particles in deformed materials is promoted by fast diffusion paths along grain boundaries and dislocations.
- The shape of α particles remains equiaxed in deformed materials; dense network of preferential nucleation sites resulted in fine and equiaxed precipitates whose growth is impeded by impingement with other α particles and also by increased amount of β stabilizing Mo, which is expelled from the α precipitates to the surrounding β matrix.

The following general key conclusions can be drawn from this research:

1. In severely deformed materials with high density of lattice defects, the nucleation and growth of phases forming via diffusional transformation (in our case α phase) are accelerated due to preferential nucleation at lattice defects and enhanced diffusion along grain boundaries and dislocations.
2. The enhanced precipitation of the α phase in deformed metastable β Ti alloys also leads to the faster dissolution of the ω precipitates which cause material embrittlement. Thus, lower temperatures are needed for thermomechanical treatment of the deformed metastable β Ti alloy in order to achieve duplex $\alpha+\beta$ structure.

3. Phase transformations occurring in single crystal or in coarse-grained metastable β Ti alloys have been thoroughly investigated and reported in literature. However, to our best knowledge, none of the studies systematically assessed the effect of lattice defects on phase transformations in this class of materials. Nevertheless, as it was shown, lattice defects (grain boundaries and dislocations) greatly affect the sequence of phase transformations occurring upon thermal treatment.

BIBLIOGRAHY

- [1] LÜTJERING, G. and J.C. WILLIAMS. *Titanium*. Berlin, Heidelberg: Springer Berlin Heidelberg, 2007.
- [2] LEYENS, C. and M. PETERS. *Titanium and titanium alloys*. B.m.: Wiley-VCH., 2003.
- [3] POLMEAR, I. *Light Alloys*. B.m.: Butterworth-Heinemann, 2005.
- [4] HABASHI, F. *Handbook of Extractive Metallurgy*. 2nd ed. 1997.
- [5] DONACHIE, M.J. *Titanium: a technical guide*. 2nd ed. Materials Park, OH: ASM International, 2000.
- [6] BOYER, R.R. An overview on the use of titanium in the aerospace industry. *Materials Science and Engineering: A*. 1996, vol. 213, no. 1, pp. 103–114.
- [7] BREME, J., E. EISENBARTH and V. BIEHL. Titanium and its Alloys for Medical Applications. In: C. LEYENS and M. PETERS, eds. *Titanium and Titanium Alloys*. B.m.: Wiley-VCH Verlag GmbH & Co. KGaA, 2003, p. 423-451.
- [8] FROES, F.H. and M. QIAN. *Titanium in Medical and Dental Applications*. B.m.: Woodhead Publishing, 2018.
- [9] PORTER, D.A., K.E. EASTERLING and M.Y.A. SHERIF. *Phase Transformations in Metals and Alloys*. London: CRC Press, 2009.
- [10] FROES, F.H. *Titanium: Physical Metallurgy Processing and Applications*. Materials Park, OH: ASM International, 2015.
- [11] FROST, P.D., W.M. PARRIS, L.L. HIRSCH, J.R. DOIG and C.M. SCHWARTZ. Isothermal transformation of titanium-chromium alloys. *Trans. Asm*. 1954, vol. 46, pp. 231–256.
- [12] HARDY, H. and A. AESM. THE STRUCTURE OF THE ω PRECIPITATE 1636 IN TITANIUM-16% VANADIUM ALLOY. In: *Symposium on the mechanism of phase transformations in metals*. B.m.: Institute of Metals, 1955, p. 93.
- [13] BAGARIATSKII, I.A., G.I. NOSOVA and T.V. TAGUNOVA. Factors in the formation of metastable phases in titanium-base alloys. *Soviet Physics Doklady*. 1959, vol. 3, pp. 1014–1018.
- [14] ZHENG, Y., R.E.A. WILLIAMS, D. WANG, R. SHI, S. NAG, P. KAMI, J.M. SOSA, R. BANERJEE, Y. WANG and H.L. FRASER. Role of ω phase in the formation of extremely refined intragranular α precipitates in metastable β -titanium alloys. *Acta Materialia*. 2016, vol. 103, pp. 850–858.
- [15] JONES, N.G., R.J. DASHWOOD, M. JACKSON and D. DYE. β Phase decomposition in Ti–5Al–5Mo–5V–3Cr. *Acta Materialia*. 2009, vol. 57, no. 13, pp. 3830–3839.
- [16] BANERJEE, S. and P. MUKHOPADHYAY. *Phase transformations: examples from titanium and zirconium alloys*. Amsterdam, Oxford: Pergamon, 2007.

- [17] LIU, H., M. NIINOMI, M. NAKAI and K. CHO. Athermal and deformation-induced ω -phase transformations in biomedical beta-type alloy Ti-9Cr-0.2O. *Acta Materialia*. 2016, vol. 106, pp. 162–170.
- [18] HICKMAN, B.S. The formation of omega phase in titanium and zirconium alloys: A review. *Journal of Materials Science*. 1969, vol. 4, no. 6, pp. 554-563.
- [19] ZHÁŇAL, P., P. HARCUBA, J. ŠMILAUEROVÁ, J. STRÁSKÝ, M. JANEČEK, B. SMOLA and M. HÁJEK. Phase Transformations in Ti-15Mo Investigated by in situ Electrical Resistance. *Acta Physica Polonica A*. 2015, vol. 128, no. 4, pp. 779–783.
- [20] DE FONTAINE, D., N.E. PATON and J.C. WILLIAMS. The omega phase transformation in titanium alloys as an example of displacement controlled reactions. *Acta Metallurgica*. 1971, vol. 19, no. 11, pp. 1153–1162.
- [21] JAMIESON, J.C. Crystal Structures of Titanium, Zirconium, and Hafnium at High Pressures. *Science*. 1963, vol. 140, no. 3562, pp. 72–73.
- [22] BAGARYATSKIY, A.Y. and I.G. NOSOVA. *Physics of Metals and Metallography*. 1962.
- [23] KUAN, T.S., R.R. AHRENS and S.L. SASS. The stress-induced omega phase transformation in Ti-V alloys. *Metallurgical Transactions A*. 1975, vol. 6, no. 9, pp. 1767–1774.
- [24] FROES, F.H., D. EYLON and H.B. BOMBERGER. *Titanium technology: present status and future trends*. Dayton: Titanium Development Association, 1985.
- [25] NAG, S. *Influence of Beta Instabilities on the Early Stages of Nucleation and Growth of Alpha in Beta Titanium Alloys*. Dissertation thesis: The Ohio State University, 2008.
- [26] JAFFEE, R.I. and H.M. BURTE. *Titanium Science and Technology*. Berlin, Heidelberg: Springer, 1973.
- [27] BANERJEE, D., A.K. GOGIA, T.K. NANDI and V.A. JOSHI. A new ordered orthorhombic phase in a Ti3Al-Nb alloy. *Acta Metallurgica*. 1988, vol. 36, no. 4, pp. 871–882.
- [28] BENDERSKY, L.A., W.J. BOETTINGER, B.P. BURTON, F.S. BIANCANIELLO and C.B. SHOEMAKER. The formation of ordered ω -related phases in alloys of composition Ti4Al3Nb. *Acta Metallurgica et Materialia*. 1990, vol. 38, no. 6, pp. 931–943.
- [29] WELSCH, G., R. BOYER and E.W. COLLINGS. *Materials Properties Handbook: Titanium Alloys*. B.m.: ASM International, 1993.
- [30] ROSENBERG, H.W. Titanium alloying in theory and practice. In: R. I. JAFFEE, ed. *Science, Technology, And Application of Titanium*. Oxford: Pergamon Press, 1970, p. 851–859.
- [31] BANIA, P.J. Beta titanium alloys and their role in the titanium industry. *JOM*. 1994, vol. 46, no. 7, pp. 16–19.

- [32] DE FONTAINE, D. Mechanical instabilities in the b.c.c. lattice and the beta to omega phase transformation. *Acta Metallurgica*. 1970, vol. 18, no. 2, pp. 275–279.
- [33] GORNOSTYREV, Y.N. and M.I. KATSNELSON. Misfit stabilized embedded nanoparticles in metallic alloys. *Physical Chemistry Chemical Physics*. 2015, vol. 17, no. 41, pp. 27249–27257.
- [34] ŠMILAUEROVÁ, J., P. HARCUBA, D. KRIEGNER and V. HOLÝ. On the completeness of the $\beta \rightarrow \omega$ transformation in metastable β titanium alloys. *Journal of Applied Crystallography*. 2017, vol. 50, no. 1, pp. 283–287.
- [35] DEVARAJ, A., S. NAG, R. SRINIVASAN, R.E.A. WILLIAMS, S. BANERJEE, R. BANERJEE and H.L. FRASER. Experimental evidence of concurrent compositional and structural instabilities leading to ω precipitation in titanium–molybdenum alloys. *Acta Materialia*. 2012, vol. 60, no. 2, pp. 596–609.
- [36] SILCOCK, J.M. An X-ray examination of the ω phase in TiV, TiMo and TiCr alloys. *Acta Metallurgica*. 1958, vol. 6, no. 7, pp. 481–493.
- [37] ŽHÁŇAL, P., P. HARCUBA, M. HÁJEK, B. SMOLA, J. STRÁSKÝ, J. ŠMILAUEROVÁ, J. VESELÝ and M. JANEČEK. Evolution of ω phase during heating of metastable β titanium alloy Ti–15Mo. *Journal of Materials Science*. 2018, vol. 53, no. 1, pp. 837–845.
- [38] DEVARAJ, A., R.E.A. WILLIAMS, S. NAG, R. SRINIVASAN, H.L. FRASER and R. BANERJEE. Three-dimensional morphology and composition of omega precipitates in a binary titanium–molybdenum alloy. *Scripta Materialia*. 2009, vol. 61, no. 7, pp. 701–704.
- [39] WILLIAMS, J.C. and M.J. BLACKBURN. The influence of misfit on the morphology and stability of the omega phase in titanium-transition metal alloys. *Transactions of the Metallurgical Society of AIME*. 1969, vol. 245, pp. 2352–2355.
- [40] PRIMA, F., P. VERMAUT, G. TEXIER, D. ANSEL and T. GLORANT. Evidence of α -nanophase heterogeneous nucleation from ω particles in a β -metastable Ti-based alloy by high-resolution electron microscopy. *Scripta Materialia*. 2006, vol. 54, no. 4, pp. 645–648.
- [41] AZIMZADEH, S. and H.J. RACK. Phase transformations in Ti-6.8Mo-4.5Fe-1.5Al. *Metallurgical and Materials Transactions A*. 1998, vol. 29, no. 10, pp. 2455–2467.
- [42] NAG, S., R. BANERJEE, R. SRINIVASAN, J.Y. HWANG, M. HARPER and H.L. FRASER. ω -Assisted nucleation and growth of α precipitates in the Ti-5Al-5Mo-5V-3Cr-0.5Fe β titanium alloy. *Acta Materialia*. 2009, vol. 57, no. 7, pp. 2136–2147.
- [43] LI, T., D. KENT, G. SHA, L.T. STEPHENSON, A.V. CEGUERRA, S.P. RINGER, M.S. DARGUSCH and J.M. CAIRNEY. New insights into the phase transformations to isothermal ω and ω -assisted α in near β -Ti alloys. *Acta Materialia*. 2016, vol. 106, pp. 353–366.

- [44] BURGERS, W.G. On the process of transition of the cubic-body-centered modification into the hexagonal-close-packed modification of zirconium. *Physica*. 1934, vol. 1, no. 7, pp. 561–586.
- [45] DUERIG, T.W., G.T. TERLINDE and J.C. WILLIAMS. Phase transformations and tensile properties of Ti-10V-2Fe-3Al. *Metallurgical Transactions A*. 1980, vol. 11, no. 12, pp. 1987–1998.
- [46] FURUHARA, T., T. MAKINO, Y. IDEI, H. ISHIGAKI, A. TAKADA and T. MAKI. Morphology and Crystallography of α Precipitates in β Ti–Mo Binary Alloys. *Materials Transactions, JIM*. 1998, vol. 39, no. 1, pp. 31–39.
- [47] MAKINO, T., R. CHIKAIZUMI, T. NAGAOKA, T. FURUHARA and T. MAKINO. Microstructure development in a thermomechanically processed Ti15V3Cr3Sn3Al alloy. *Materials Science and Engineering: A*. 1996, vol. 213, no. 1, pp. 51–60.
- [48] OKADA, M. Strengthening of Ti-15V-3Cr-3Sn-3Al by thermo-mechanical treatments. *ISIJ International*. 1991, vol. 31, no. 8, pp. 834–839.
- [49] FURUHARA, T., S. TAKAGI, H. WATANABE and T. MAKI. Crystallography of grain boundary α precipitates in a β titanium alloy. *Metallurgical and Materials Transactions A*. 1996, vol. 27, no. 6, pp. 1635-1646.
- [50] LOVE, G.R. Dislocation pipe diffusion. *Acta Metallurgica*. 1964, vol. 12, no. 6, pp. 731–737.
- [51] AARONSON, H.I., M. ENOMOTO and J.K. LEE. *Mechanisms of Diffusional Phase Transformations in Metals and Alloys*. London: CRC Press, 2010.
- [52] VALIEV, R.Z., R.K. ISLAMGALIEV and I.V. ALEXANDROV. Bulk nanostructured materials from severe plastic deformation. *Progress in Materials Science*. 2000, vol. 45, no. 2, pp. 103–189.
- [53] SAKAI, T. Dynamic and Post-Dynamic Recrystallization under Hot, Cold and Severe Plastic Deformation Conditions. *Progress in Materials Science*. 2014, vol. 60, no. 1, pp. 130–207.
- [54] ESTRIN, Y. and A. VINOGRADOV. Extreme grain refinement by severe plastic deformation: A wealth of challenging science. *Acta Materialia*. 2013, vol. 61, no. 3, pp. 782–817.
- [55] ZEHETBAUER, M.J., G. STEINER, E. SCHAFLENER, A.V. KOZNIKOV and E.A. KORZNIKOVA. Deformation Induced Vacancies with Severe Plastic Deformation: Measurements and Modelling. *Materials Science Forum*. 2006, vol. 503, pp. 57–64.
- [56] LANGDON, T.G. Twenty-five years of ultrafine-grained materials: Achieving exceptional properties through grain refinement. *Acta Materialia*. 2013, vol. 61, no. 19, pp. 7035–7059.
- [57] HALL, E.O. The Deformation and Ageing of Mild Steel: III Discussion of Results. *Proceedings of the Physical Society. Section B*. 1951, vol. 64, no. 9, p. 747.
- [58] PETCH, N.J. The Cleavage Strength of Polycrystals. *Journal of the Iron and Steel Institute*. no date, vol. 1953, no. 174, pp. 25–28.

- [59] SEGAL, V.M. Materials processing by simple shear. *Materials Science and Engineering: A*. 1995, vol. 197, no. 2, pp. 157–164.
- [60] VALIEV, R.Z. and T.G. LANGDON. Principles of equal-channel angular pressing as a processing tool for grain refinement. *Progress in Materials Science*. 2006, vol. 51, pp. 881–981.
- [61] ZHILYAEV, A.P. and T.G. LANGDON. Using high-pressure torsion for metal processing: Fundamentals and applications. *Progress in Materials Science*. 2008, vol. 53, no. 6, pp. 893–979.
- [62] SAITO, Y., H. UTSUNOMIYA, N. TSUJI and T. SAKAI. Novel ultra-high straining process for bulk materials—development of the accumulative roll-bonding (ARB) process. *Acta Materialia*. 1999, vol. 47, no. 2, pp. 579–583.
- [63] MISHRA, R.S., M.W. MAHONEY, S.X. MCFADDEN, N.A. MARA and A.K. MUKHERJEE. High strain rate superplasticity in a friction stir processed 7075 Al alloy. *Scripta Materialia*. 1999, vol. 42, no. 2, pp. 163–168.
- [64] VALIEV, R.Z., Y.V. IVANISENKO, E.F. RAUCH and B. BAUDELET. Structure and deformation behaviour of Armco iron subjected to severe plastic deformation. *Acta Materialia*. 1996, vol. 44, no. 12, pp. 4705–4712.
- [65] SONG, Y., E.Y. YOON, D.J. LEE, J.H. LEE and H.S. KIM. Mechanical properties of copper after compression stage of high-pressure torsion. *Materials Science and Engineering: A*. 2011, vol. 528, no. 13, pp. 4840–4844.
- [66] ISLAMGALIEV, R.K., W. BUCHGRABER, Y.R. KOLOBOV, N.M. AMIRKHANOV, A.V. SERGUEEVA, K.V. IVANOV and G.P. GRABOVETSKAYA. Deformation behavior of Cu-based nanocomposite processed by severe plastic deformation. *Materials Science and Engineering: A*. 2001, vols. 319–321, pp. 872–876.
- [67] ISLAMGALIEV, R.K., N.F. YUNUSOVA, I.N. SABIROV, A.V. SERGUEEVA and R.Z. VALIEV. Deformation behavior of nanostructured aluminum alloy processed by severe plastic deformation. *Materials Science and Engineering: A*. 2001, vols. 319–321, pp. 877–881.
- [68] SABIROV, I. and R. PIPPAN. Formation of a W–25%Cu nanocomposite during high pressure torsion. *Scripta Materialia*. 2005, vol. 52, no. 12, pp. 1293–1298.
- [69] MISHRA, R.S., V.V. STOLYAROV, C. ECHER, R.Z. VALIEV and A.K. MUKHERJEE. Mechanical behavior and superplasticity of a severe plastic deformation processed nanocrystalline Ti–6Al–4V alloy. *Materials Science and Engineering: A*. 2001, vol. 298, no. 1, pp. 44–50.
- [70] STOLYAROV, V.V., Y.T. ZHU, T.C. LOWE, R.K. ISLAMGALIEV and R.Z. VALIEV. Processing nanocrystalline Ti and its nanocomposites from micrometer-sized Ti powder using high pressure torsion. *Materials Science and Engineering: A*. 2000, vol. 282, no. 1, pp. 78–85.
- [71] ZHILYAEV, A.P., S. LEE, G.V. NURISLAMOVA, R.Z. VALIEV and T.G. LANGDON. Microhardness and microstructural evolution in pure nickel during high-pressure torsion. *Scripta Materialia*. 2001, vol. 44, no. 12, pp. 2753–2758.

- [72] SAKAI, G., K. NAKAMURA, Z. HORITA and T.G. LANGDON. Developing high-pressure torsion for use with bulk samples. *Materials Science and Engineering: A*. 2005, vol. 406, no. 1, pp. 268–273.
- [73] UM, H.Y., E.Y. YOON, D.J. LEE, C.S. LEE, L.J. PARK, S. LEE and H.S. KIM. Hollow cone high-pressure torsion: Microstructure and tensile strength by unique severe plastic deformation. *Scripta Materialia*. 2014, vol. 71, pp. 41–44.
- [74] HORITA, Z. Development of High-Pressure Sliding Process for Microstructural Refinement of Rectangular Metallic Sheets. *ResearchGate*. 2009, vol. 50, no. 4, pp. 930–933.
- [75] IWAHASHI, Y., J. WANG, Z. HORITA, M. NEMOTO and T.G. LANGDON. Principle of equal-channel angular pressing for the processing of ultra-fine grained materials. *Scripta Materialia*. 1996, vol. 35, no. 2, pp. 143–146.
- [76] RABKIN, E., I. GUTMAN, M. KAZAKEVICH, E. BUCHMAN and D. GORNI. Correlation between the nanomechanical properties and microstructure of ultrafine-grained copper produced by equal channel angular pressing. *Materials Science and Engineering: A*. 2005, vol. 396, no. 1, pp. 11-21.
- [77] LIN, H.K., J.C. HUANG and T.G. LANGDON. Relationship between texture and low temperature superplasticity in an extruded AZ31 Mg alloy processed by ECAP. *Materials Science and Engineering: A*. 2005, vol. 402, no. 1, pp. 250–257.
- [78] LATYSH, V.V., I.P. SEMENOVA, G.H. SALIMGAREEVA, I.V. KANDAROV, Y.T. ZHU, T.C. LOWE and R. VALIEV. Microstructure and Properties of Ti Rods Produced by Multi-Step SPD. *Materials Science Forum*. 2006.
- [79] KIM, H.S., W.S. RYU, M. JANECEK, S.C. BAIK and Y. ESTRIN. Effect of Equal Channel Angular Pressing on Microstructure and Mechanical Properties of IF Steel. *Advanced Engineering Materials*. 2005, vol. 7, nos. 1–2, pp. 43-46.
- [80] IWAHASHI, Y., Z. HORITA, M. NEMOTO and T.G. LANGDON. Factors influencing the equilibrium grain size in equal-channel angular pressing: Role of Mg additions to aluminum. *Metallurgical and Materials Transactions A*. 1998, vol. 29, no. 10, pp. 2503–2510.
- [81] RAAB, G.J., R.Z. VALIEV, T.C. LOWE and Y.T. ZHU. Continuous processing of ultrafine grained Al by ECAP–Conform. *Materials Science and Engineering: A*. 2004, vol. 382, no. 1, pp. 30–34.
- [82] POPOV, A.A., I.Yu. PYSHMINTSEV, S.L. DEMA KOV, A.G. ILLARIONOV, T.C. LOWE, A.V. SERGEYEVA and R.Z. VALIEV. Structural and mechanical properties of nanocrystalline titanium processed by severe plastic deformation. *Scripta Materialia*. 1997, vol. 37, no. 7, pp. 1089-1094.

- [83] STOLYAROV, V.V., Y.T. ZHU, I.V. ALEXANDROV, T.C. LOWE and R.Z. VALIEV. Influence of ECAP routes on the microstructure and properties of pure Ti. *Materials Science and Engineering: A*. 2001, vol. 299, no. 1, pp. 59–67.
- [84] SHIN, D.H., I. KIM, J. KIM, Y.S. KIM and S.L. SEMIATIN. Microstructure development during equal-channel angular pressing of titanium. *Acta Materialia*. 2003, vol. 51, no. 4, pp. 983–996.
- [85] KIM, I., J. KIM, D.H. SHIN, C.S. LEE and S.K. HWANG. Effects of equal channel angular pressing temperature on deformation structures of pure Ti. *Materials Science and Engineering: A*. 2003, vol. 342, no. 1, pp. 302–310.
- [86] KO, Y.G., W.S. JUNG, D.H. SHIN and C.S. LEE. Effects of temperature and initial microstructure on the equal channel angular pressing of Ti–6Al–4V alloy. *Scripta Materialia*. 2003, vol. 48, no. 2, pp. 197–202.
- [87] STOLYAROV, V.V., Y.T. ZHU, I.V. ALEXANDROV, T.C. LOWE and R.Z. VALIEV. Grain refinement and properties of pure Ti processed by warm ECAP and cold rolling. *Materials Science and Engineering: A*. 2003, vol. 343, no. 1, pp. 43–50.
- [88] VALIEV, R.Z., A.V. SERGUEEVA and A.K. MUKHERJEE. The effect of annealing on tensile deformation behavior of nanostructured SPD titanium. *Scripta Materialia*. 2003, vol. 49, no. 7, pp. 669–674.
- [89] SERGUEEVA, A.V., V.V. STOLYAROV, R.Z. VALIEV and A.K. MUKHERJEE. Enhanced superplasticity in a Ti-6Al-4V alloy processed by severe plastic deformation. *Scripta Materialia*. 2000, vol. 43, no. 9, pp. 819–824.
- [90] SAITOVA, L.R., H.W. HÖPPEL, M. GÖKEN, I.P. SEMENOVA, G.I. RAAB and R.Z. VALIEV. Fatigue behavior of ultrafine-grained Ti–6Al–4V ‘ELI’ alloy for medical applications. *Materials Science and Engineering: A*. 2009, vol. 503, nos. 1–2, pp. 145–147.
- [91] SAITOVA, L.R., H.W. HÖPPEL, M. GÖKEN, I.P. SEMENOVA and R.Z. VALIEV. Cyclic deformation behavior and fatigue lives of ultrafine-grained Ti-6Al-4V ELI alloy for medical use. *International Journal of Fatigue*. 2009, vol. 31, no. 2, pp. 322–331.
- [92] ZHANG, B., X. ZHANG, X.Y. ZHANG, Y.Z. JIA, M.Z. MA, R.P. LIU and Q. JING. Effects of microstructure on the mechanical properties of a high-strength Ti₂₀Zr_{6.5}Al₄V alloy. *Journal of Alloys and Compounds*. 2018, vol. 735, pp. 2133–2141.
- [93] ZHEREBTSOV, S.V., E.A. KUDRYAVTSEV, G.A. SALISCHEV, B.B. STRAUMAL and S.L. SEMIATIN. Microstructure evolution and mechanical behavior of ultrafine Ti₆Al₄V during low-temperature superplastic deformation. *Acta Materialia*. 2016, vol. 121, pp. 152–163.
- [94] BARTHA, K., P. ZHÁŇAL, J. STRÁSKÝ, J. ČÍŽEK, M. DOPITA, F. LUKÁČ, P. HARCUBA, M. HÁJEK, V. POLYAKOVA, I. SEMENOVA and M. JANEČEK. Lattice defects in severely deformed biomedical Ti-6Al-7Nb alloy and thermal stability of its ultra-fine grained microstructure. *Journal of Alloys and Compounds*. 2019, vol. 788, pp. 881–890.

- [95] JANEČEK, M., J. ČÍŽEK, J. STRÁSKÝ, K. VÁCLAVOVÁ, P. HRUŠKA, V. POLYAKOVA, S. GATINA and I. SEMENOVA. Microstructure evolution in solution treated Ti15Mo alloy processed by high pressure torsion. *Materials Characterization*. 2014, vol. 98, pp. 233–240.
- [96] VÁCLAVOVÁ, K., J. STRÁSKÝ, V. POLYAKOVA, J. STRÁSKÁ, J. NEJEZCHLEBOVÁ, H. SEINER, I. SEMENOVA and M. JANEČEK. Microhardness and microstructure evolution of ultra-fine grained Ti-15Mo and TIMETAL LCB alloys prepared by high pressure torsion. *Materials Science and Engineering: A*. 2017, vol. 682, pp. 220–228.
- [97] ZAFARI, A., X.S. WEI, W. XU and K. XIA. Formation of nanocrystalline β structure in metastable beta Ti alloy during high pressure torsion: The role played by stress induced martensitic transformation. *Acta Materialia*. 2015, vol. 97, pp. 146–155.
- [98] YILMAZER, H., M. NIINOMI, M. NAKAI, K. CHO, J. HIEDA, Y. TODAKA and T. MIYAZAKI. Mechanical properties of a medical β -type titanium alloy with specific microstructural evolution through high-pressure torsion. *Materials Science and Engineering: C*. 2013, vol. 33, no. 5, pp. 2499-2507.
- [99] KENT, D., G. WANG, Z. YU, X. MA and M. DARGUSCH. Strength enhancement of a biomedical titanium alloy through a modified accumulative roll bonding technique. *Journal of the Mechanical Behavior of Biomedical Materials*. 2011, vol. 4, no. 3, pp. 405–416.
- [100] ZHANG, Z.B., Y.L. HAO, S.J. LI and R. YANG. Fatigue behavior of ultrafine-grained Ti–24Nb–4Zr–8Sn multifunctional biomedical titanium alloy. *Materials Science and Engineering: A*. 2013, vol. 577, pp. 225–233.
- [101] YILMAZER, H., M. NIINOMI, M. NAKAI, J. HIEDA, Y. TODAKA, T. AKAHORI and T. MIYAZAKI. Heterogeneous structure and mechanical hardness of biomedical β -type Ti–29Nb–13Ta–4.6Zr subjected to high-pressure torsion. *Journal of the Mechanical Behavior of Biomedical Materials*. 2012, vol. 10, pp. 235–245.
- [102] SURESH, K.S., N.P. GURAO, D. SATYAVEER SIGNH, S. SUWAS, K. CHATTOPADHYAY, S.V. ZHEREBTSOV and G.A. SALISCHEV. Effect of equal channel angular pressing on grain refinement and texture evolution in a biomedical alloy Ti13Nb13Zr. *Materials Characterization*. 2013, vol. 82, pp. 73–85.
- [103] KURODA, D., M. NIINOMI, M. MORINAGA, Y. KATO and T. YASHIRO. Design and mechanical properties of new β type titanium alloys for implant materials. *Materials Science and Engineering: A*. 1998, vol. 243, nos. 1–2, pp. 244–249.
- [104] NIINOMI, M., Y. LIU, M. NAKAI, H. LIU and H. LI. Biomedical titanium alloys with Young's moduli close to that of cortical bone. *Regenerative Biomaterials*. 2016, vol. 3, no. 3, pp. 173–185.
- [105] VÁCLAVOVÁ, K. *Microstructure and mechanical properties of ultra-fine grained titanium alloys*. Master thesis: Charles University, Prague, 2015.

- [106] VÁCLAVOVÁ, K., J. STRÁSKÝ, P. HARCUBA, V. POLYAKOVA, I. SEMENOVA and M. JANEČEK. Investigation of Microhardness and Microstructure in Ultra-Fine Grained Metastable Beta-Ti Alloys Prepared by High Pressure Torsion. In: *Proceedings of the 13th World Conference on Titanium*. B.m.: Wiley Online Library, 2016, p. 657–662.
- [107] VÁCLAVOVÁ, K., J. STRÁSKÝ, J. VESELÝ, S. GATINA, V. POLYAKOVA, I. SEMENOVA and M. JANEČEK. Evolution of microstructure and microhardness in Ti-15mo β -Ti alloy prepared by high pressure torsion. *Materials Science Forum*. 2017, vol. 879, pp. 2555–2560.
- [108] ŠMILAUEROVÁ, J., M. JANEČEK, P. HARCUBA, J. STRÁSKÝ, J. VESELÝ, R. KUŽEL and H.J. RACK. Ageing response of sub-transus heat treated Ti–6.8Mo–4.5Fe–1.5Al alloy. *Journal of Alloys and Compounds*. 2017, vol. 724, pp. 373–380.
- [109] ŠMILAUEROVÁ, J., M. JANEČEK, P. HARCUBA and J. STRÁSKÝ. Aging study of TIMETAL LCB titanium alloy. *METAL 2013 - Conference Proceedings*. 2014, vol. 9.
- [110] SHEKHAR, S., R. SARKAR, S.K. KAR and A. BHATTACHARJEE. Effect of solution treatment and aging on microstructure and tensile properties of high strength β titanium alloy, Ti–5Al–5V–5Mo–3Cr. *Materials & Design*. 2015, vol. 66, pp. 596–610.
- [111] NG, H.P., A. DEVARAJ, S. NAG, C.J. BETTLES, M. GIBSON, H.L. FRASER, B.C. MUDDLE and R. BANERJEE. Phase separation and formation of omega phase in the beta matrix of a Ti–V–Cu alloy. *Acta Materialia*. 2011, vol. 59, no. 8, pp. 2981–2991.
- [112] TANE, M., Y. OKUDA, Y. TODAKA, H. OGI and A. NAGAKUBO. Elastic properties of single-crystalline ω phase in titanium. *Acta Materialia*. 2013, vol. 61, no. 20, pp. 7543–7554.
- [113] NEJEZCHLEBOVÁ, J., M. JANOVSKÁ, H. SEINER, P. SEDLÁK, M. LANDA, J. ŠMILAUEROVÁ, J. STRÁSKÝ, P. HARCUBA and M. JANEČEK. The effect of athermal and isothermal ω phase particles on elasticity of β -Ti single crystals. *Acta Materialia*. 2016, vol. 110, pp. 185–191.
- [114] XU, W., X. WU, M. STOICA, M. CALIN, U. KÜHN, J. ECKERT and K. XIA. On the formation of an ultrafine-duplex structure facilitated by severe shear deformation in a Ti–20Mo β -type titanium alloy. *Acta Materialia*. 2012, vol. 60, no. 13, pp. 5067–5078.
- [115] JIANG, B., K. TSUCHIYA, S. EMURA and X. MIN. Effect of High-Pressure Torsion Process on Precipitation Behavior of α Phase in β -Type Ti–15Mo Alloy. *MATERIALS TRANSACTIONS*. 2014, vol. 55, no. 6, pp. 877–884.
- [116] KOKUOZ, B.Y., H.J. RACK and Y. KOSAKA. High-cycle fatigue crack initiation and growth in TIMETAL LCB. *Journal of Materials Engineering and Performance*. 2005, vol. 14, no. 6, pp. 773–777.
- [117] XU, W., D.P. EDWARDS, X. WU, M. STOICA, M. CALIN, U. KÜHN, J. ECKERT and K. XIA. Promoting nano/ultrafine-duplex structure via accelerated α precipitation in a β -type titanium alloy severely deformed by high-pressure torsion. *Scripta Materialia*. 2013, vol. 68, no. 1, pp. 67–70.

- [118] ZAFARI, A. and K. XIA. Formation of equiaxed α during ageing in a severely deformed metastable β Ti alloy. *Scripta Materialia*. 2016, vol. 124, pp. 151-154.
- [119] JIANG, B., S. EMURA and K. TSUCHIYA. Formation of equiaxed α phase in Ti-5Al-5Mo-5V-3Cr alloy deformed by high-pressure torsion. *Journal of Alloys and Compounds*. 2018, vol. 738, pp. 283–291.
- [120] *Supplier technical sheet*. B.m.: Carpenter Co., Belgium. 2012
- [121] ATI ALLVAC®. *ATI 15MoTMTitanium Alloy, Technical Data Sheet*. 2014
- [122] CHEN, D., J.C. KUO and W.T. WU. Effect of microscopic parameters on EBSD spatial resolution. *Ultramicroscopy*. 2011, vol. 111, nos. 9–10, pp. 1488–1494.
- [123] KELLER, R.R. and R.H. GEISS. Transmission EBSD from 10 nm domains in a scanning electron microscope. *Journal of Microscopy*. 2012, vol. 245, no. 3, pp. 245–251.
- [124] TOKARSKI, T., G. CIOS, A. KULA and P. BAŁA. High quality transmission Kikuchi diffraction analysis of deformed alloys - Case study. *Materials Characterization*. 2016, vol. 121, pp. 231–236.
- [125] EDAXBLOG. TRANSMISSION-EBSD – Taking Transparency to a new level. *EDAX Blog*. 2014.
- [126] KOZLÍK, J. *Microstructure and Texture of Titanium Prepared by Powder Metallurgy*. Master thesis: Charles University, Prague, 2018.
- [127] SCHWARZER, R.A. and S. ZAEFFERER. An Inexpensive CCD Camera System for the Recording and On-Line Interpretation of TEM Kikuchi Patterns. *Materials Science Forum*. 1994, vols. 157–162, pp. 189–194.
- [128] RAUCH, E.F. and M. VERON. Coupled microstructural observations and local texture measurements with an automated crystallographic orientation mapping tool attached to a tem. *Materialwissenschaft und Werkstofftechnik*. 2005, vol. 36, no. 10, pp. 552–556.
- [129] PETŘÍČEK, V., M. DUŠEK and L. PALATINUS. Crystallographic Computing System JANA2006: General features. *Zeitschrift für Kristallographie - Crystalline Materials*. 2014, vol. 229, no. 5, pp. 345–352.
- [130] SCHELL, N., A. KING, F. BECKMANN, T. FISCHER, M. MÜLLER and A. SCHREYER. The High Energy Materials Science Beamline (HEMS) at PETRA III. *Materials Science Forum*. 2014, vol. 772, pp. 57–61.
- [131] DOLLASE, W.A. Correction of intensities for preferred orientation in powder diffractometry: application of the March model. *Journal of Applied Crystallography*. 1986, vol. 19, no. 4, pp. 267–272.
- [132] RODRÍGUEZ-CARVAJAL, J. Recent advances in magnetic structure determination by neutron powder diffraction. *Physica B: Condensed Matter*. 1993, vol. 192, nos. 1–2, pp. 55–69.
- [133] WEST, R.N. Positron Studies of Lattice Defects in Metals. In: P. HAUTOJÄRVI: *Positrons in Solids*. Berlin: Springer-Verlag, 1979.

- [134] ZHÁŇAL, P. *Study of Phase Transformation in Ti Alloys*. Doctoral thesis: Charles University, Prague, 2018.
- [135] VÁCLAVOVÁ, K., J. STRÁSKÝ, V. POLYAKOVA, J. STRÁSKÁ, J. NEJEZCHLEBOVÁ, H. SEINER, I. SEMENOVA and M. JANEČEK. Microhardness and microstructure evolution of ultra-fine grained Ti-15Mo and TIMETAL LCB alloys prepared by high pressure torsion. *Materials Science and Engineering: A*. 2017, vol. 682, pp. 220–228.
- [136] TERYNKOVÁ, A. *Mikrostruktura a mechanické vlastnosti slitiny Ti15Mo připravené metodou ECAP*. Bachelor thesis: Charles University, Prague, 2017.
- [137] LINS, J.F.C., H.R.Z. SANDIM, H.-J. KESTENBACH, D. RAABE and K.S. VECCHIO. A microstructural investigation of adiabatic shear bands in an interstitial free steel. *Materials Science and Engineering: A*. 2007, vol. 457, no. 1, pp. 205–218.
- [138] HAUKE, V. *Structural and Residual Stress Analysis by Nondestructive Methods*. 1st ed. B.m.: Elsevier, 1997.
- [139] BARTHA, K., A. TERYNKOVÁ, J. STRÁSKÝ, P. MINÁRIK, J. VESELÝ, V. POLYAKOVA, I. SEMENOVA and M. JANEČEK. Inhomogeneous Precipitation of the α -Phase in Ti15Mo Alloy Deformed by ECAP. *Materials Science Forum*. 2018, vol. 941, pp. 1183–1188.
- [140] KOZLÍK, J., J. STRÁSKÝ, P. HARCUBA, I. IBRAGIMOV, T. CHRÁSKA and M. JANEČEK. Cryogenic Milling of Titanium Powder. *Metals*. 2018, vol. 8, no. 1, p. 31.
- [141] ČÍŽEK, J. Characterization of lattice defects in metallic materials by positron annihilation spectroscopy: A review. *Journal of Materials Science & Technology*. 2018, vol. 34, no. 4, pp. 577–598.
- [142] ROSSITER, P.L. *The Electrical Resistivity of Metals and Alloys*. B.m.: Cambridge University Press, 1987.
- [143] NG, H.P., A. DEVARAJ, S. NAG, C.J. BETTLES, M. GIBSON, H.L. FRASER, B.C. MUDDLE and R. BANERJEE. Phase separation and formation of omega phase in the beta matrix of a Ti–V–Cu alloy. *Acta Materialia*. 2011, vol. 59, no. 8, pp. 2981–2991.
- [144] SUN, F., F. PRIMA and T. GLORANT. High-strength nanostructured Ti-12Mo alloy from ductile metastable beta state precursor. *Materials Science and Engineering: A*. 2010, vol. 527, no. 16, pp. 4262–4269.
- [145] LEWELLYN, D.J., K.B. BELAY and M.C. RIDGWAY. In-situ transmission electron microscopy of the solid-phase epitaxial growth of GaAs: sample preparation and artifact characterization. In: *10th Australian conference on Nuclear Techniques of Analysis - proceedings*. 1997, p. 222–225.
- [146] TSUCHIYA, K., S. FARJAMI, B.Z. JIANG, X.H. MIN, S. EMURA and S. II. Effect of high-pressure torsion deformation on isothermal ω phase in β -Ti alloys. *Proceedings of 12th world Conference on Titanium*. 2011, vol. 1, pp. 584–587.

- [147] WANG, Y.B., Y.H. ZHAO, Q. LIAN, X.Z. LIAO, R.Z. VALIEV, S.P. RINGER, Y.T. ZHU and E.J. LAVERNIA. Grain size and reversible beta-to-omega phase transformation in a Ti alloy. *Scripta Materialia*. 2010, vol. 63, no. 6, pp. 613–616.
- [148] KILMAMETOV, A.R., Yu. IVANISENKO, A.A. MAZILKIN, B.B. STRAUMAL, A.S. GORNAKOVA, O.B. FABRICHNAYA, M.J. KRIEGEL, D. RAFAJA and H. HAHN. The $\alpha \rightarrow \omega$ and $\beta \rightarrow \omega$ phase transformations in Ti–Fe alloys under high-pressure torsion. *Acta Materialia*. 2018, vol. 144, pp. 337–351.
- [149] ZHÁŇAL, P. *Study of Phase Transformations in Ti Alloys*. Prague, 2014. Master Thesis. Charles University.
- [150] LÜTJERING, G., J. ALBRECHT, C. SAUER and T. KRULL. The influence of soft, precipitate-free zones at grain boundaries in Ti and Al alloys on their fatigue and fracture behavior. *Materials Science and Engineering: A*. 2007, vols. 468–470, The McEvily Symposium: Fatigue and Fracture of Traditional and Advanced Materials, TMS 2006, pp. 201–209.
- [151] HUANG, Y., J.D. ROBSON and P.B. PRANGNELL. The formation of nanograin structures and accelerated room-temperature theta precipitation in a severely deformed Al–4wt.% Cu alloy. *Acta Materialia*. 2010, vol. 58, no. 5, pp. 1643–1657.
- [152] SEMENOVA, I.P., G.I. RAAB, L.R. SAITOVA and R.Z. VALIEV. The effect of equal-channel angular pressing on the structure and mechanical behavior of Ti–6Al–4V alloy. *Materials Science and Engineering: A*. 2004, vols. 387–389, pp. 805–808.
- [153] SAITOVA, L.R., H.W. HÖPPEL, M. GÖKEN, I.P. SEMENOVA and R.Z. VALIEV. Cyclic deformation behavior and fatigue lives of ultrafine-grained Ti-6AL-4V ELI alloy for medical use. *International Journal of Fatigue*. 2009, vol. 31, no. 2, pp. 322–331.
- [154] NEJEZCHLEBOVÁ, J., M. JANOVSÁ, P. SEDLÁK, J. ŠMILAUEROVÁ, J. STRÁSKÝ, M. JANEČEK and H. SEINER. Elastic constants of β -Ti15Mo. *Journal of Alloys and Compounds*. 2019, vol. 792, pp. 960–967.
- [155] PRIMA, F., J. DEBUIGNE, M. BOLIVEAU and D. ANSEL. Control of omega phase volume fraction precipitated in a beta titanium alloy: Development of an experimental method. *Journal of Materials Science Letters*. 2000, vol. 19, pp. 2219–2221.
- [156] VÁCLAVOVÁ, K., J. STRÁSKÝ, P. ZHÁŇAL, J. VESELÝ, V. POLYAKOVA, I. SEMENOVA and M. JANEČEK. Ultra-fine grained microstructure of metastable beta Ti-15Mo alloy and its effects on the phase transformations. *IOP Conference Series: Materials Science and Engineering*. 2017, vol. 194, no. 1, p. 012021.
- [157] GUO, S., Q. MENG, L. HU, G. LIAO, X. ZHAO and H. XU. Suppression of isothermal ω phase by dislocation tangles and grain boundaries in metastable β -type titanium alloys. *Journal of Alloys and Compounds*. 2013, vol. 550, pp. 35–38.

- [158] SEMIATIN, S.L., S.L. KNISLEY, P.N. FAGIN, D.R. BARKER and F. ZHANG. Microstructure evolution during alpha-beta heat treatment of Ti-6Al-4V. *Metallurgical and Materials Transactions A*. 2003, vol. 34, no. 10, pp. 2377–2386.
- [159] LEGROS, M. and G. DEHM. Observation of Giant diffusivity along dislocation core. *Science*. 2008, vol. 319, pp. 1646–1649.
- [160] DESCHAMPS, A., F. DE GEUSER, Z. HORITA, S. LEE and G. RENO. Precipitation kinetics in a severely plastically deformed 7075 aluminium alloy. *Acta Materialia*. 2014, vol. 66, pp. 105–117.
- [161] BOUREZG, Y.I., H. AZZEDDINE, L. HENNET, D. THIAUDIÈRE, Y. HUANG, D. BRADAI and T.G. LANGDON. The sequence and kinetics of pre-precipitation in Mg-Nd alloys after HPT processing: A synchrotron and DSC study. *Journal of Alloys and Compounds*. 2017, vol. 719, pp. 236–241.
- [162] LIVINGSTON, J.D. and J.W. CAHN. Discontinuous coarsening of aligned eutectoids. *Acta Metallurgica*. 1974, vol. 22, no. 4, pp. 495–503.
- [163] QIN, G.W., K. OIKAWA, Z.M. SUN, S. SUMI, T. IKESHOJI, J.J. WANG, S.W. GUO and S.M. HAO. Discontinuous coarsening of the lamellar structure of γ -TiAl-based intermetallic alloys and its control. *Metallurgical and Materials Transactions A*. 2001, vol. 32, no. 8, pp. 1927–1938.
- [164] SHAARBAF, M. and R.A. FOURNELLE. Discontinuous coarsening of lamellar discontinuous precipitate in an Al-29.5at.%Zn alloy. *Materials Science and Engineering: A*. 1988, vol. 102, no. 2, pp. 271–279.
- [165] STANFORD, N. and P.S. BATE. Crystallographic variant selection in Ti-6Al-4V. *Acta Materialia*. 2004, vol. 52, no. 17, pp. 5215–5224.
- [166] HARCUBA, P., K. VÁCLAVOVÁ, J. ČAPEK, J. STRÁSKÝ, M. JANEČEK and M. JANOVSÁ. Alpha Variant Selection Determined from Grain Misorientations in Ti-6Al-7Nb Alloy with a Duplex Microstructure. *Acta Physica Polonica, A*. 2015, vol. 128, no. 4, pp. 570–573.
- [167] ŠMILAUEROVÁ, J., P. HARCUBA, J. STRÁSKÝ, J. STRÁSKÁ, M. JANEČEK, J. POSPÍŠIL, R. KUŽEL, T. BRUNÁTOVÁ, V. HOLÝ and J. ILAVSKÝ. Ordered array of particles in β -Ti matrix studied by small-angle X-ray scattering. *Acta Materialia*. 2014, vol. 81, pp. 71–82.
- [168] ŠMILAUEROVÁ, J., P. HARCUBA, D. KRIEGNER, M. JANEČEK and V. HOLÝ. Growth kinetics of particles in β -Ti matrix studied by in situ small-angle X-ray scattering. *Acta Materialia*. 2015, vol. 100, pp. 126–134.
- [169] ZHENG, Y., J.M. SOSA and H.L. FRASER. On the Influence of Athermal ω and α Phase Instabilities on the Scale of Precipitation of the α Phase in Metastable β -Ti Alloys. *JOM*. 2016, vol. 68, no. 5, pp. 1343–1349.
- [170] ZHENG, Y., R.E.A. WILLIAMS, G.B. VISWANATHAN, W.A.T. CLARK and H.L. FRASER. Determination of the structure of α - β interfaces in metastable β -Ti alloys. *Acta Materialia*. 2018, vol. 150, pp. 25–39.
- [171] FRIEDEL, J. *Dislocations - 1st Edition*. R. Smoluchovski, N. Kurti. B.m.: Pergamon Press, 1964.

- [172] LABUSCH, R. A Statistical Theory of Solid Solution Hardening. *Physica Status Solidi (b)*. 1970, vol. 41, no. 2, pp. 659–669.
- [173] MUÑOZ-MORRIS, M.A. and D.G. MORRIS. Microstructure control during severe plastic deformation of Al–Cu–Li and the influence on strength and ductility. *Materials Science and Engineering: A*. 2011, vol. 528, no. 9, pp. 3445–3454.
- [174] SUN, W.T., X.G. QIAO, M.Y. ZHENG, C. XU, S. KAMADO, X.J. ZHAO, H.W. CHEN, N. GAO and M.J. STARINK. Altered ageing behaviour of a nanostructured Mg-8.2Gd-3.8Y-1.0Zn-0.4Zr alloy processed by high pressure torsion. *Acta Materialia*. 2018, vol. 151, pp. 260–270.
- [175] WANG, H., I. SHURO, M. UMEMOTO, K. HO-HUNG and Y. TODAKA. Annealing behavior of nano-crystalline austenitic SUS316L produced by HPT. *Materials Science and Engineering: A*. 2012, vol. 556, pp. 906–910.

LIST OF ABBREVIATIONS

ACOM-TEM	automated crystal orientation mapping in a TEM
ARB	accumulative roll-bonding
bcc	body-centered cubic
BSE	backs-scattered electrons
BF	bright field
CCD	charge-coupled device
CG	coarse-grained
CP	commercially pure
DF	dark field
EBSD	electron backscatter diffraction
ECAP	equal channel angular pressing
EDS (EDX)	energy dispersive X-ray spectroscopy
FEG	field emission gun
FIB	focused ion beam
FSP	friction stir processing
GB	grain boundary
GIS	gas injection system
hcp	hexagonal close-packed
HEXRD	high energy X-ray diffraction
HPT	high pressure torsion
IPF	inverse pole figure
LT	lifetime
M_s	martensite start (temperature)
OL	objective lens
PAS	positron annihilation spectroscopy
SAED	selected area electron diffraction
SB	shear band
SE	secondary electrons
SEM	scanning electron microscopy
SPD	severe plastic deformation
ST	solution treated
STM	simple trapping model

tEBSD	transmission electron backscatter diffraction
TEM	transmission electron microscopy
TKD	transmission Kikuchi diffraction
UFG	ultra-fine grained
USATU	Ufa State Aviation Technical University
XRD	X-ray diffraction
[hkl]	crystallographic direction with Miller indices h, k and l
(hkl)	crystallographic plane with Miller indices h, k and l
$\langle hhk \rangle$	set of all directions equivalent to [hkl]
{hkl}	set of all planes equivalent to (hkl)
ω_{ath}	athermal ω
ω_{iso}	isothermal ω